E-555

NEUTRAL STRANGE PARTICLE PRODUCTION

AND

POLARIZATION AT LARGE P_T

by

Byron Gene Lundberg

A thesis submitted in partial fulfillment of the requirements for the degree of

Doctor of Philosophy
(Physics)

at the

UNIVERSITY OF WISCONSIN-MADISON

1984

7381496

NEUTRAL STRANGE PARTICLE PRODUCTION

AND

POLARIZATION AT LARGE P_T

Byron Gene Lundberg

Under the supervision of
Professor Lee G. Pondrom

ABSTRACT

A systematic study of the production and polarization of Λ's, $\bar{\Lambda}$'s and K_s^0's has been performed using the Fermilab neutral hyperon beam. The invariant differential cross sections, $Ed^3\sigma/dp^3$, have been measured up to a transverse momentum of 5 GeV/c for the Λ. The A dependence to the cross sections has also been measured by using three different target materials.

The polarization of the Λ has been mapped over a large range of x_F and p_T to good precision for $p_T \leq 3.8$ GeV/c and can be expressed as a simple functional form. The $\bar{\Lambda}$ was found to be unpolarized out to $p_T = 2.8$ GeV/c. A target nucleon dependence to the Λ polarization has been observed.

TABLE OF CONTENTS

1. Introduction 1

2. The Experimental Apparatus 6

   1. Beam Transport 6

   2. The Target Area 9

   3. The Neutral Beam Collimator 12

   4. The Spectrometer 13

   5. Triggers 17

   6. Data Acquisition 19

3. Event Selection 22

   1. Event Reconstruction 22

   2. Event Selection 24

   3. A Note on Monte Carlo Simulation 27

   4. The Event Sample Distributions 29

   5. Event Reconstruction Efficiency 29

4. Cross Section Analysis 38

   1. Definitions 38

   2. Spectrometer Acceptance 40

   3. Momentum Independent Corrections 42

   4. Momentum Dependent Corrections 47

   5. Sources of Systematic Error in $Ed^3\sigma/dp^3$ 48

FERMILAB
LIBRARY

5. Polarization Analysis 51

1. Preliminary Discussion 51

2. Principles of the Analysis 53

3. Data Acquisition Scheme 56

4. The Hybrid Monte Carlo Method 57

5. Fit to the Polarization Data 62

6. Inclusive Invariant Cross Sections: Data 65

1. General Behavior of the Data 65

2. Functional Fits to the Data 67

3. Discussion of the General Behavior 85

4. Target Nucleon Dependence 92

5. Extrapolation to A = 1 103

6. Indirect Λ Production 103

7. Presentation and Discussion of Polarization Data 109

1. The Data 109

2. Functional Fits to the Λ Polarization ... 113

3. Systematic Error Estimation and Backgrounds 115

4. $\bar{\Lambda}$ Polarization Search 124

5. A Dependence 124

6. Helicity Search 130

7. The Effect of Non-direct Λ's 131

8. Discussion of the Results 132

9. Conclusions 136

6. Chapter 6

1. Λ Invariant Cross Section - Be 68

2. $\bar{\Lambda}$ Invariant Cross Section - Be 69

3. K^0_S Invariant Cross Section - Be 70

4. Λ Invariant Cross Section - Cu 71

5. $\bar{\Lambda}$ Invariant Cross Section - Cu 72

6. K^0_S Invariant Cross Section - Cu 73

7. Λ Invariant Cross Section - Pb 74

8. $\bar{\Lambda}$ Invariant Cross Section - Pb 75

9. K^0_S Invariant Cross Section - Pb 76

10. Invariant Cross Sections - p_T Dependence . 77

11. Invariant Cross Sections - x_F Dependence . 80

12. Particle Ratios 83

13. Invariant Cross Section - x_R Dependence .. 88

14. Fit to A^α..... 93

15. A Dependence - Λ 95

16. A Dependence - $\bar{\Lambda}$ 96

17. A Dependence - K^0_S..... 97

18. Λ Multiplicity 100

19. Nucleon Extrapolation - Λ 104

20. Nucleon Extrapolation - $\bar{\Lambda}$ 105

21. Nucleon Extrapolation - K^0_S 106

22. Nucleon Extrapolation - a,b,c 107

7. Chapter 7

1. Λ Polarization 110

2. Λ Polarization vs p_T @ Fixed x_F 111

3. Fit to $\mathbb{P}_\Lambda$ vs p_T @ Fixed x_F 116

4. Fit to $\mathbb{P}_\Lambda$ vs x_F @ Fixed p_T 117

5. Three Dimensional Polarization Fit 118

6. x-bias vs Momentum 121

7. y-bias vs Momentum 122

8. z-bias vs Momentum 123

9. $\bar{\Lambda}$ Polarization 125

10. Λ Polarization for Cu and Pb Targets vs p_T 127 .

11. Momentum Averaged $\mathbb{P}_\Lambda$ for Cu and Pb 128

12. Target Dependent Polarization Ratios 129

13. Polarization Models 135

8. Appendix A : IC and SEM Calibration 138

9. Appendix B : Target Absorption Correction 142

10. Appendix C : Yields and Correction factors ... 147

11. Appendix D : Functional Fit to Cross Section Data 157

12. Appendix E : Tables of Cross Sections 159

13. Appendix F : A Dependence; Tables of α 173

14. Appendix G : Polarization Results 178

LIST OF FIGURES

1. Chapter 1

1. Distribution of Data in x_F and p_T 3

2. Chapter 2

1. Pitching Magnets 8

2. Target Area and Collimator 11

3. Plan View of Spectrometer 14

3. Chapter 3

1. z-vertex Distribution 28

2. Invariant Mass Distributions 30

3. Momentum Spectra 31

4. R^2 Distribution 32

5. Rates vs Production Angle 34

6. Geometric χ^2 Distribution 37

4. Chapter 4

1. Acceptance 43

2. Momentum Dependent Corrections 49

5. Chapter 5

1. $\cos\theta$ Distributions for Data and Monte Carlo 63

CHAPTER 1

Introduction

The development of high flux beams of strange particles, hyperon beams [1], has provided not only a wealth of information on production cross sections, but also made possible measurements of other fundamental properties. The neutral hyperon beam at Fermilab operated from 1974 to 1982, during which time the Michigan-Minnesota-Rutgers-Wisconsin colaboration (the Neutral Hyperon colaboration) performed a succession of experiments in hyperon physics. An unexpected result of this program was the observation of a large polarization signal for inclusive production [2]. This discovery and the subsequent finding that other hyperons were produced polarized provided the means to measure the magnetic moments of the Λ and other hyperons to high accuracy [3].

The phenomenon of inclusive polarization has been

the subject of much experimental study in itself, by the neutral hyperon group and many others. An experiment at Fermilab (E441, 1978) [4] was the first to measure inclusive Λ polarization in a more detailed and systematic way. A liquid hydrogen target was used, and within the limits set by statistical errors, the data are complete in coverage of the low p_T region of x_F-p_T space.† These data suggested that there is a simple dependence of the Λ polariztion on x_F and p_T [5].

The last experiment of the Fermilab neutral hyperon series to measure polarization and cross sections was proposed to extend the prior research to the largest p_T that was practical. Designated E555, it was begun on January 1,1982 and ended February 17 , 1982 in the M2 beam line at Fermilab. The results of this experiment are the subject of this thesis. A schematic representation of the region populated by the data in x_F-p_T space is shown in Fig. 1.1. The data from the copper and lead targets encompass roughly the same region as the polarization data for beryllium.

† Feynman x is defined as $x_F = p_\parallel^* / p_{\parallel max}^*$ where $p_\parallel^*$ is the longitudinal momentum of the produced particle in the nucleon-nucleon center of momentum frame and $p_{\parallel max}^*$ is the maximum allowed longitudinal momentum. In the high energy limit $x_F = 2p_\parallel^* / \sqrt{s}$.

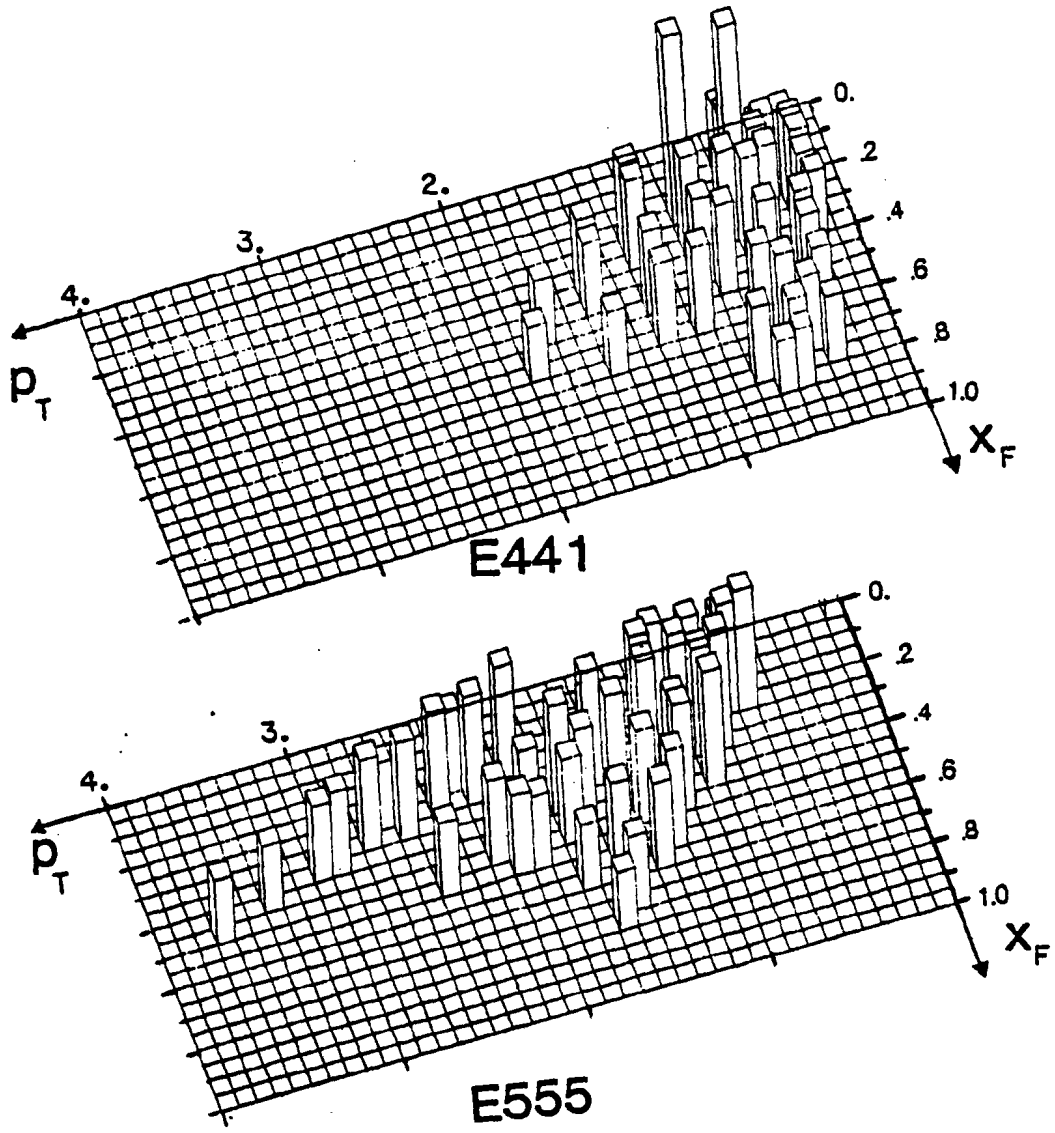

Figure 1. 1 The regions populated by data in the x_F-p_T plane that were used in the polarization analysis. The heights of the bins are roughly proportional to the number of events. The discrete nature of the graphs are due to momentum binning of the data and because the data was taken at fixed production angles.

The following strange particles and the indicated decay modes have been analyzed:

$$\Lambda \dashrightarrow p\pi^-$$

$$\bar{\Lambda} \dashrightarrow \bar{p}\pi^+$$

$$K^0_s \dashrightarrow \pi^+\pi^-$$

All of the particles were produced in inclusive reactions by 400 GeV protons on metal targets made of beryllium, copper, or lead. An "inclusive" reaction means that out of many particles which may be produced in a collision, only one particle is measured.

The inclusive invariant cross sections and polarization were measured simultaneously, using the same data. The cross sections for the Λ, $\bar{\Lambda}$ and K^0_s have been measured extensively at 300 GeV including the dependence on the atomic weight of the target (A dependence) for $p_T < 2$ GeV/c [6]. This experiment greatly increases the range of p_T to 5 GeV/c in cross section and near to 4 GeV/c for the A dependence and polarization.

Acquiring a significant amount of data on neutral particles at large p_T is a more difficult task than obtaining large p_T charged particles. This is so because it is not possible to select the momentum of the particles in the neutral beam before they decay. One can, though,

pick the range of p_T of the beam (by varying the production angle). But as one selects a larger p_T range the number of unwanted low momentum neutrals increases by two orders of magnitude relative to the desirable particles (high p_T Λ's). Therefore, the limiting factor is not the low flux of high p_T particles, but the detector saturation from the low p_T particles and their interactions.

The above outline indicates why it was necessary to record an enormous number of events to extract a sizeable subset of the events with large p_T. Since polarization is a property of an ensemble of events one needs a much larger amount of data relative to a cross section measurement for the same degree of precision. In fact, a polarization measurement which has a relative error of 20% requires about 100 times the amount of data needed for a comparable cross section result.

The analysis which follows is the reduction of over 4×10^7 recorded events to the results given in Chapters 6 and 7.

CHAPTER 2

The Experimental Apparatus

2.1 Beam Transport

The Fermilab proton synchrotron was the source of 400 GeV protons, which were extracted and distributed to many different primary targets, about a kilometer from the extraction point. The experimental beam line consisted of a set of dipole (bending) magnets, quadrupole (focussing) magnets and adjustable collimators (holes) which were tuned to transport a beam of particles of desired charge and momentum from the primary target. For this experiment the beam line was tuned for 400 GeV/c positively charged particles, which were either scattered protons from the primary target or transmitted protons directly from the

synchrotron. These protons were then transported and focussed by the beam line elements onto a secondary target 450 m "downstream" from the primary target. Henceforth, this secondary target will simply be called "the target".

An experimental requirement was that the incident angle of the beam on the target be adjustable over a range of 50 milliradians (mr). This enabled data to be taken at any desired production angle between -25 and +25 mr in the horizontal plane, which was necessary to produce events at large transverse momenta. The production angle was defined to be the angle between the momentum vector of the incident protons at the target and the momentum vector of the detected neutral particle produced at the target.

The desired production angle was achieved by bending the proton beam away from the target 80 m upstream of the target and bending the beam back onto the target with a string of dipole magnets as near as possible to the target. Specifically, this last section of magnets consisted of four, 6 m long main synchrotron dipole magnets with the end of the last magnet just 2 m from the target. Because of the large angles involved, and the small apertures of the magnets, they had to move differentially, forming an arc, with the maximum horizontal travel (between the first and second magnets) being 28 cm. This magnet train is shown schematically in Fig 2.1, in a configuration to transport beam to the target at +20 mr.

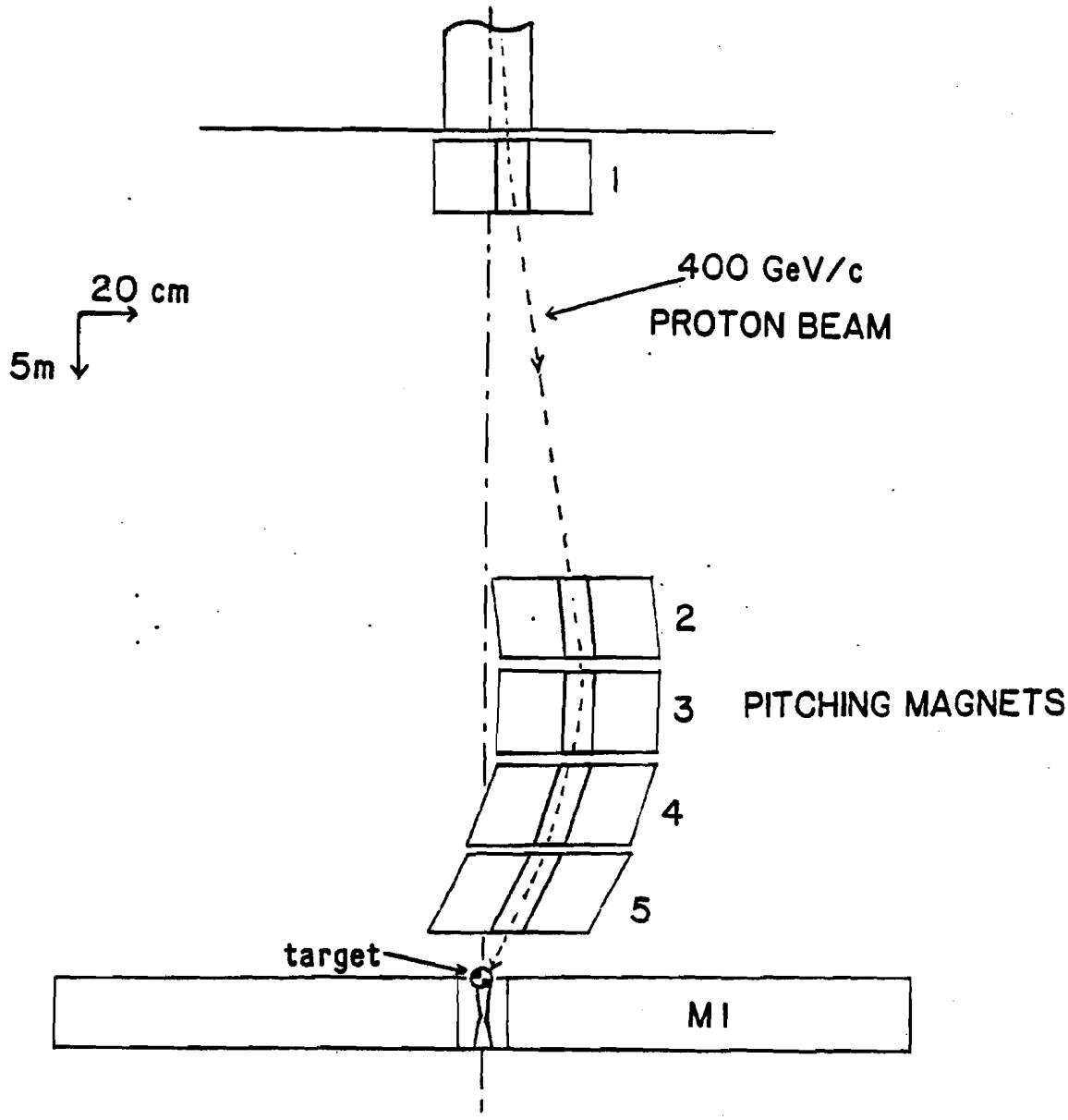

Figure 2.1 The system of five pitching magnets was designed to transport a 400 GeV/c proton beam to the target at angles, θ_p, as large as ±25 milliradians (mr).

2.2 The Target Area

Two types of beam monitoring equipment were employed in the beam line. One set accurately counted the number of 400 GeV protons incident on the target, while another set measured the beam size and position. This experiment required that the incident proton beam intensity on the target be varied by six orders of magnitude. No single beam monitor is useful over such a wide range. Instead, three separate devices with different intensity ranges were used. For the lowest intensities a set of scintillation counters with photomultiplier tubes was used which directly counted individual protons, and could accurately measure fluxes up to about 10^6 protons per second. Intensities exceeding 10^6 per second had to be measured by devices which integrated the total charge of ions created by the passage of the proton beam. An ion chamber, IC, filled with one atmosphere of argon was used for beam intensities not exceeding $5x10^9$, and a secondary emission monitor, SEM, used for all intensities higher than $5x10^9$. The SEM is an evacuated cylinder containing metal foils with a potential of 500 volts between them. The charged beam passing through the foils liberated a number of electrons which were collected on the anode and measured by the integrator. The charge collected on the anodes of both the IC and SEM were measured with digital charge integrators

which were recorded for every machine cycle. The calibrations for the IC and SEM and the proceedures used to determine them are described in Appendix A. The relative positions of the beam monitors and targets are shown in Fig 2.2.

Five cylindrical targets were mounted in a positioning device 20 cm from the beginning of the magnet M1. Three were made of beryllium (atomic weight, A=9), 9.6 mm in diameter and had lengths of 6.00, 9.00 and 15.00 cm. These lengths correspond to 0.2, 0.3 and 0.5 of an interaction length, respectively. The other targets were made of copper (A=63.5) and lead (A=207). Both were 12.6 mm in diameter and one half of an interaction length. Any desired target could be positioned remotely. In addition, all of the targets could be removed from the beam by selecting an empty (air) slot on the target moving device. During data taking the scintillation counters were removed from the proton beam to prevent unwanted sources of particles.

In addition to the beam intensity monitors there were also two segmented wire ion chambers (SWICs) which gave an accurate two dimensional beam profile and the proton beam's position. One SWIC was attached to the end of the last bending magnet, 2 m from the target, and the second SWIC was mounted 15 cm from the target. Both had a wire spacing of one millimeter, and the information from

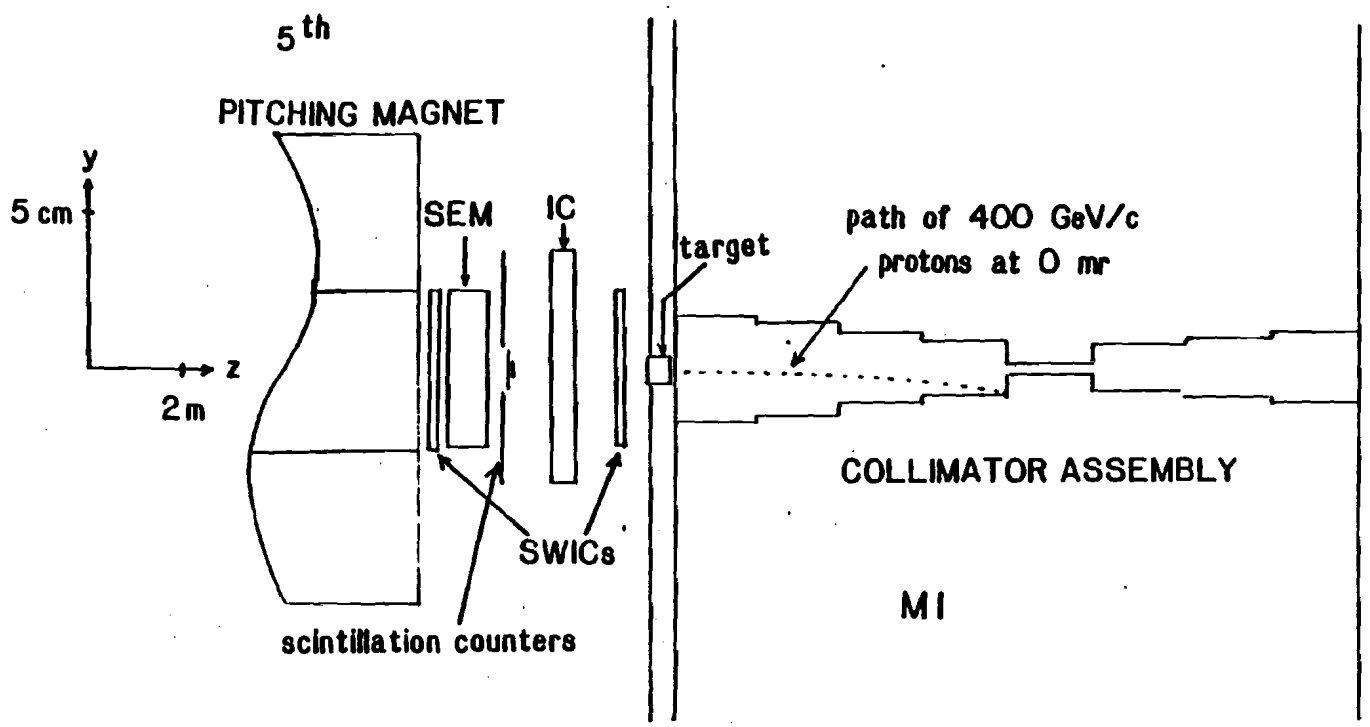

Figure 2.2 The apparatus from the end of the last pitching magnet to the collimator is shown here, with the positions of the beam monitors and target. Also indicated is where the transmitted 400 GeV/c beam is dumped into the collimator at a production angle of zero.

them was updated every machine cycle.

2.3 The Neutral Beam Collimator

The spectrometer was designed to accept the decay products of a neutral beam with a very small angular divergence. The creation of this neutral beam was accomplished by putting a small aperture channel in a strong uniform magnetic field perpendicular to the channel.

The collimating channel itself was a series of rectangular brass blocks with holes drilled through them. The diameter of these holes decreased from either end of the channel to the center block which had a 4 mm diameter defining aperture machined through a 69 cm long tungsten insert. The total length of the channel was 5.28 m, and during the experiment was filled with helium to decrease the probability of interactions and scattering. The entire collimator was immersed in a magnetic field of 22.7 kG which implies a field integral of 12.0 T-m. The 400 GeV/c incident proton beam was deflected 4.8 mm at the defining aperture of the collimator at zero production angle. Hence none of the secondary charged particles from the target were transmitted through the channel. A diagram of the collimator assembly and the target area is shown in Fig 2.2.

The magnetic field had another, subtler effect. For all particles with non-zero spin, the field precessed the direction of the spin by an amount proportional to the line integral of the field and the particle's magnetic moment. The angular rotation of the spin vector in degrees, ϕ, is given by

$$\phi = 18.30\mu_\Lambda \int B\, dl \qquad (2.1)$$

where μ_Λ is the magnetic moment of the Λ. This rotation of the spin gives rise to an observed rotation of the polarization vector and it was this effect which made the precise measurement of μ_Λ possible [7]. The present experiment did not accurately monitor the magnetic field in M1, so ϕ had to be computed in the polarization analysis.

2.4 The Spectrometer

The spectrometer was conventional in design, using multiwire proportional chambers (MWPC's), a large dipole analyzing magnet, and scintillation counters. The layout of the spectrometer is shown in Fig 2.3 along with the designations for its parts that will be used below.

The experiment used six MWPC's, three upstream and three downstream of the analyzing magnet, M2. All had two orthogonal planes of sense wires perpendicular to the neutral beam, with a wire spacing of 2 mm. The wires of

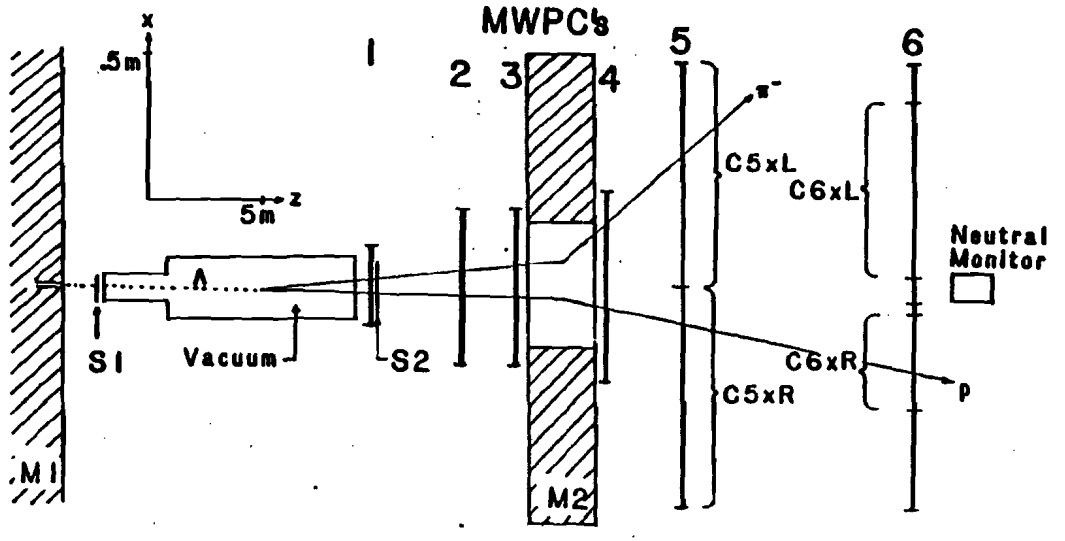

Figure 2.3 The plan view of the spectrometer with all relevant detectors and magnets is shown. The tracks of a typical high momentum Λ is also shown. Note that the proton and pion pass through the sections of MWPC's 5 and 6 which are required for a "T2" trigger (see Section 2.5).

MWPC's 1,3,4,5,6 defined the coordinate system for the two dimensions perpendicular to the neutral beam. The horizontal wires were defined to measure the "y" coordinate (vertical direction) and the vertical wires measured the "x" coordinate (horizontal direction). The z-coordinate axis of this (right handed) system was defined with a low intensity 400 GeV proton beam that was passed through the collimator and spectrometer after removing the target and setting the currents in M1 and M2 to zero. The proton beam was very small transverse to its momentum (4mm FWHM) and so provided an excellent reference, or survey line, so that the relative positions of all MWPC's could be referred to the intersection of the proton beam and each chamber. In general, the measured postions of two particles with two sets of wires per chamber has a two-fold ambiguity. The particle track ambiguity was resloved by using information from MWPC 2 which had its wires rotated by 45° with respect to the other chambers.

The gas used in the chambers was a mixture of argon with 0.2% freon bubbled through methylal at 0°C. The efficiencies of the chambers for detecting charged particles were measured during the experiment and for low fluxes all efficiencies exceeded 98%. Neutral beam fluxes exceeding 10^7 per second caused the efficiencies in the central regions of MWPC's 1,2 and 3 to drop to 92%-95%.

The chamber electronics provided two different

signals which transmitted information about each event. A prompt signal from sets of wires in each MWPC was initiated when any wire from that set recorded the passage of a charged particle, or was "hit". The set could be an entire plane of wires in a chamber, or any connected subset of wires in units of four wires. The prompt signals from several chambers were used with the information from scintillation counters in logic circuits which decided if the event was to be recorded on magnetic tape and analyzed. The logic cicuits themselves were called the event "triggers" , several of which operated in parallel and are discussed in detail in the next section. When the logic circuits had determined that the current event was to be recorded for posterity, a computer controlled the sequence which retreived a latched signal from the chamber giving the relative position or address of every wire that was hit in the spectrometer. Details of the chamber electronics used in this experiment are documented elsewhere [8].

The analysis magnet, M2, was a dipole with iron pole pieces excited by a superconducting coil. The pole tips measured 60 cm wide, 183 cm long, and had a gap of 20 cm. The current was set to give the field integral a value of 3.16 T-m which corresponds to a momentum transfer of 0.95 GeV/c (in the horizontal or x-z plane).

In order to reduce neutral beam interactions and scattering, an evacuated pipe was placed in between the

collimator and the first MWPC. For the same purpose, helium filled plastic bags were put between MWPC's 4 and 5, and between MWPC's 5 and 6, and also in the aperture of the spectrometer magnet, M2.

A neutral beam monitor was placed behind the last chamber, and aligned to intercept the neutral beam. Its purpose was to give a measure of the flux of neutral particles (mostly photons and neutrons) produced in the target. This provided an independent way of checking proton beam position and proton beam intensity at a given production angle. The monitor was a three layer steel and scintillator sandwich equivalent to 8.5 radiation lengths and 1.5 interaction lengths.

2.5 Triggers

Three different event triggers were mixed into a master trigger which initiated data collection. Each trigger used signals from S1 and S2 and prompt outputs from some of the the MWPC's. Several triggers were used simultaneously so that events with different decay topologies could be recorded on the same magnetic tape or "run".

The simplest and least restrictive of the three triggers was designed to accept neutral particles which

decayed in the evacuated pipe and whose charged decay products were not absorbed by the analysis magnet M2. This trigger was designated T1,

$$T1 = \overline{S1} \cdot S2 \cdot C1x \cdot C1y \cdot C5xR \cdot C5xL \cdot C5y$$

The "•" means the logical AND operation and the symbols represent logic signals from, respectively, the two scintillation counters, prompt signals from any x wire, and any y wire in MWPC 1, MWPC 5 right and left halves, and any y from MWPC 5. The "right half" of MWPC 5 was the set of vertical wires from the chamber edge in the -x direction to the geometric center of the neutral beam at the chamber and the "left half" was the set of vertical wires not in the right half. The various regions in MWPC 5 and 6 referred to in disucussion above and below are indicated in Fig. 2.3. It is important to note that at MWPC 5 positive and negative particles were almost completely segregated in the x-z plane, hence the T1 trigger was very efficient in recognizing the neutral two body decays. The S2 and negated S1 required that a neutral particle entered the evacuated pipe and decayed by the time it reached the end of the pipe.

The second and third triggers, T2 and T3, were designed to accept high momentum protons from Λ decay and antiprotons from $\bar{\Lambda}$ decay, respectively. Symbolically,

$$T2 = T1 \cdot C6xR \quad \text{and}$$

$$T3 = T1 \cdot C6xL.$$

Here, C6xR designates the the region in MWPC 6 from -21.8 cm to -2.8 cm, and likewise C6xL was the segment from +2.0 cm to +41.8 cm. For reference, the chamber boundaries were at -58.7 and +69.4 cm.

The triggers T1 and T3 were prescaled, or electronically suppressed, by factors of 32 and 4 respectively, before they were mixed into the master trigger, T,

$$T = \frac{T1}{32} + T2 + \frac{T3}{4}$$

The "+" stands for the logical OR operation. The T2 trigger rejected low momentum Λ's by rejecting low momentum protons because the two momenta were highly correlated. The Λ's in T2 were reduced by a factor of 50 at 50 GeV/c relative to T1. The T3 trigger responded to high momentum negatively charged particles. Note that T3 does not include the small region in MWPC 6 which is often hit by a π^- from decay (11% of the Λ decays at 20 mr).

2.6 Data Acquisition

The data acquisition system included the electronics to digitize the sources of data, the computer to access the

electronics and record the data, and the software to operate the computer. The data acquisition computer was a PDP 11/45 and used standard CAMAC compatible electronics and interface. The data acquisition, or "on-line", software was RT-MULTI, modified to be more efficient at high data rates.

The proton beam intensity was adjusted at each production angle to maximize the ratio of the trigger rate to the dead time. The system dead-time (reciprocal of the duty cycle) was entirely due to the time needed to transfer information from the detector electronics to computer memory. While data transfers were occuring, the computer sent a disable signal, or "gate", to the trigger electronics, since the computer could not be interrupted during transfers. During the first half of the experiment, at production angle of 20 mr, typically 300,000 triggers were written onto a tape at a rate of about 800 triggers per machine cycle (0.85 second). When the synchrotron was running smoothly there was one cycle or "spill" every 12 seconds. In the second half of the experiment part of the computer's memory was replaced with one that had a faster access time, and dead time limited data taking rates exceeded 2000 triggers per spill.

The data recorded for each event consisted of all the MWPC wires for the event, and a number that indicated which trigger had initiated the event. At the end of every

spill the accumulated number of pulses from the IC and SEM charge digitizers, the number of triggers, and the number of prompt signals from the chambers were recorded.

CHAPTER 3

Event Selection

3.1 Event Reconstruction

The reconstruction of an event from MWPC wire information proceeded by looking for two tracks before the magnet M2 and two tracks after M2. The program used was specifically tailored to find patterns from the two oppositely charged particles in the spectrometer resulting from a decay of a neutral particle before the first chamber. This type of pattern is called a "V" with the decay occuring at the vertex of the "V".

The pattern recognition aspect of the program began by searching for two tracks in the y-view (non-bending view) in all of the MWPC's. It then searched for two

tracks in the x-view before the magnet and the true positions in space were found by resolving the x,y ambiguity with the u,v information from MWPC 2. Lastly, the program looked for two tracks in the three chambers downstream of M2, and the tracks before and after the magnet were tested to see if they matched at the bend center for both views. At this stage, no attempt was made to constrain the tracks so they originated from a common point, the vertex of the "V".

After the points had been assigned to the tracks the event was classified according to how many points were found per track and if any extraneous third track before or after M2 had been identified.

Once the neutral "V" pattern had been indentified the tracks were determined with a least squares fit subject to the constraint that the tracks originated from a point. The reduced chi-square of the fit was computed and the event was rejected if it exceeded 3.0. The momenta of the two particles were then calculated as well as the $p\pi^-$, $\pi^+\pi^-$, and $\bar{p}\pi^+$ invariant masses. The invariant mass, M, for a two body decay under the hypothesis that the daughter particles were "i" and "j" is given by

$$M(ij) = m_i^2 + m_j^2 + 2E_i E_j - 2p_i p_j \cos\theta_{ij} \qquad (3.1)$$

The energies, E ,and momenta, p , and the angle between i and j , θ_{ij}, were the measured quantities in the lab system.

If the calculated $p-\pi^-$ ($\bar{p}-\pi^+$) invariant mass was within 10 MeV/c^2 of the Λ ($\bar{\Lambda}$) mass, the event parameters were refit with the constraint that the invariant mass be exactly equal to the Λ ($\bar{\Lambda}$) mass. This kinematic fit adjusted the angles of the decay in the Λ ($\bar{\Lambda}$) center of momentum frame to meet the Λ mass hypothesis. Since the errors in the reconstructed parameters were known, a chi-square test to the kinematic fit could be formed and it served as another indicator of the quality of the event. The main purpose of the fit, however, was to obtain the center of momentum decay angles (θ,ϕ) appropriate for the event. Such a procedure automatically eliminated the unphysical values for the decay parameters (i.e. $\cos\theta > 1$) which might have been computed from the quantities derived from the geometrical fit alone. The corrected angles (θ,ϕ) were used exclusively in the polarization analysis discussed in Chapter 5. The kinematic fitting routine was also used on a small sample of K^0_s candidates, as a test for systematic errors in the polarization analysis.

3.2 Event Selection

Once an event was reconstructed it was placed in a category indicating that it was a Λ, $\bar{\Lambda}$, or K^0_s candidate or none of the above. In addition the events were required to

pass certain cuts. Generally the cuts were made at apparatus boundaries or apertures, and at values of parameters from the geometric or kinematic fit which eliminated background events but did not greatly affect events of interest.

Particle identification was based only on the reconstructed invariant masses (using three hypotheses $\{ij\}=\{p\pi\}, \{\pi^+,\bar{p}\}, \{\pi^+,\pi^-\}$ in Eqn.(3.1)) and the errors in the invariant masses. The identification was made by checking to see if M(ij) was within a "mass window" centered on either the Λ ($\bar{\Lambda}$) mass or the K^0_s mass. Symbolically,

$$M(ij)-M(k) \leq 3\sigma(k) \qquad (3.2)$$

where the index, k, was appropriate for Λ ($\bar{\Lambda}$) or K^0_s. The error in M(k), $\sigma(k)$, was computed for each decay based on the uncertainties in the momenta and positions of the charged particles. Equations (3.1) and (3.2) could be satisfied for both the Λ (or $\bar{\Lambda}$) and K^0_s hypotheses simultaneously. The following rules were applied to deal with the ambiguous solutions:

(1) If the decay was classified in Eqns. (3.1) and (3.2) as a Λ it remained a Λ whether or not it was ambiguous.

(2) If the decay was classified as a $\bar{\Lambda}$ and K^0_s it was rejected from further analysis.

(3) If the decay was classified as K^0_s only but the measured positively charged particle had a momentum greater than the negatively charged particle it was rejected from further analysis.

The data contained other contaminations due mainly to three processes: decays of Ξ^0 hyperons, events that fooled the reconstruction software, and particles that did not originate in the target. Each event was required to pass three geometric cuts intended to reduce the above mentioned sources of background. A cut was made at the defining aperture of the collimator in M1 by requiring the square of the reconstructed transverse distance from the center, R^2, be less than 40 mm^2. This cut eliminated 83% of the $\Xi^0 \rightarrow \Lambda + \pi^0$ in the Λ sample since the daughter Λ from Ξ^0 decay typically had a large momentum component transverse to the neutral beam defined by the collimator. The cut, $R^2 < 40$ mm^2 (or equivalently $|R| < 6.32$ mm) also reduced the number of neutral particles created in the collimator or upstream of the production target.

The only other cut made on the data sample as a whole was the requirement that the reconstructed vertex position be between the scintillation counter , S1, and MWPC 1, within the uncertainty determined for each event. Events whose vertices were determined to be upstream of the S1 counter were kept if the difference in the z-coordinate of the vertex and the S1 counter was less than the error in the vertex point. The uncertainty in the measured vertex along the z axis was highly dependent on the momentum of the neutral particle, the larger errors being associated with higher momentum Λ's, $\bar{\Lambda}$'s, or K^0_S's. The average error

for the measured vertex position along the z-axis was 24 cm at a production angle of 20 mr. A typical reconstructed vertex distribution (20 mr) is shown in Fig. 3.1.

3.3 A Note on Monte Carlo Simulation

For nearly all high energy experiments today, the most important tools, after the detector itself, are the computer simulations done before and after data taking, commonly called Monte Carlo programs. The Monte Carlo program creates "particles" and propagates them through a model of the apparatus and often includes subtleties such as multiple coulomb scattering and spectrometer magnetic field anomalies.

Monte Carlo programs were invaluable in the analysis of this experiment. They were used in the determination of the apparatus acceptance, necesary for cross section measurements, and they were used explicitly in the polarization analysis. The details and results from Monte Carlo simulations are given where appropriate in the following sections and chapters.

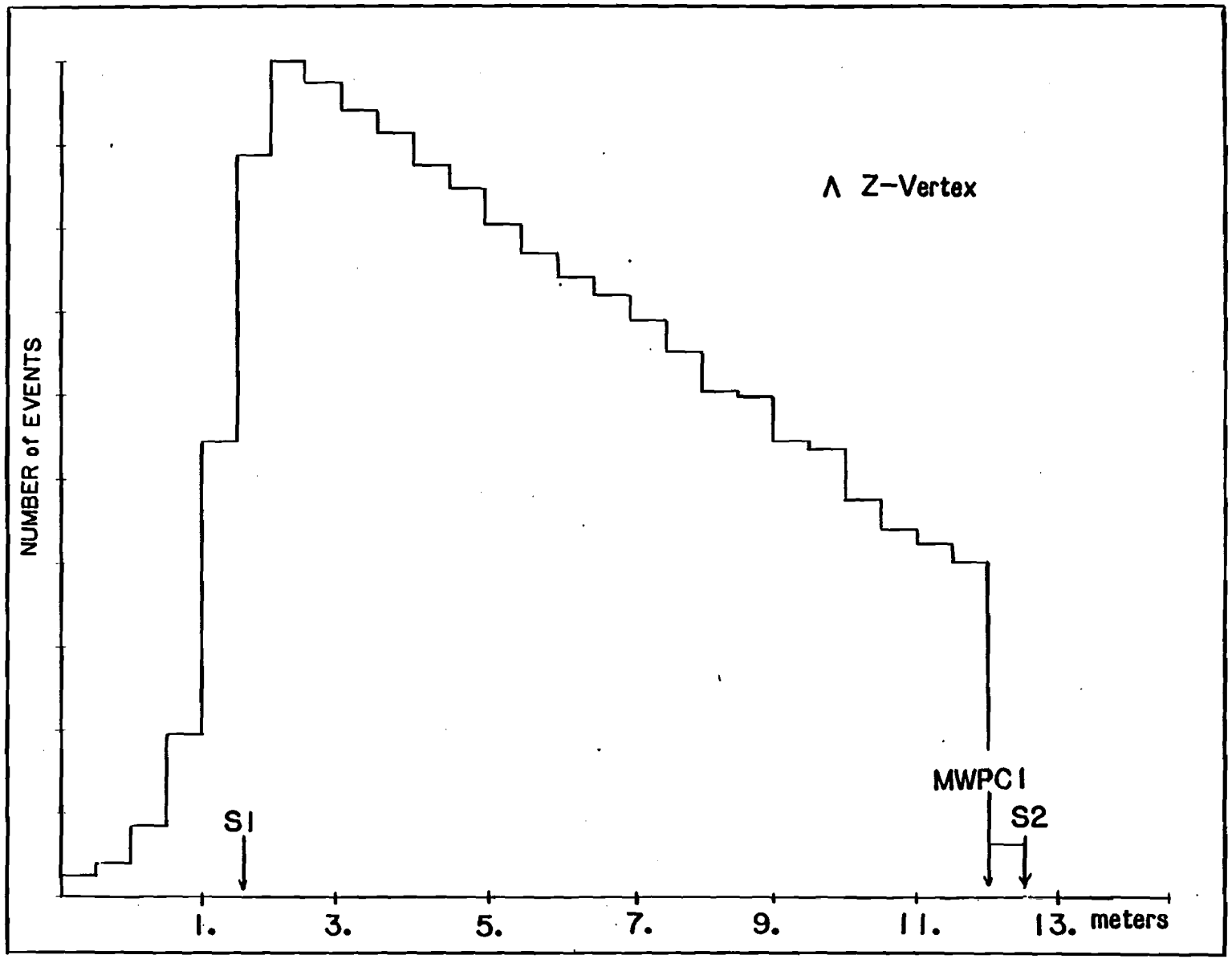

Figure 3.1 The reconstructed position of the Λ vertex along the z-axis is shown here for 20 mr data.

3.4 The Event Sample Distributions

The reconstructed invariant masses for 20 mr without any cuts are shown in Fig 3.2. The momentum spectra of the reconstructed Λ events at various production angles are shown in Fig 3.3.

Figure 3.4 is a plot of R^2 at the defining collimator for Λ's produced at 20 mr compared to the distribution calculated from a Monte Carlo. The linear curve near R^2 equal to zero, corresponding to a gaussian distribution, gives way to a broad background not seen in the Monte Carlo. These large R^2 events are due to daughter Λ's from Ξ^0 decays, most of which are eliminated by the cut shown.

3.5 Event Reconstruction Efficiency

The efficiency of the software in reconstructing the events from the triggers under ideal conditions (i.e. no chamber inefficiencies, no multiple Coulomb scattering, etc.) was measured using Monte Carlo simulation to be 98.5% at 12 mr (momentum averaged). The efficiency in reconstructing the data is reduced by effects which can be classified as either rate (flux) dependent effects or rate independent (physical) effects such as scattering, and

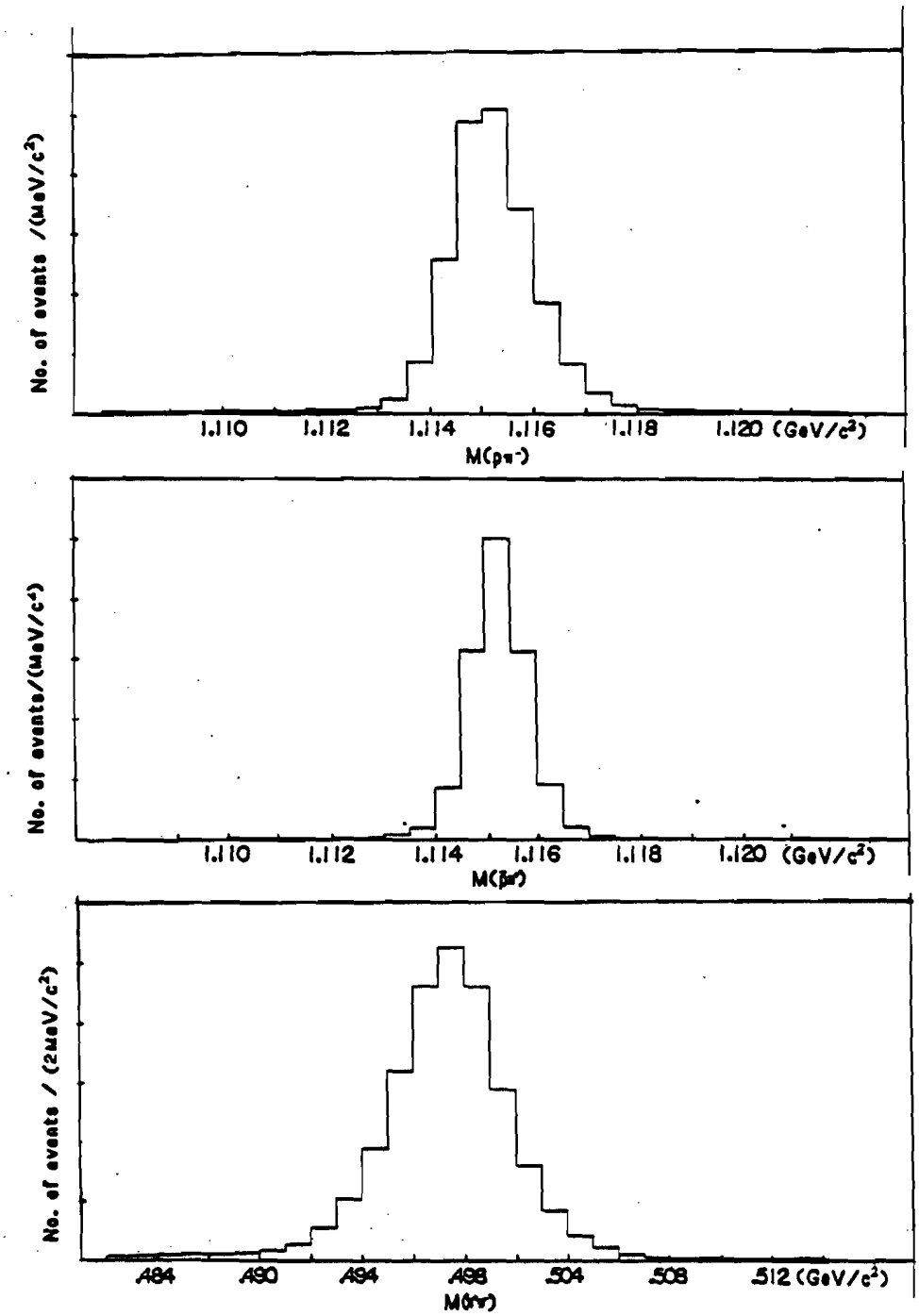

Figure 3.2 The invariant masses for the Λ, $\bar{\Lambda}$ and K^0_S are shown before any cuts were made.

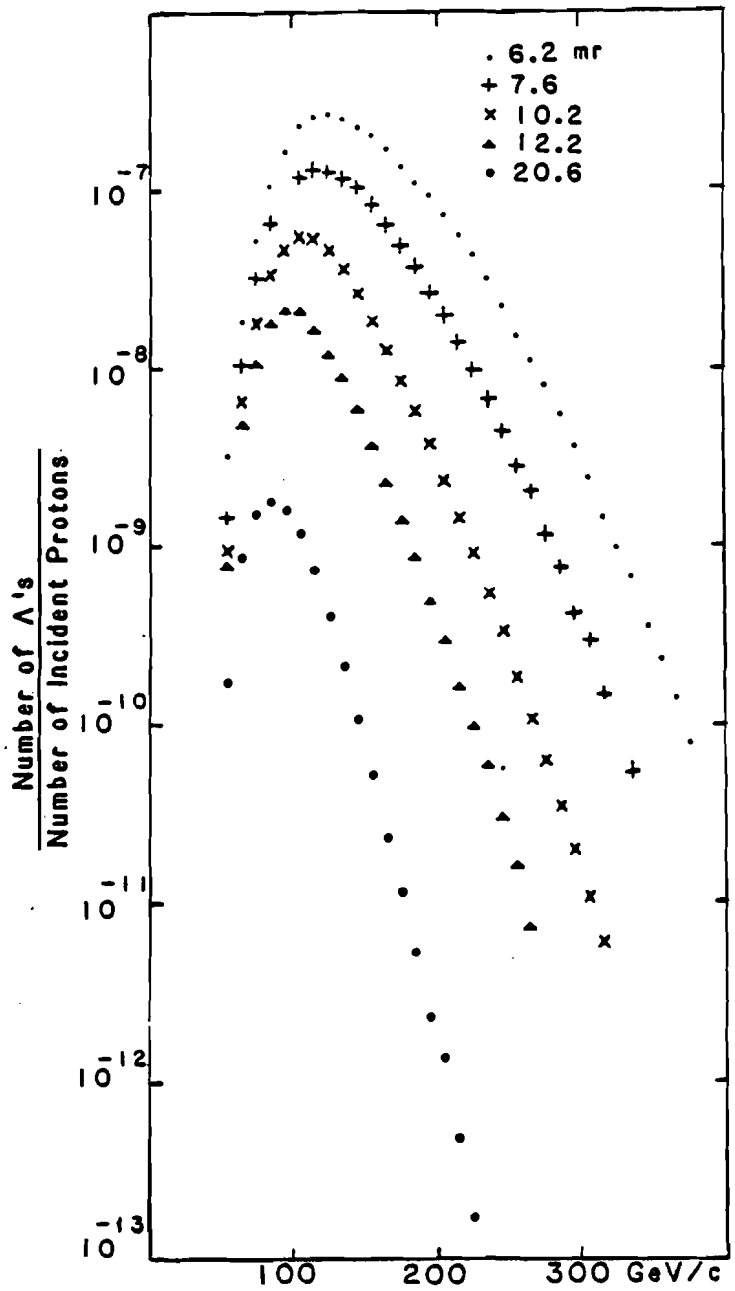

Figure 3.3 The momenta spectra show the number of Λ's from "T2" triggers (after cuts) divided by the number of incident protons at the target. It indicates the relative sensitivity needed to acquire high momentum (high p_T) events.

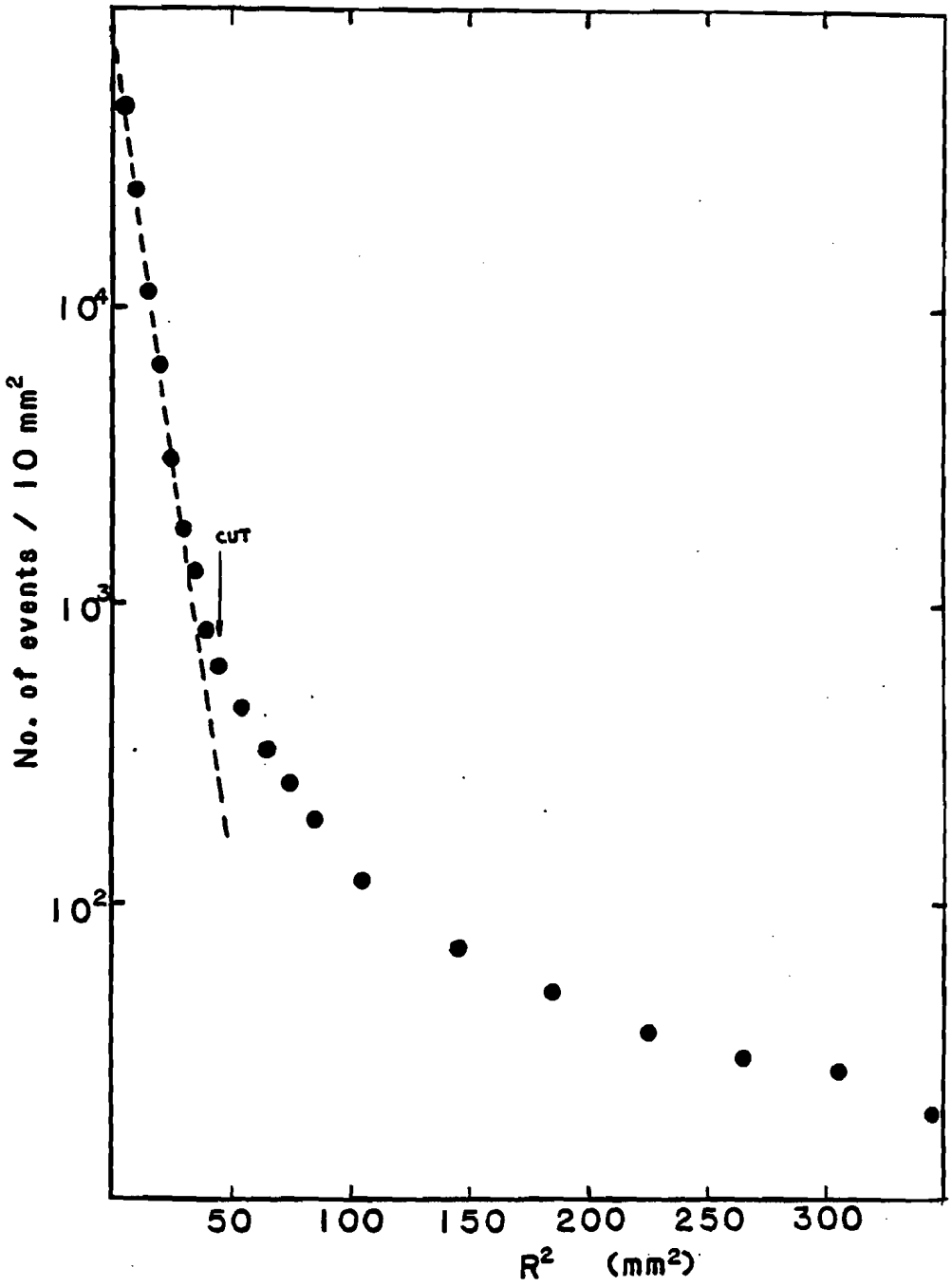

Figure 3.4 The square of the projected distance of Λ's from the neutral beam axis at the defining collimator (R^2) for 20 mr data is compared to a Monte Carlo simulation for Λ's (dashed line). The two distributions are normalized to the first bin.

magnetic field irregularities in M2. The effects of the neutral beam flux are considered first.

The intensity of the neutral beam in the spectrometer varied from 10^3 neutrals per second to more than 10^7 per second as inferred from the neutral monitor. Of course the spectrometer detects neutral particles if they decay (mostly Λ's and K_L^0's), but also if they interact with material in the spectrometer (neutrons and γ's). An approximate guide to the number and kind of neutral particles in the beam versus production angle is shown in Fig. 3.5. A clear feature illustrated in the figure is that the ratio $(n+\gamma)/\Lambda$ increases as θ_p increases. This confirms the observation that at small θ_p one is limited mainly by the charged particle flux due to decays, but at large θ_p (20 mr) one is limited to a greater extent by the rate of neutral conversions in matter.

At any production angle the limitation was the instantaneous rates of charged particles in the chambers which caused inefficiencies due to space charge effects around the wires. These wire inefficiencies are concentrated near the centers of the MWPC's 1, 2, 3, and are usually 3 to 4% but were sometimes as high as 8% (some 20 mr data). The wire inefficiency patterns, averaged over runs for a given θ_p, were included in the Monte Carlo, and the generated events were analyzed by the reconstruction program. The resulting estimates for the efficiency of the

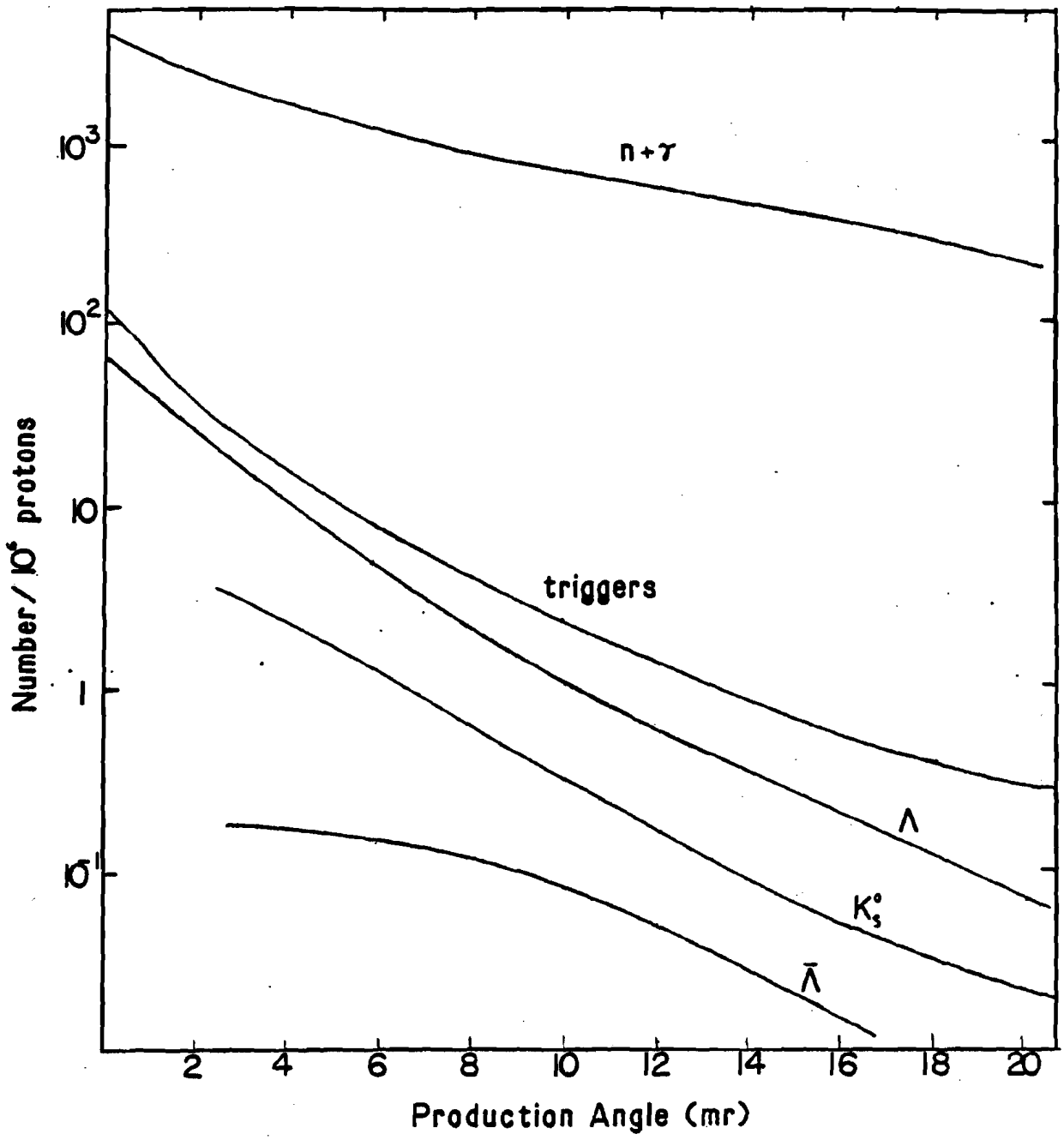

Figure 3.5 The relative number of triggers from the spectrometer and the number of neutral particles detected by the neutral monitor are shown. The curves for small angles are adapted from Ref. 6.

reconstruction process are incorporated into the cross section corrections described in Section 4.4. The results at 20 mr were checked by comparing the yields of a typical (high flux) condition with a run taken with unusually low rates (1/10 of the average).

The loss of reconstruction efficiency from processes not related to beam intensity was also computed using the Monte Carlo. Only three effects were considered: imperfections in the magnetic field of M2 (the reconstruction program assumes a perfect dipole field), multiple Coulomb scattering and pion decay in flight.

The magnetic field in M2 was "mapped" with the charged particles from K_S^0 decays and fit to a second order polynomial in the x and y coordinates. The insertion of this field into the Monte Carlo simulated the small deflections in the y-z plane.

The multiple scattering was simulated for the region between MWPC's 1 and 3. This region contained the greatest amount of material. The counter S2 and the chambers contributed 0.95% of a radiation length and the air was equivalent to 1.8% of a radiation length. The field non-uniformities in M2 had the greatest effect on the efficiency at low momenta. The best indicator of the quality of the track fitting was the chi-square, χ^2_0 defined as the squares of the differences between the chamber hits and the projections of the fitted tracks at each chamber.

It is shown in Fig 3.6 for 20 mr data compared to the χ^2 distribution obtained from Monte Carlo events with the above processes included.

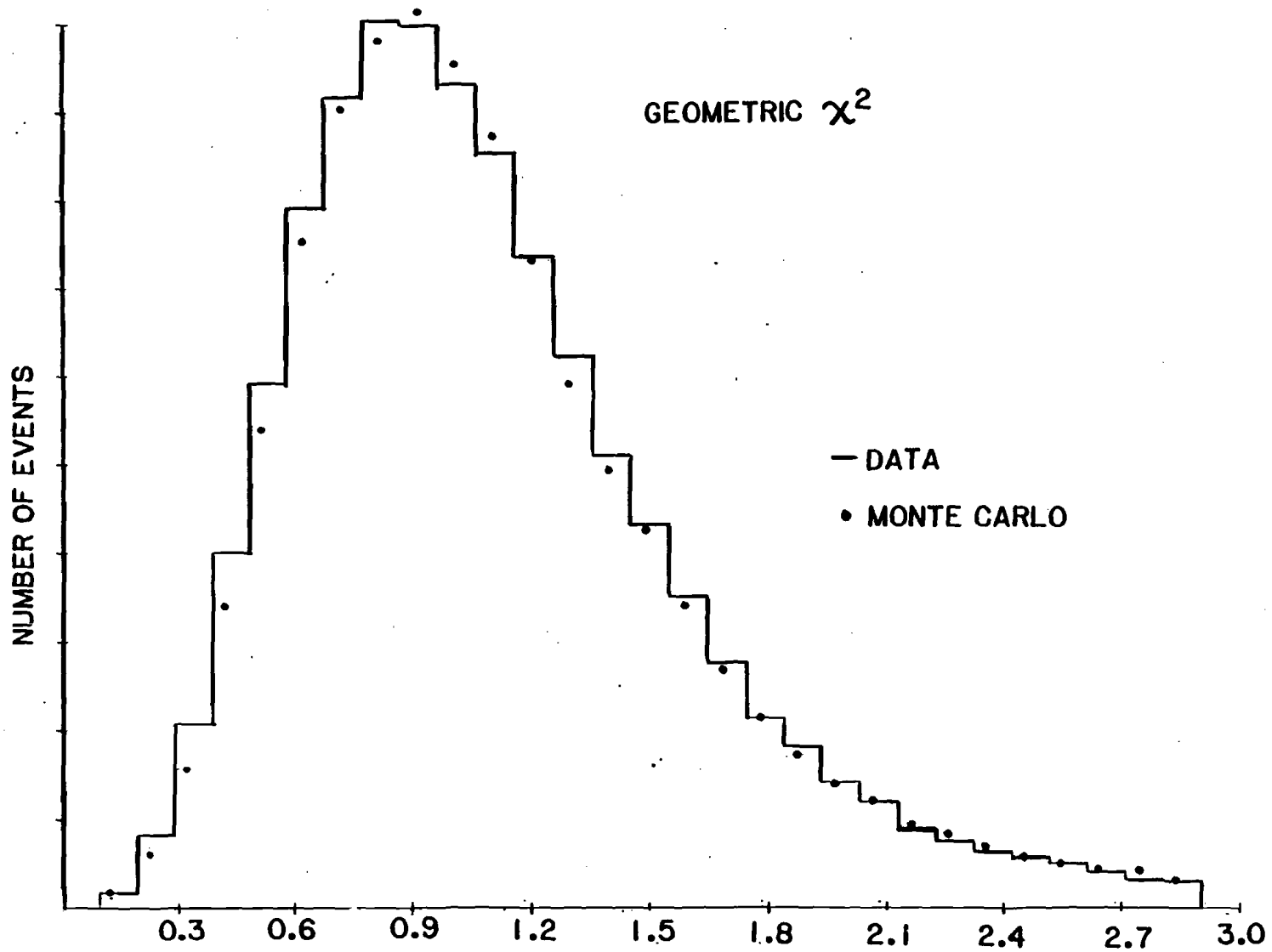

Figure 3.6 The geometric χ^2/d.f. distributions for Λ data and Monte Carlo events at 20 mr. The Monte Carlo used here includes typical chamber inefficiencies, spectrometer magnet non-uniformities, multiple coulomb scattering and π^- decay.

CHAPTER 4

Cross Section Analysis

4.1 Definitions

The Lorentz invariant cross section for the process

$$P + A \dashrightarrow h + X$$

is defined to be the number of particles of type h, per unit flux of protons, P, per target nucleon, produced per second, and per element of phase space, $d^3 p/E$. Symbolically the invariant cross section can be written

$$E \frac{d^3\sigma}{dp^3} = \frac{E}{p^2} \frac{d^2\sigma}{dp d\Omega}, \qquad (4.1)$$

where E and p are the energy and momentum of particle h in the laboratory, and $d\Omega$ is the (infinitesimal) solid angle

into which the observed particle was seen. Experimentally, the apparatus did not accept all momenta with unit probability. Therefore, Eq. (4.1) is rewritten into an operational form which includes corrections and approximations. The invariant cross sections were computed from the following form:

$$E\,\frac{d^3\sigma}{dp^3} = \frac{E\cdot N(p,\theta_p)\cdot A\cdot C\;K(p,\theta_p)\cdot d\cdot S}{p^2\cdot I\cdot N_0\cdot\rho\cdot L\cdot\Delta p\cdot\Delta\Omega\cdot\mathcal{A}(p,\theta_p)\cdot B} \qquad (4.2)$$

The symbols and their meanings are:

- E, p. Reconstructed energy and momentum measured in the lab.

- $N(p,\theta_p)$ Number of observed inclusively produced Λ, $\bar{\Lambda}$, or K_s^0 in the bin with average momentum p at production angle θ_p.

- I Measured number of protons incident on the beam monitors.

- A Atomic weight of the target.

- N_0 Avogadro's number [6.022×10^{23}].

- ρ Target density in g/cm^3 [1.849 (Be), 8.96 (Cu), 11.35 (Pb)].

- L Target length in cm [15.00, 9.00, 6.00 (Be); 4.64 (Cu); 4.84 (Pb)].

- C Correction factor independent of momentum and angle.

- $K(p,\theta_p)$ Momentum and/or production angle dependent correction factor.

- Δp Momentum bin width [10 GeV/c].

- $\Delta\Omega$ Solid angle subtended by the collimator from the target in steradians [$1.23 \pm .06 \times10^{-6}$].

- $\mathcal{A}_h(p,\theta_p)$ Spectrometer acceptance at momentum p, and angle θ_p for particle h.

- B_h Branching ratio for observed decay of particle h [.642 ± .05 ($\Lambda,\bar{\Lambda}$); .686 ± .02 (K^0_s)] [12a].

- d Electronic dead-time correction factor.

- S Trigger scaling factor [4.0 for $\bar{\Lambda}$ and K^0_s; 1.0 for Λ].

The major task in computing the cross sections was the determination of the acceptance and the corection factors in the above list of the parameters ($\mathcal{A}$, C, K, and d). The remainder of the chapter describes how each correction term was computed and what its value is.

4.2 Spectrometer Acceptance

The spectrometer acceptance was defined as the probability that the particle of interest decayed in the proper region of the apparatus and that its decay products cleared all spectrometer apertures and satisfied the trigger requirements demanded for that particle. Specifically, the Λ's were required to satisfy the T2 trigger, and the $\bar{\Lambda}$'s and K^0_s's the T3 trigger. No reconstruction efficiency was included in $\mathcal{A}(p,\theta_p)$. The special criteria for selecting the K^0_s, and $\bar{\Lambda}$ events described in section 3.2 were also included in the acceptance.

The acceptance functions were determined using Monte Carlo computations for the appropriate decay mode. There were two distinct parts to the computations. The first was the probability that the neutral hadron, after being generated in the target, decayed in the vacuum pipe as required by all triggers. The second part determined the probability that both charged particles from the decay passed through the spectrometer restrictions and the portions of the MWPC's which were required in the T1 trigger. The Monte Carlo was used in determining the acceptance for the T1 trigger only, i.e. the trigger excluding MWPC 6. The full acceptance function including MWPC 6 was found by determining the relative acceptance of T2 (or T3) to T1 as a function of momentum using the data (for a given magnitude and sign of θ_p). Then $\mathcal{A}(p,\theta_p)$ was the product of this relative acceptance and the absolute acceptance of T1 found from the Monte Carlo. This approach was taken since the acceptance was found to be sensitive to the sign of θ_p. The qualitative explaination for this fact was easy to understand. The solid angle, $\Delta\Omega$, though small, was large enough (roughly 1 milliradian^2) to allow a range of production angles in the spectrometer, and as it will be shown later, the cross sections rapidly decrease with increasing θ_p. This means that the neutral beam defined by the collimator was skewed in favor of smaller θ_p, and hence the neutral beam oscillated symmetrically in the

x-coordinate, with respect to the z-coordinate axis, when $\theta_r \rightarrow -\theta_r$. The charged daughter particles from the neutrals also had oscillating distribtuions, but the trigger boundary was stationary. Including these effects in a Monte Carlo simulation was not very practical and greatly inferior to using the prescaled T1 which was almost completely unaffected by changes in θ_r. The neutral beam oscillations must also be reckoned with in the polarization analysis in Chapter 5.

The acceptance functions for 10 mr, $\mathcal{A}(p,+10)$, are shown in Fig 4.1 for Λ, $\bar{\Lambda}$, and K^0_s. For Λ's the two functions are nearly identical for momenta greater than 150 GeV/c.

4.3 Momentum Independent Corrections

The largest of the corrections included in the factor C of Eqn (4.2) was the target absorption correction. A target of finite length will attenuate the incident flux of protons as well as absorb a fraction of the created hadrons. The amount of absorption was determined empirically by comparing the yield of Λ's and K^0_s's from the one-half interaction length target to that of the shorter targets. The details of obtaining the corrections are given in Appendix B.

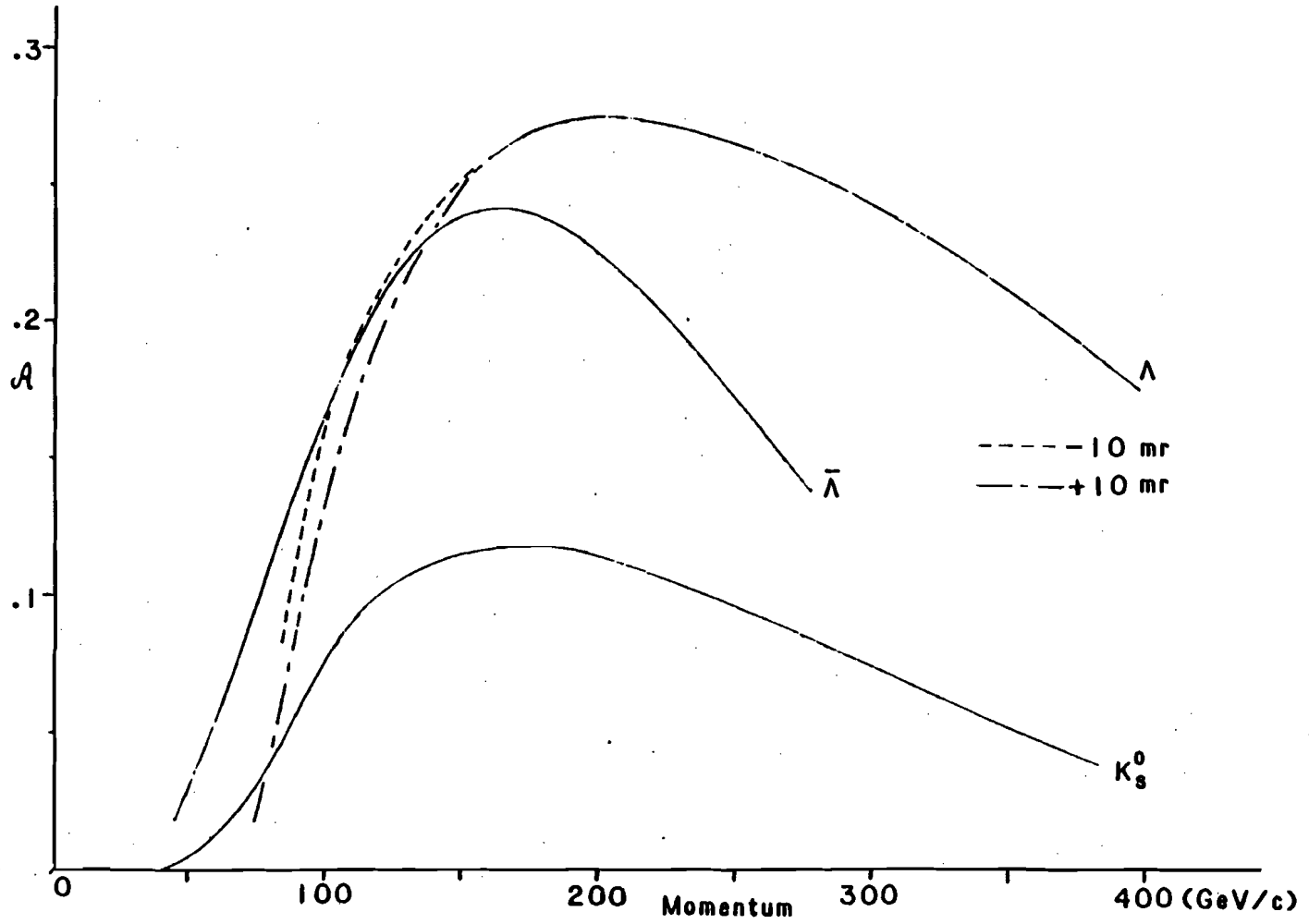

Figure 4.1 The acceptance functions for the three particles are shown. For the the T2 trigger is included in , and for the 's and K 's the T3 trigger is included. It also includes the loss of events which do not decay in the region defined by the counters S1, S2.

A second correction applied to the data compensated for the absorption of the produced neutral particle in the apparatus upstream of MWPC 1 or the absorption of one of the charged particles in the spectrometer. This correction (> 1) depended somewhat on the decay. The estimated values given in Table 4.1 are approximate in that they assume $\sigma_\Lambda = \sigma_\gamma$ and $\sigma_\Lambda = \sigma_p$, and that the total cross sections are independent of $\sqrt{s}$.

Extraneous sources of neutral particles (i.e. not produced in the target) which were recorded by the spectrometer had to be identified and subtracted from the target produced events. The most significant secondary source at 6 and 7 mr was a spot produced near the defining collimator by the transmitted 400 GeV/c proton beam. At 90 GeV/c it accounted for 5.9% of the 6 mr events passing all cuts from Chapter 3 and 3.2% at 7 mr. Although the source itself was strongly momentum dependent it was also very localized and could be effectively eliminated by cutting out a region in the x-y plane at the upstream end of the defining aperture of the collimator. A cut was chosen which eliminated 85±5% of the collimator produced events but eliminated only 2.1±0.8% of the target produced events. These numbers were estimated from fitting two gaussian distributions (2 dimensions) to the beam and source and then applying the cut.

		Λ	$\bar{\Lambda}$	K^0_s
Target Absorption,	Be	1.30±0.04	1.34±0.04	1.27±0.04
	Cu	1.23±0.04	1.28±0.04	1.19±0.04
	Pb	1.19±0.04	1.24±0.04	1.16±0.04
Absorption in Spectrometer		1.07±0.01	1.07±0.01	1.05±0.01
Target size and beam position				
$\theta_p = 20$ mr, Be			1.15±0.06	
$\theta_p < 20$ mr, Be			1.09±0.04	
All θ_p, Cu Pb			1.05±0.05	
R^2 cut at collimator				
$\theta_p = 6$ & 7 mr only			1.02	

Table 4.1 Momentum independent correction factors. The product of these four components for a given θ_p, particle and target is equal to the factor C in Eqn (4.2).

This 2.1% correction is independent of momentum and particle and is the same for 6 and 7 mr. At production angles larger than 7 mr this source is no longer measurable.

The defining collimator also intercepts the neutron beam produced in the target. The Λ's and K_s^0's produced by the neutrons are present in the final sample at all values of θ_r. The precision of the projected position of the Λ at the defining collimator is insufficient to resolve the source which would appear as an annular distribution. One must estimate the contribution of this source by using neutron production data [9]. At 6 mr neutron produced events were estimated to be less than 1% of the total. Since the invariant cross sections for (p+A--> n+X) is similar to (p+A--> Λ +X) in shape this estimate is not very sensitive to θ_r, and hence the neutron induced background is ignored.

The beam monitors upstream of the target are in themselves "targets" and were unwanted sources of neutrals. Their contribution is estimated from data runs taken with the target removed from the proton beam. The estimated relative production of Λ's, $\bar{\Lambda}$'s and K_s^0's from the beam monitors (and air) is 3.2% at 6 mr, 2.2% at 7 mr, 1.0% at 10 mr, 0.7% at 12 mr and 0.2% at 20 mr.

The last momentum independent correction applied to the data compensated for targeting inefficiency. Because

of the transverse size of the beam, not all of the protons counted by the beam monitors struck the target. The typical proton beam was roughly gaussian in both x and y projections with FWHM of 6.5 mm in x and 3.8 mm in y as determined by the SWIC. The RMS positioning error was found to be about 0.9 mm in x and less than 0.5 mm in y. The corrections from these losses depended on the target since the diameter of the copper and lead targets was greater than the beryllium targets, 12.7 mm and 9.8 mm respectively.

The factor denoted by "d" in Eqn. (4.2) corrected for the decays that occurred while the trigger electronics were gated off by the data acquisition system. It was computed by dividing the total number of ungated T1 triggers by the number of T1 triggers which occurred while the system was active for each run. Hence if d=2 for a given run, then the data acquisition system was busy for half of the time that the spectrometer was active.

4.4 Momentum Dependent Corrections

The most significant correction which was a function of momentum was due to the reconstruction losses discussed in Section 3.5.

A second loss originating in the analysis came from the mass cut on the sample of Λ's, $\bar{\Lambda}$'s, and K_s^0's detailed in Section 3.2. Those losses, on the "tails" of the mass distributions, were independent of Θ_p, and increased as a function of momentum. At 200 GeV/c, 4% of the Λ's were lost and 6.5% of the K_s^0's were lost.

There were two sources of background in the Λ sample which could not be eliminated; the K_s^0 decays with ambiguous invariant masses, and the Ξ^0 decays which had daughter Λ's that met the criterion at the collimator, $R^2 < 40\ mm^2$. Both of these backgrounds decrease as the Λ momentum increases because the ratio of the K_s^0 or Ξ^0 cross section to the Λ cross section decreases with momentum. The correction factor due to Ξ's was 0.985 at 85 GeV/c and was greater than 0.995 at 125 GeV/c. From the measured K_s^0 background the correction factor applied to the Λ sample was 0.987 at 85 GeV/c and greater than 0.992 at 165 GeV/c and above.

The momentum dependent correction factors for Λ's which include all of the above effects are shown graphically in Fig 4.2.

4.5 Sources of Systematic Error in $\varepsilon \frac{d^2\sigma}{dp^3}$.

The largest contribution to the systematic error was from variations in the beam monitors from run to run.

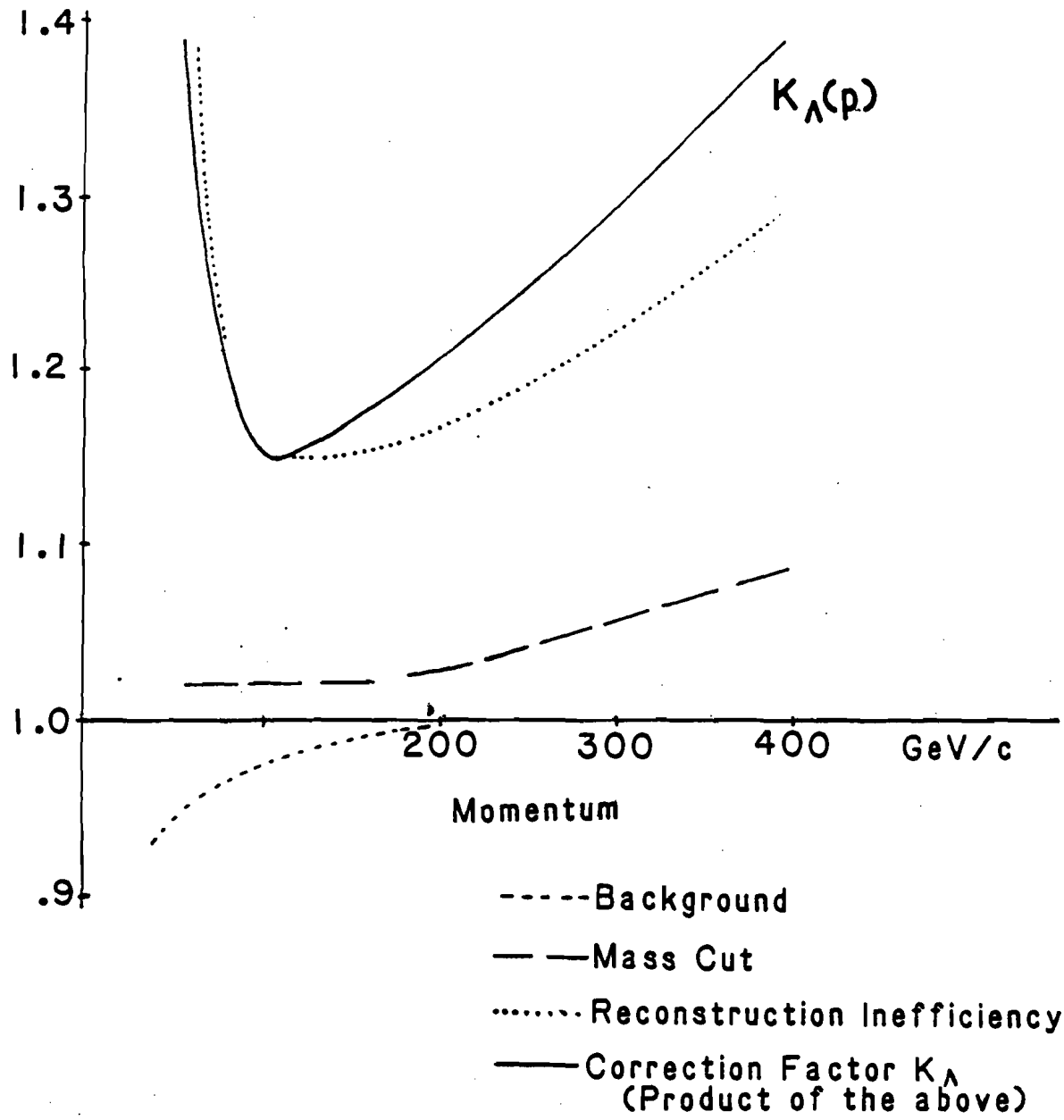

Figure 4.2 Shown here is the momentum dependent correction function $K_\Lambda(p)$ for 20 mr and its components described in Sections 4.2 and 4.3.

These monitors were calibrated only near the beginning of the experiment so the changes in gain had to be inferred from yields and T1 triggers which were recorded for every tape. The RMS deviation in the response of the beam monitors was estimated to be 12%. Other contributions were the uncertainty in the solid angle (6%), the uncertainty in targeting efficiency (4%), and the uncertainty in the reconstruction efficiency (2%). Adding these errors in quadrature gives an overall normalization uncertainty of 14%.

CHAPTER 5

Polarization Analysis

5.1 Preliminary Discussion

The polarization of a sample of particles with non-zero spin ($J \neq 0$) is given by the average value of the spin vector

$$\text{Polarization} = \vec{\mathbb{P}} = \langle \vec{s} \rangle .$$

Parity conservation in the production process restricts the direction of $\vec{\mathbb{P}}$ to be normal to the production plane,

$$\vec{\mathbb{P}} = |\mathbb{P}| \frac{\vec{p}_i \times \vec{p}_o}{\vec{p}_i \times \vec{p}_o} . \qquad (5.1)$$

The vector $\vec{p}_i$ is the incident proton momentum and $\vec{p}_o$ is the momentum of the outgoing, created particle. Equation (5.1) implies that $\vec{\mathbb{P}}$ changes sign when θ_p changes sign. It will

be shown later that this is a very useful property that was fully exploited in the analysis.

The decay mode studied for polarization was, as before,

$$\Lambda \dashrightarrow p\pi^- \qquad (\text{ \& charge conjugate}).$$

This decay is evidently a weak process since the additive quantum number S (strangeness) is not conserved. Therefore the decay need not conserve parity. This fact, together with the conservation of angular momentum and $J = 1/2$, implies a decay distribution for a Λ with its spin along the +z-axis of:

$$dn = \frac{1}{4\pi}(1+\alpha\cos\theta)\, d\Omega. \qquad (5.2)$$

Here, (θ, ϕ) are the decay angles of the proton measured from the Λ spin vector, $\hat{s}$, in its rest system, and decay parameter α has been measured to be 0.642 ± 0.013. This distribution gives the probability of measuring the proton in $d\Omega$ from a single Λ decay knowing the direction of $\hat{s}$. The decay distribution for a polarized sample can be easily derived and is given by

$$\frac{dN}{d\Omega} = \frac{N_{\Lambda}}{4}(1+\alpha\vec{P}\cdot\hat{n}), \qquad (5.3)$$

where $\hat{n}$ is a unit vector parallel to the momentum of the proton in the Λ rest system. Equation (5.3) is the distribution of the protons expected from a polarized

sample of N_{tot} Λ's and is, of course, only valid in the rest frame of the Λ.

5.2 Principles of the Analysis

Given a sample of Λ decays, polarization is determined by matching the experimental decay distribution to the expected distribution, Eqn (5.3), by choosing the polarization, $\mathbb{P}$, which gives the best match. Consider the ideal situation, a spectrometer with perfect acceptance and a reconstruction effiency of 100%, then the expected decay distribution, $dN/d\Omega$, is independent of ϕ. This implies that Eqn (5.3) can be reduced into three independent one dimensional distributions,

$$\frac{dN}{d\cos\theta_i} = \frac{N_{tot}}{2}\,(1+\alpha\,\mathbb{P}_i\cos\theta_i\,). \qquad (5.4)$$

with the coordinate index i=x,y,z. Operationally, one proceeds by counting the number of Λ decays, dN , falling in each cosine bin, $\cos\theta_i$. This number is expected to be a linear function of $\cos\theta_i$ with a slope given by $\alpha\mathbb{P}$. From a linear least square fit to the real event $\cos\theta_i$ distribution, the best estimator for $\alpha\mathbb{P}_i$ would be the slope of ther fitted line. The estimated error in the magnitude of the polarization for this ideal case is given

by $\Delta(\alpha \mathbb{P}) \simeq \sqrt{3/N}$. So much for the ideal case. If the acceptance is not perfect the integration of Eqn (5.3) will not necessarily yield Eqn (5.4) because the range of $(\cos\theta, \phi)$ is not the entire solid angle of 4π steradians. To get a better feeling for what this implies, Eqn (5.3) is expanded and expressed in terms of (θ, ϕ)

$$\frac{dN}{d\Omega} = \frac{N_{tot}}{4\pi} [\ 1 + \alpha \mathbb{P}_z \cos\theta_z + \sin\theta_z\ (\alpha \mathbb{P}_x \cos\phi_z + \alpha\ \mathbb{P}_y \sin\phi_z)] \tag{5.5}$$

The subscript, z, attached to the angles θ, ϕ indicates that the polar axis coincides with the the lab z-coordinate. The distribution relative to x or y is obtained by permuting the indices (x,y,z)-->(z,x,y)-->(y,z,x). As before, for perfect acceptance, integration over the full range of ϕ gives back Eqn (5.3). In this form it seems that for imperfect acceptance in ϕ one cannot split the spatial distribution into three independent distributions. However, if the apertures are approximately symmetric to the beam under reflection (x--> -x ; y--> -y) and if the momentum dependence of the acceptance is not too severe then one may still separate Eqn (5.5) into Eqn (5.4) to very good degree of approximation.

Assume that Eqn (5.4) can be separated into x,y and z distributions, and the acceptance is given by $A\ (\cos\theta_i)$ (ϕ is now irrelevent), then the experimentally observed decays depend on $\cos\theta_i$ by

$$\frac{dN}{d\cos\theta_i} = \frac{N_{tot}}{2} \mathcal{A}(\cos\theta_i)\,(1+\alpha \mathbb{P}_i \cos\theta_i). \qquad (5.6)$$

Taking the ratio of the positive production angle data to the negative angle data the polarization can be extracted due to the reversal of the sign of $\mathbb{P}$. This ratio, r_i, is given by,

$$r_i = \frac{\frac{1}{N_i(+\theta_p)}\frac{dN_i}{d\cos\theta_i}}{\frac{1}{N_i(-\theta_p)}\frac{dN_i}{d\cos\theta_i}} = \frac{1+\alpha \mathbb{P}_i \cos\theta_i}{1-\alpha \mathbb{P}_i \cos\theta_i}$$

and so

$$\mathbb{P}_i = \frac{1}{N}\sum_j \left[\frac{1}{\cos\theta_j}\,\frac{r_i-1}{r_i+1}\right], \qquad (5.7)$$

Note that Eqn (5.7) holds provided the acceptance $\mathcal{A}(\cos\theta_i)$ is independent of the sign of the production angle.

In this experiment the c.m. acceptance $\mathcal{A}(\cos\theta_i)$ did depend on the sign of θ_p for i= x,z (as does the lab acceptance $\mathcal{A}$ defined in Section 4.2). This was due to the beam oscillation phenomenon discussed in Section 4.2. Hence one must use a polarization analysis which is indifferent to this variation in $\mathcal{A}(\cos\theta)$. Without this feature the analysis would impart a systematic error in the derived polarization. It is the supression of systematic errors, in both data acquisition and analysis, which is the primary concern in polarization studies. A description of procedures used for data aquisition which eliminates many

systematic problems is the subject of the following section.

5.3 Data Acquisition Scheme

The most important ingredient for the elimination of systematic errors was the reversal of the sign of the polarization at the production target. Recall that this was accomplished by changing the sign of the production angle, $\theta_p \rightarrow -\theta_p$ which reversed the Λ spin everywhere in space. This fact implies that $\mathbb{P}$ can be measured from two sets of data, one set taken with θ_p and the other taken with $-\theta_p$. For the sake of clarity, let the value of $\mathbb{P}$ that would be measured from one angle alone be called $\mathbb{A}$ for "asymmetry". The asymmetry is defined to be the sum of the true polarization and any false "polarization" signal which from now on will be called a "bias", $\mathbb{B}_i$.

$$\mathbb{A}_i = \mathbb{P}_i + \mathbb{B}_i \qquad (5.8)$$

Then it is obvious that

$$\mathbb{P}_i = 1/2\ [\ \mathbb{A}_i(+\theta_p) - \mathbb{A}_i(-\theta_p)]$$

and

$$\mathbb{B}_i = 1/2\ [\ \mathbb{A}_i(+\theta_p) + \mathbb{A}_i(-\theta_p)].$$

By extracting the polarization information in this manner, the false signals, $\mathbb{B}_i$, which are invariant for $\theta_p \rightarrow -\theta_p$

are eliminated from $\mathbb{P}$ and can be measured with the same accuracy as $\mathbb{P}$. This is the method that was used in obtaining the results of the polarization analysis. During the data taking program, the sign of Θ_p was changed after every two data tapes to ensure equal amounts of data for each sign and as a way to safegaurd against biases which may have varied in the course of the experiment.

The direction of the current in the sweeping magnet, M1, was reversed every four runs. This reversed the direction of precession of the polarization vector which changed the z component of the polarization, $\mathbb{P} \rightarrow -\mathbb{P}$. Once again the bias associated with M1, $\mathbb{B}_z'$, did not change sign (by definition) and one can extract $\mathbb{B}_z'$ directly. However, no measureable difference was seen between $\mathbb{B}_z$ found by reversing production angle and $\mathbb{B}_z'$ found by reversing the field in M1, $\mathbb{B}_z = \mathbb{B}_z'$.

5.4 The Hybrid Monte Carlo Method [10]

The primary motivation for using the Hybrid Monte Carlo (HMC) method is its insensitivity to possible apparatus induced systematic problems. The HMC method is also easily adapted to changes in the spectrometer configuration and its chamber trigger boundaries.

Consider first the following scheme for analyzing

the polarization of a sample of Λ's. It is for illustrative purposes only and never actually used. In addition to the data, i.e. the "real" Λ's, one also generates a sample of Monte Carlo events simulating carefully the conditions under which the data were taken but with various values of the polarization. The reconstructed $\cos\theta_p$ distributions for both the real and Monte Carlo events are compared by forming a chi-square given by

$$\chi^2 = \sum_j \frac{[N_j^{real} - N_j^{mc}]^2}{N_j^{real}} . \qquad (5.9)$$

Here, N_j^{real} is the number of real events in the jth $\cos\theta$ bin and N_j^{mc} is the number of Monte Carlo events in bin j which has been normalized to the total number of real events. The procedure is repeated with a new value of $\mathbb{P}^{mc}$ until the minimum in χ^2 has been found and hence $\mathbb{P}^{mc} = \mathbb{P}^{real}$. Note that for this procedure to be accurate, the total number of Monte Carlo events should greatly exceed N^{real} so that the statistical errors in the Monte Carlo sample are negligible compared to the statistical errors of the real events. In practice, this method has two major drawbacks. First, the number of events which must be generated to get a good map of χ^2 as a function of $\mathbb{P}$ is quite large. Secondly, writing a Monte Carlo program that includes such nuances as oscillations of the neutral beam with θ_p (as discussed in

Section 3.2) is difficult yet important in the determination of the polarization. The Hybrid Monte Carlo is designed to eliminate or at least reduce these objections.

In the Monte Carlo method outlined above all of the event parameters are regenerated for each event. The momentum, decay vertex position, $\cos\theta$ and ϕ are randomly picked for every event. In the Hybrid Monte Carlo (HMC) for each real event a set of 30 Monte Carlo events were generated with $\cos\theta$ chosen randomly for each HMC event as before, but all other event parameters in this set were fixed and equal to the reconstructed values of the real event. Only the parameter ($\cos\theta$) which was physically significant to the quantity to be measured ($\mathbb{A}$) was varied. The acceptance of each event (both real and HMC) as a function of $\cos\theta$, $\mathbb{A}(\cos\theta)$, was determined by making a Lorentz transformation from the Λ rest frame to the lab frame and checking if the trajectories of the proton and pi were within all geometric apertures of the spectrometer. If the real event failed to be accepted it (and its corresponding HMC set of events) was rejected from further analysis. This could occur because the cuts used in the HMC were slightly more restrictive than the actual apertures which were not so well defined. The $\cos\theta_i$'s ($i=x,y,z$) for an accepted real event and the first ten accepted HMC events were stored separately with each $\cos\theta_i$

(real and HMC) divided into twenty bins.

One can now understand why the HMC analysis is not (in principle) affected by the oscillation of particle distributions when $\theta_p \rightarrow -\theta_p$ (Section 4.2). The actual shifting of the neutral beam is input to the HMC via the reconstructed vertex position of the real event that is used in generating the set of decays.

A key feature of this method is that one need not generate many Monte Carlo samples with different $\mathbb{P}$ since each HMC event is weighted by a value that depends on the asymmetry, $\mathbb{A}$, which is to be determined. The HMC events were generated with a uniform (flat) $\cos\theta$ distribution, but the set which passed acceptance cuts gets distorted and the distribution becomes,

$$dN = \frac{N_{hmc}}{4\pi} \mathbb{A}(\cos\theta_1)\, d\Omega \qquad (5.10)$$

The real events were distributed like Eqn (5.6). Therefore to analytically compare distributions, Eqns. (5.7) and (5.10), each HMC event should be given a weight, W, proportional to a polarized sample,

$$W = C(1+ \mathbb{A} \cos\theta^{hmc}) \qquad (5.11)$$

If the apparatus had perfect acceptance in $\cos\theta$ or the Monte Carlo events were generated independently of the

real events (as in the above scheme used as an illustration), then C = 1. This value for C implies that the real event distribution has no influence on the HMC events. But in fact it does have some effect since the real event acceptance is not perfect. To compensate for the effects of the real event polarization the factor C was set equal to $(1+ A\cos\theta^{real})$. Therefore, each HMC event was assigned a weight of

$$W = \frac{1 + A \cos\theta^{HMC}}{1 + A \cos\theta^{real}} \qquad (5.12)$$

Heuristically, the numerator polarizes the HMC events and the denominator removes possible effects of the polarized sample of real events from which the HMC sample is generated. The asymmetries, A_i, are the three quantities which are to be determined by formulating a χ^2, a generalization of Eqn (5.9), to compare the two data sets (HMC and real),

$$\chi^2 = \sum_j \frac{(N^{real} - R_j \Sigma W)^2}{N_j^{real}} . \qquad (5.13)$$

Again the bin index is j and the sum of the weights is over all HMC events in bin j. The R_j normalize the sum of the weights to the single real event (R_j = 1/30 if 30 HMC events were generated for every real event). To facilitate computation, Eqn (5.12) is expanded in a power series in

terms of $\mathbb{A}\cos\theta$ and terms up to third order are kept.

$$W = (1+ \mathbb{A}\cos\theta^{MC})(1+ \mathbb{A}\cos\theta^{real})^{-1}$$

$$= (1+ \mathbb{A}\cos\theta^{MC})\{1- \mathbb{A}\cos\theta + (\mathbb{A})^2 \cos^2\theta^{real} - \cdots \}$$

$$= 1+ \sum_k (-\mathbb{A})^k \cos^{k-1}\theta^{real} (\cos\theta^{real} - \cos\theta^{MC}) \qquad (5.14)$$

Thus the χ^2 can be given an analytical form which is minimized with respect to $\mathbb{A}$ by standard methods.

This analysis was performed for each set of data taken at the same sign and value of production angle and the same sign of the field in M2. The data were combined as described in Section 5.3 to yield the measured values of $\mathbb{P}\alpha$ and hence $\mathbb{P}$.

5.5 Fit to the Polarization Data

In priciple the value of the polarization at each momentum bin j and production angle k can be found by simple vector addition of the components,

$$|\mathbb{P}| = \sum_i \mathbb{P}_i^2 \qquad (i=x,y,z) \qquad (5.15)$$

The sign of $\mathbb{P}$ can be determined via Eqn (2.1) with the known value of μ_Λ and using,

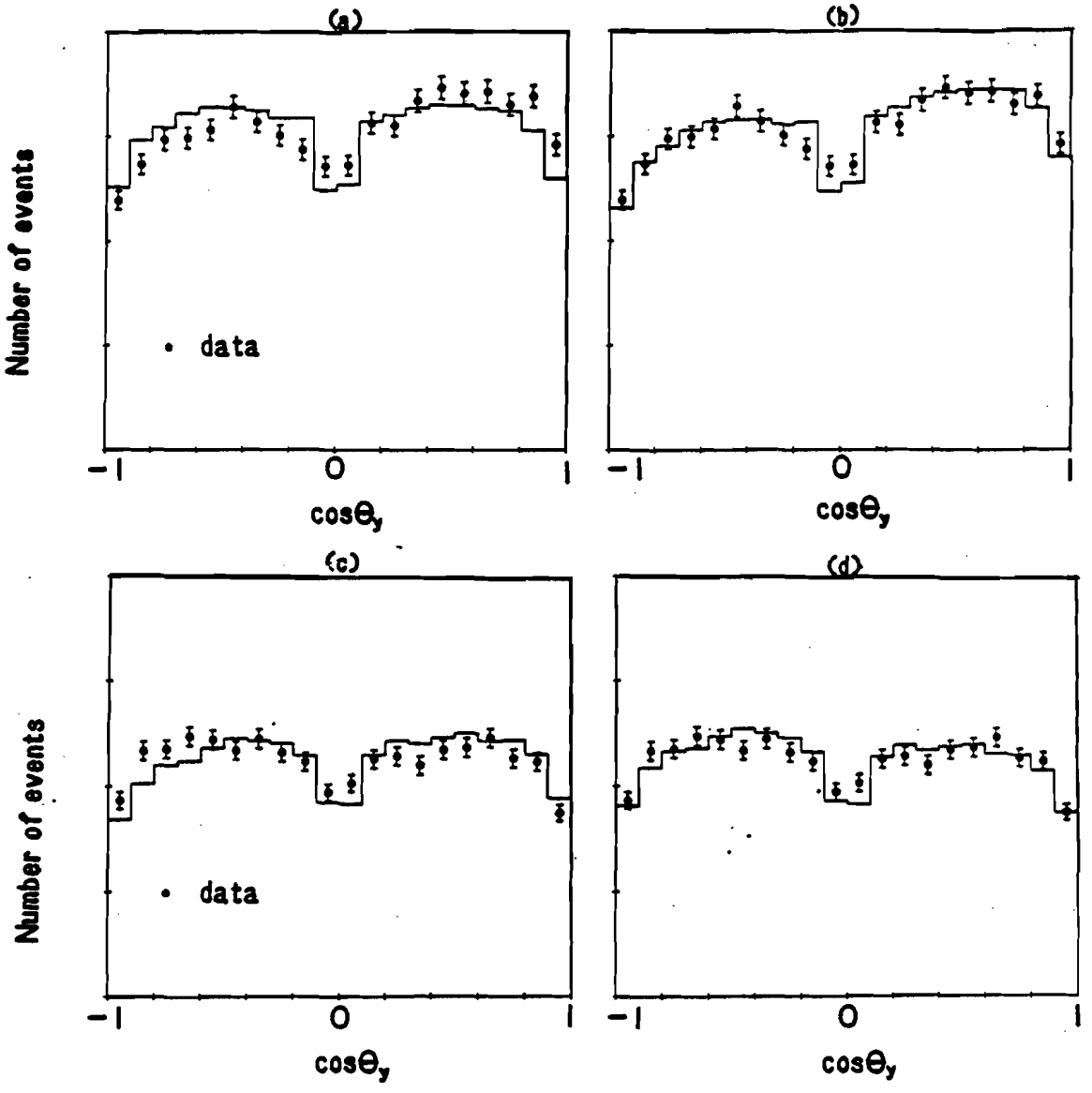

Figure 5.1 Each graph shows the comparison of $\cos\theta_y$ distributions from the data to Hybrid Monte Carlo distributions, before and after the weight, W, has been applied. Part (a) is +10 mr with HMC events unweighted, (b) +10 mr weighted, (c) -10 mr unweighted and (d) -10 mr weighted. The signal derived from this data is $\alpha_\Lambda P_\Lambda = -0.060 \pm 0.020$ (p_Λ = 208 GeV/c).

$$\tan\phi = \mathbb{P}_y / \mathbb{P}_z \qquad (5.16)$$

where ϕ is the precession angle.

In practice a more general approach was used to compute $\mathbb{P}$ which uses three aspects of the physics ignored in the above approach:

(1) ϕ is a constant for all momenta and θ_p
(2) parity conservation implies that $\mathbb{P}_x = 0$
(3) $\mathbb{P}$ precesses in the y-z plane.

Although (2) is an assumption, $\mathbb{P}_x$ was not incorporated into the computation of $\mathbb{P}$. Points (1) and (3) are used explicitly by simultaneously fitting all $\mathbb{P}_i$'s, $\mathbb{B}_i$'s and $\int \mathbb{B}\, dl$ in the minimization of the function,

$$\chi^2 = \sum_{ijk} \frac{\{\mathbb{A}_{y_{ijk}} - (\mathbb{B}_{y_i} \pm \mathbb{P}_i \cos\phi_k)\}^2}{\sigma_y^2} + \frac{\{\mathbb{A}_{z_{ijk}} - (\mathbb{B}_{z_i} \pm \mathbb{P}_i \sin\phi_k)\}^2}{\sigma_z^2} \qquad (5.17)$$

The indices i, j, k, correspond to, respectively, the momentum bin, the two signs of the production angle, and the sign of the field in M1. The input data were the $\mathbb{A}_y$ and $\mathbb{A}_z$'s and the value used for μ_Λ was -0.6138 nuclear magnetons. The polarizations, $\mathbb{P}_i$, and biases, $\mathbb{B}_i$, and $\int \mathbb{B}\, dl$ were treated free parameters. The errors assigned to the $\mathbb{P}_i$, and $\mathbb{B}_i$ are given by the variation in that parameter which increases the value of χ^2 by one.

CHAPTER 6

Inclusive Invariant Cross Sections: Data

6.1 General Behavior of the Data

The data from this experiment cover a different region of $[x_F, p_T]$ space than previous measurements of differential cross sections of Λ, $\bar{\Lambda}$, K^0_S. The forward production (p_T near zero) was not measured since θ_p = 6 mr was the smallest production angle. Instead, the cross sections were measured at higher p and also closer to the kinematic boundary , $x_F \rightarrow 1$, for production angles of 6, 7 and 10 mr.

The values of the invariant cross sections at fixed incident proton angle as a function of the produced particle's momentum are shown in the series of figures 6.1

through 6.9 for all three targets (Be, Cu, Pb). The solid curves in all figures in this chapter (unless otherwise indicated) are derived from empirical fits to the data discussed in the next section. The errors shown do not indicate the overall normalization uncertainty of 14% (see Section 4.4). The complete results of the cross section analysis are tabulated in Appendix C.

The following sample calculation illustrates the mechanics of how $Ed^3\sigma/dp^3$ was computed for 6mr beryllium $\bar{\Lambda}$ data at a momentum of 155 GeV/c. First, the parameters in Eqn. (4.2) are regrouped into the form:

$$\frac{Ed^3\sigma}{dp^3} = \underset{(1)}{\frac{N(p,\theta_F)\ d}{I}} \cdot \underset{(2)}{\frac{K(p,\theta_F)}{A(p,\theta_F)}} \cdot \underset{(3)}{C} \cdot \underset{(4)}{\frac{1}{p}} \cdot \underset{(5)}{\frac{A\ S}{N_0 \rho L\ \Delta p \Delta\Omega\ B}} \qquad (6.1)$$

The first term on the right hand side, (1), is the corrected yield (particles per incident proton) tabulated in Appendix C. The value from the tables is 7.63×10^{-10}. Next, the acceptance including momentum dependent corrections, term (2), is found in Table C.2 and C.3 in Appendix C, and is 4.54. Term (3) is the momentum independent correction for this data point, 1.59, from Table 4.1 (in the text). Term (4) is simply the momentum of the bin, 155 GeV/c. The last group of parameters (5) has the value 2.73×10^{-19}. The product of these terms gives the invariant cross section of the $\bar{\Lambda}$'s at x_F=0.56 and

p_T=1.3 GeV/c, 9.7×10^{-30} cm^2/ GeV^2 .

The p_T dependence of the cross sections for Λ, $\bar{\Lambda}$, and K^0_1 on Be is shown in Figs. 6.10 a-c, and the x_F dependence is isolated in Figs. 6.11 a-c.

The production of $\bar{\Lambda}$'s and K^0_1's relative to Λ production is shown in Figs. 6.12 with a least squares fit to all the data (all targets and production angles).

6.2 Functional Fits to the Data

The functions used in the figures in conjunction with the data were not motivated by any particular model or theory. Rather, the functions are to be considered only as accurate representations of $E\, d^3\sigma/dp^3$ in the region of $[x_F, p_T]$ space spanned by the data. They also provide a way to interpolate the data to regions not directly measured. In effect, they make the range of Θ_F continuous.

The data are fit by standard methods to a function of the form,

$$\exp\{f(p_T, x_F)\}\ (1-x_F)^{g(p_T)} \qquad (6.2)$$

The values for the nine fitted parameters contained in $f(p_T, x_F)$ and $g(p_T)$ are given Appendix D.

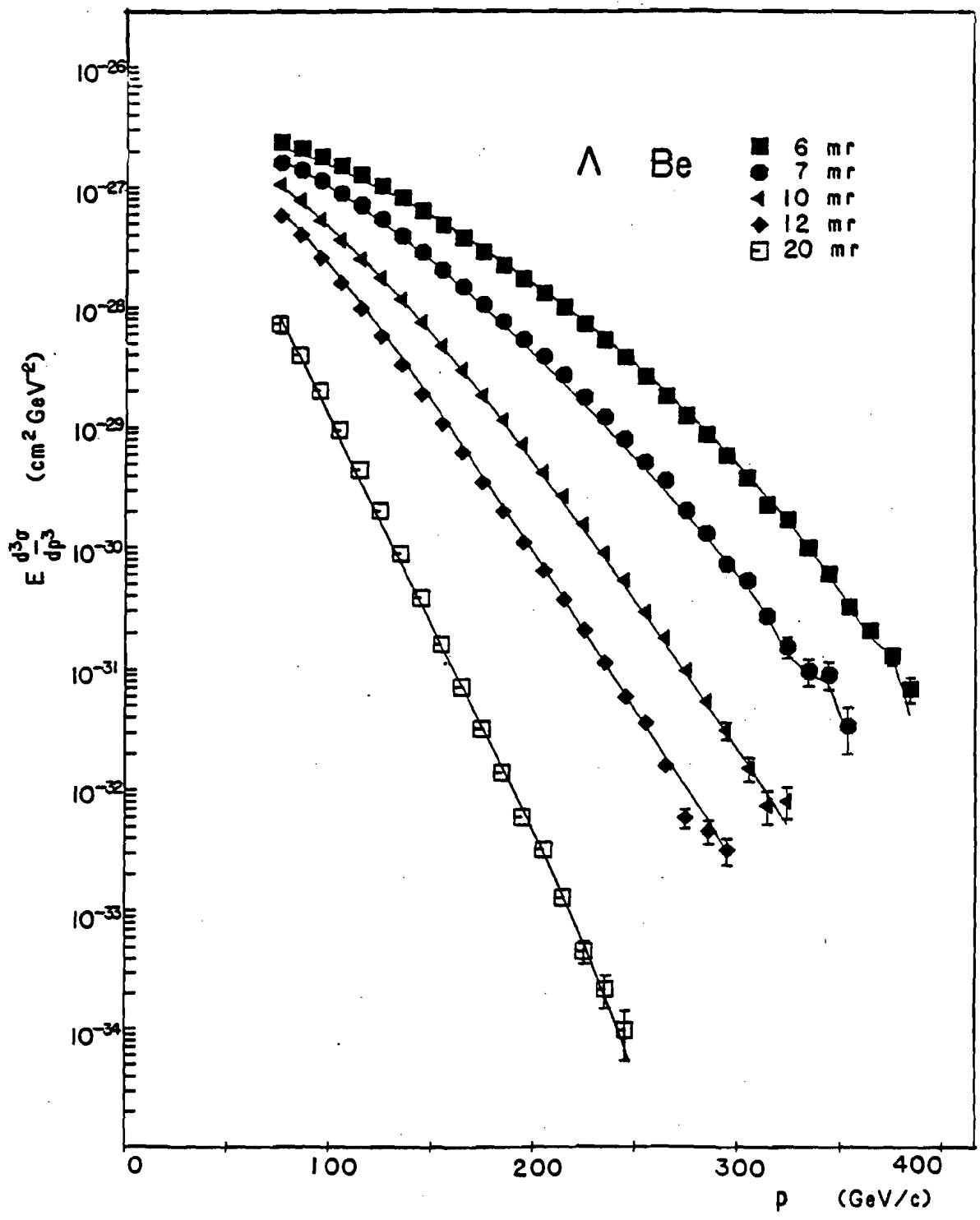

Figures 6.1-6.9 The Lorentz invariant cross sections for Λ, $\bar{\Lambda}$ and K's are shown. The functional fits to the data are indicated by the solid curves. (See Section 6.2 and Appendix B.)

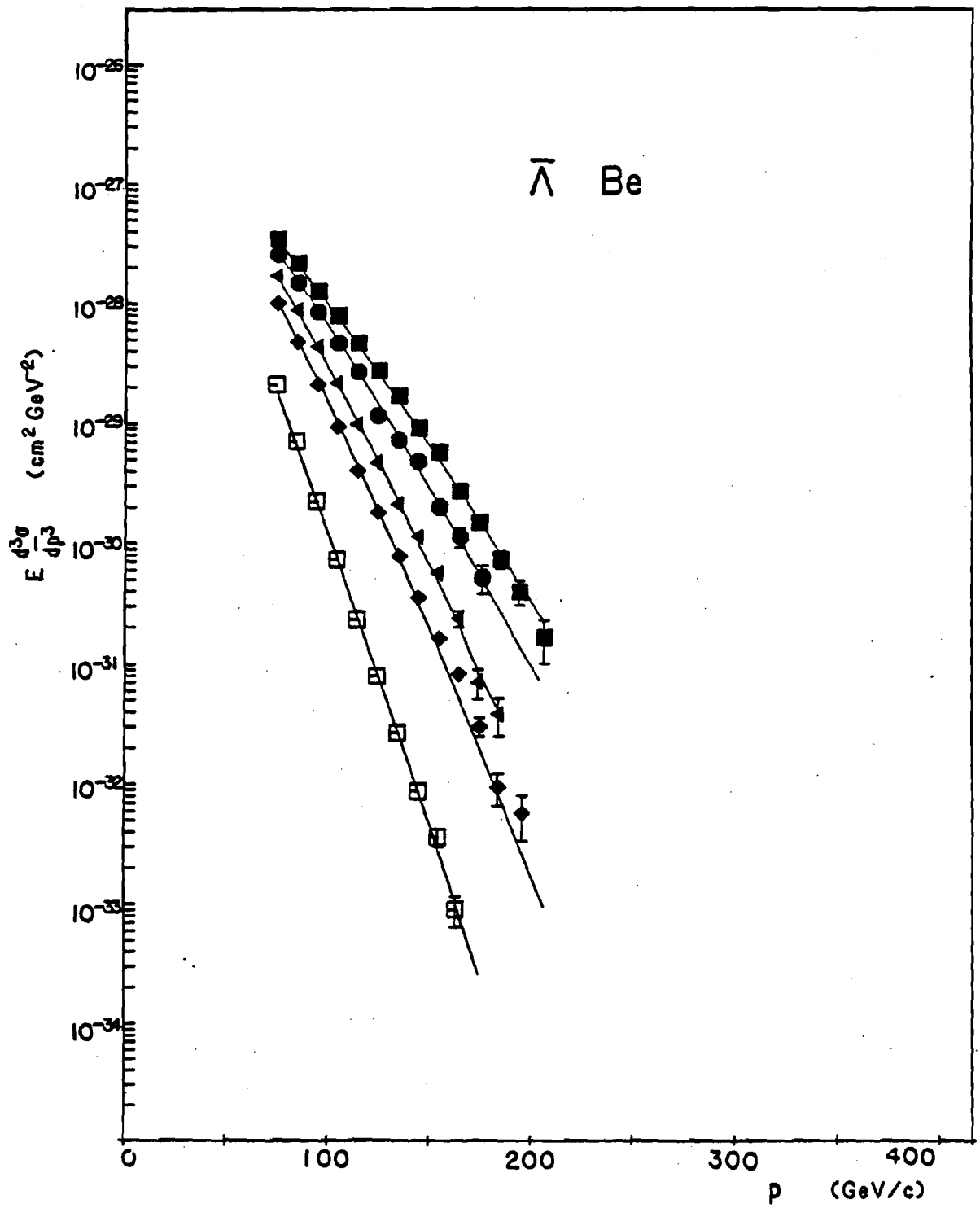
$\bar{\Lambda}$ Be
$E\frac{d^3\sigma}{dp^3}$ (cm^2 GeV^{-2})
10^{-26}
10^{-27}
10^{-28}
10^{-29}
10^{-30}
10^{-31}
10^{-32}
10^{-33}
10^{-34}
0
100
200
300
400
p (GeV/c)

Figure 6.2

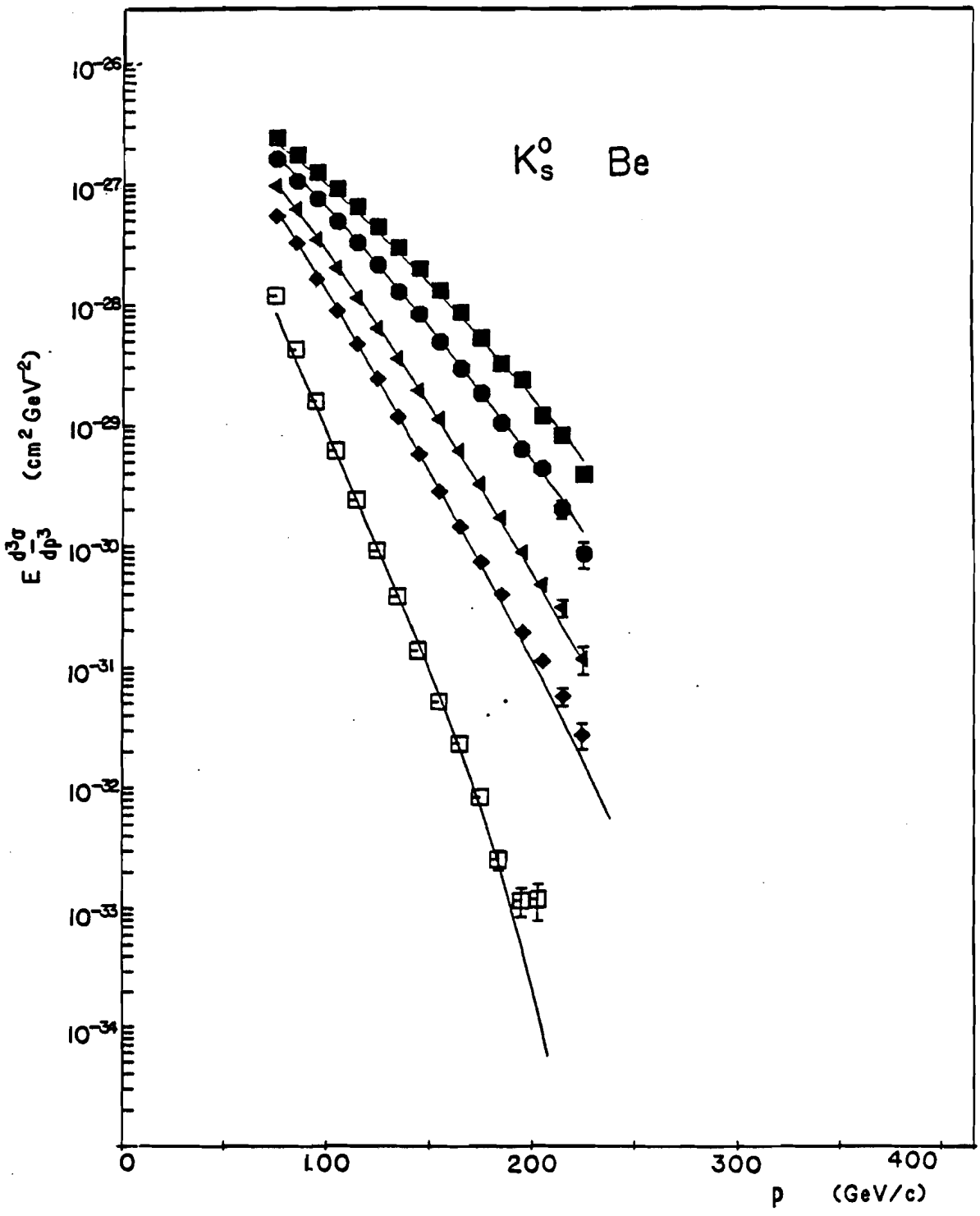
K_s^0 Be
$E\frac{d^3\sigma}{dp^3}$ (cm^2 GeV^{-2})
10^{-26}
10^{-27}
10^{-28}
10^{-29}
10^{-30}
10^{-31}
10^{-32}
10^{-33}
10^{-34}
0
100
200
300
400
p (GeV/c)

Figure 6.3

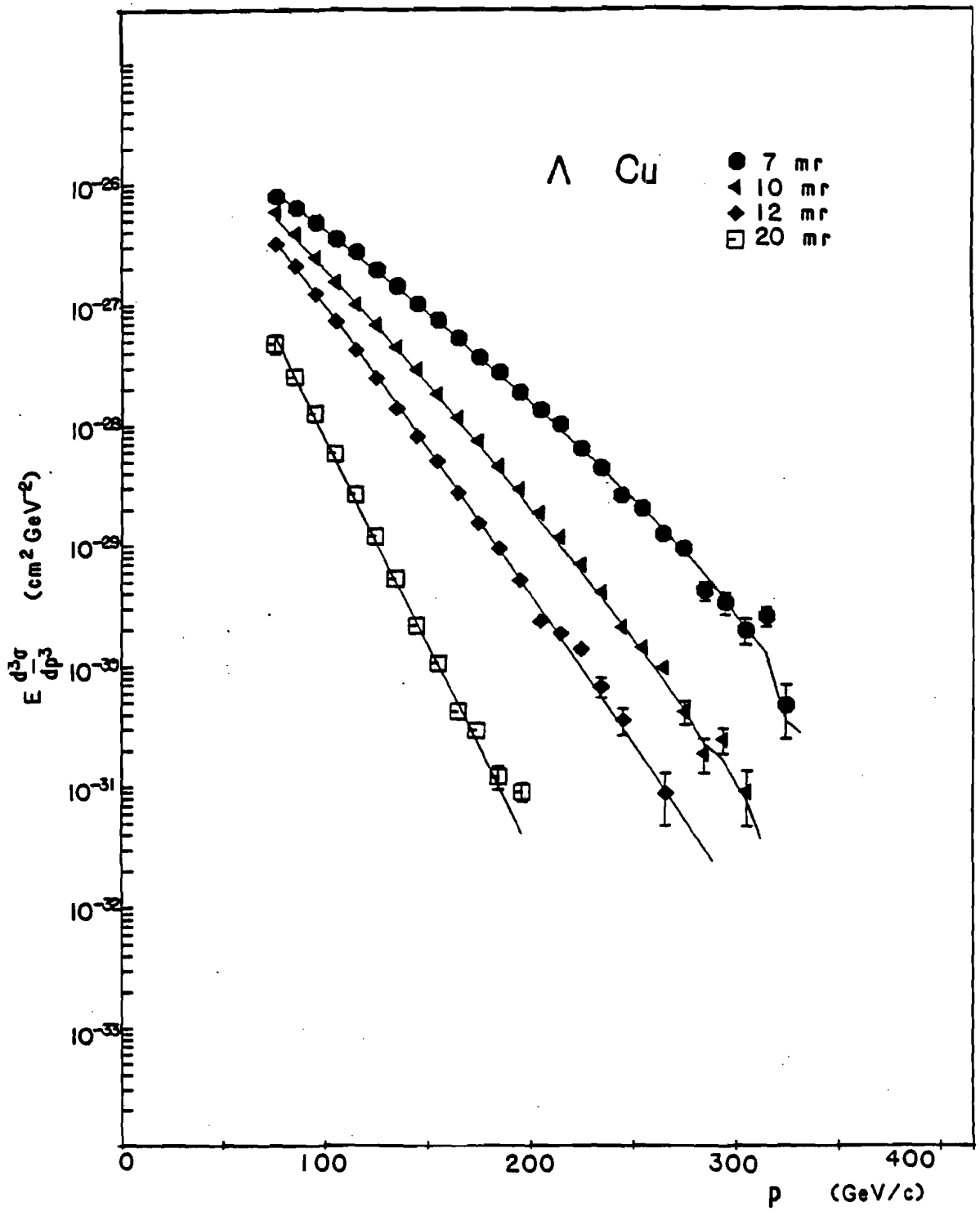
Λ Cu
7 mr
10 mr
12 mr
20 mr
10^{-26}
10^{-27}
10^{-28}
10^{-29}
10^{-30}
10^{-31}
10^{-32}
10^{-33}
$E\frac{d^3\sigma}{dp^3}$ (cm^2 GeV^{-2})
0
100
200
300
400
p (GeV/c)

Figure 6.4

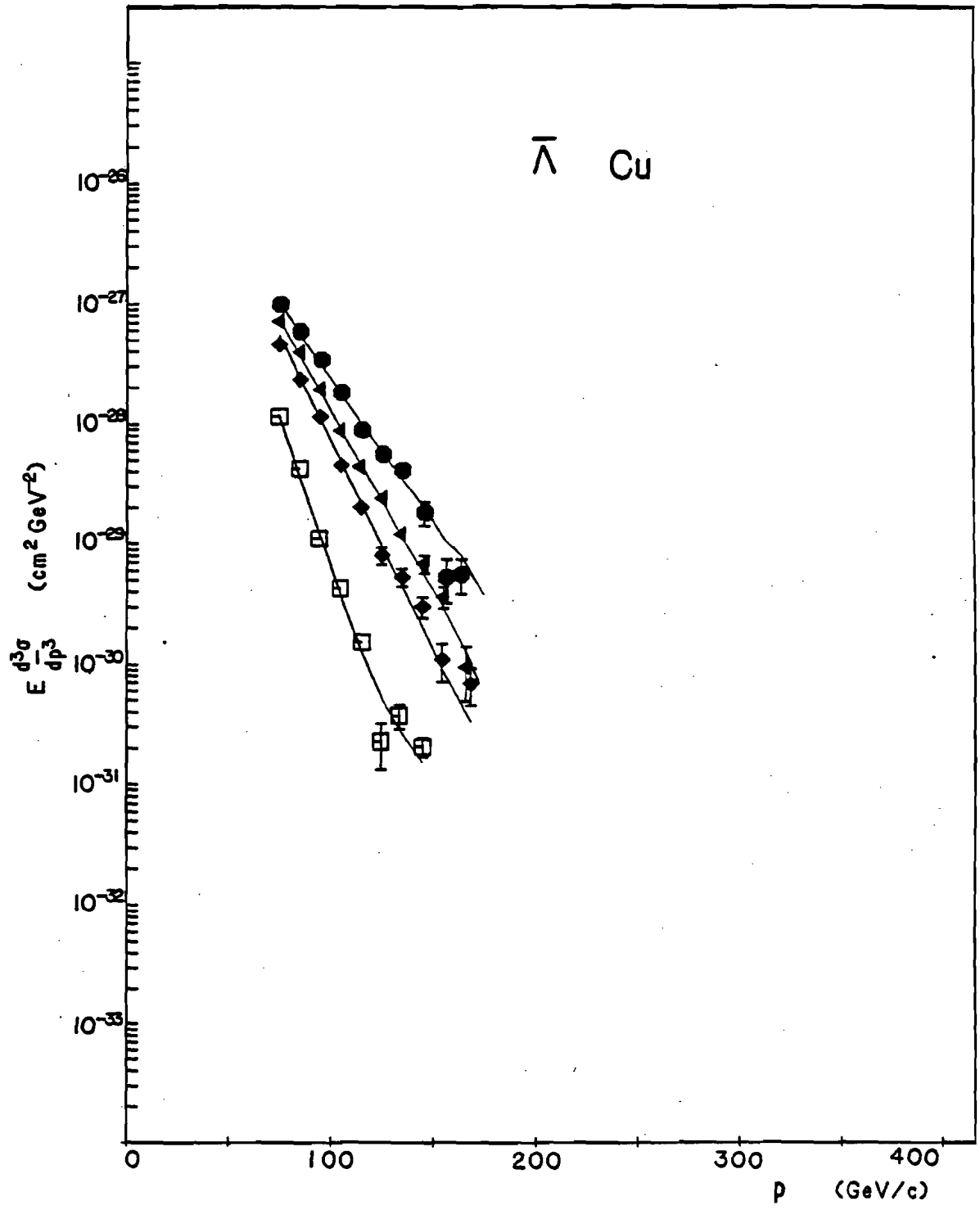
$\bar{\Lambda}$ Cu
10^{-26}
10^{-27}
10^{-28}
10^{-29}
10^{-30}
10^{-31}
10^{-32}
10^{-33}
$E\frac{d^3\sigma}{dp^3}$ $(cm^2 GeV^{-2})$
0
100
200
300
400
p (GeV/c)

Figure 6.5

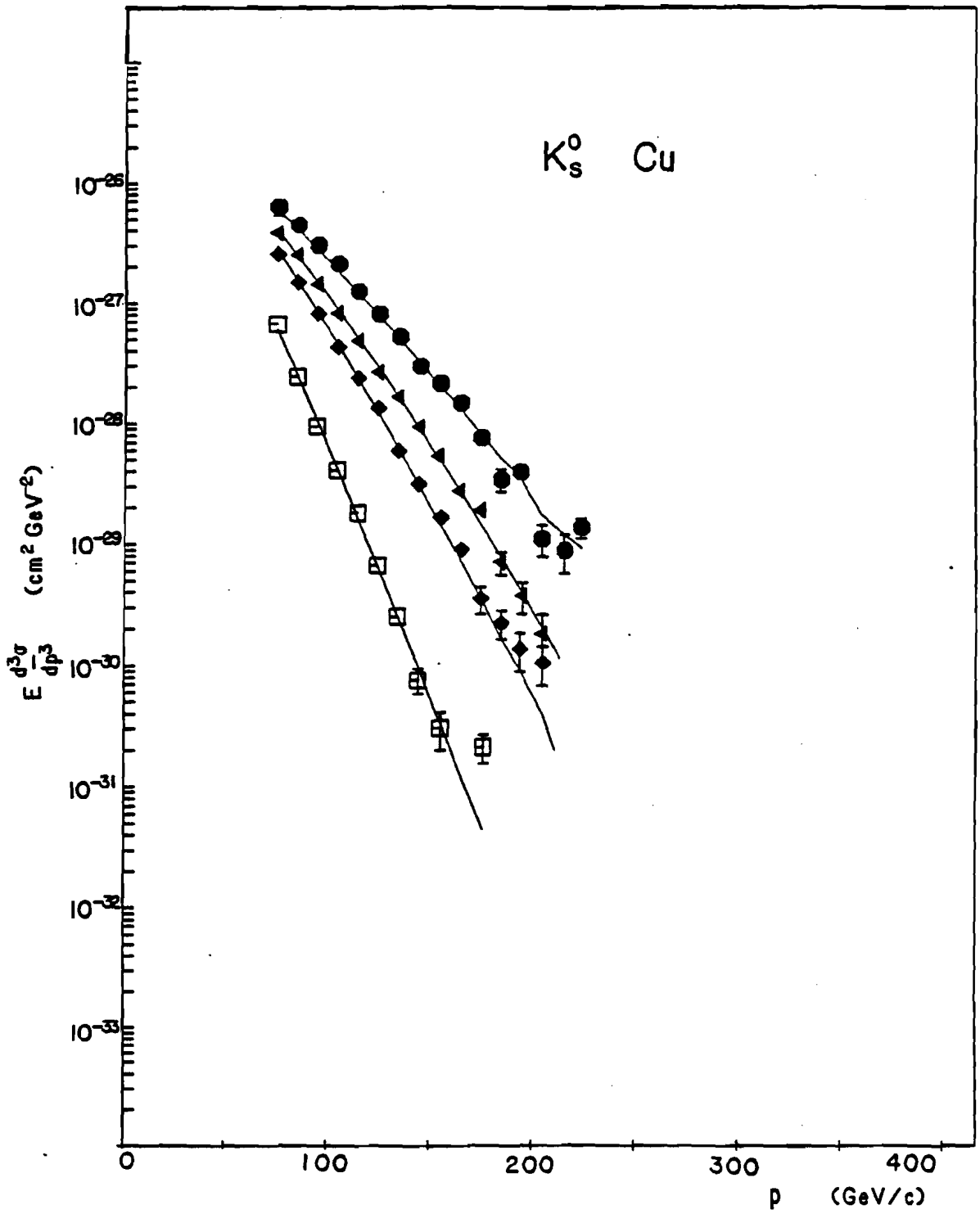
K_s^0 Cu
10^{-26}
10^{-27}
10^{-28}
10^{-29}
10^{-30}
10^{-31}
10^{-32}
10^{-33}
$E \frac{d^3\sigma}{dp^3}$ (cm^2 GeV^{-2})
0
100
200
300
400
p (GeV/c)

Figure 6.6

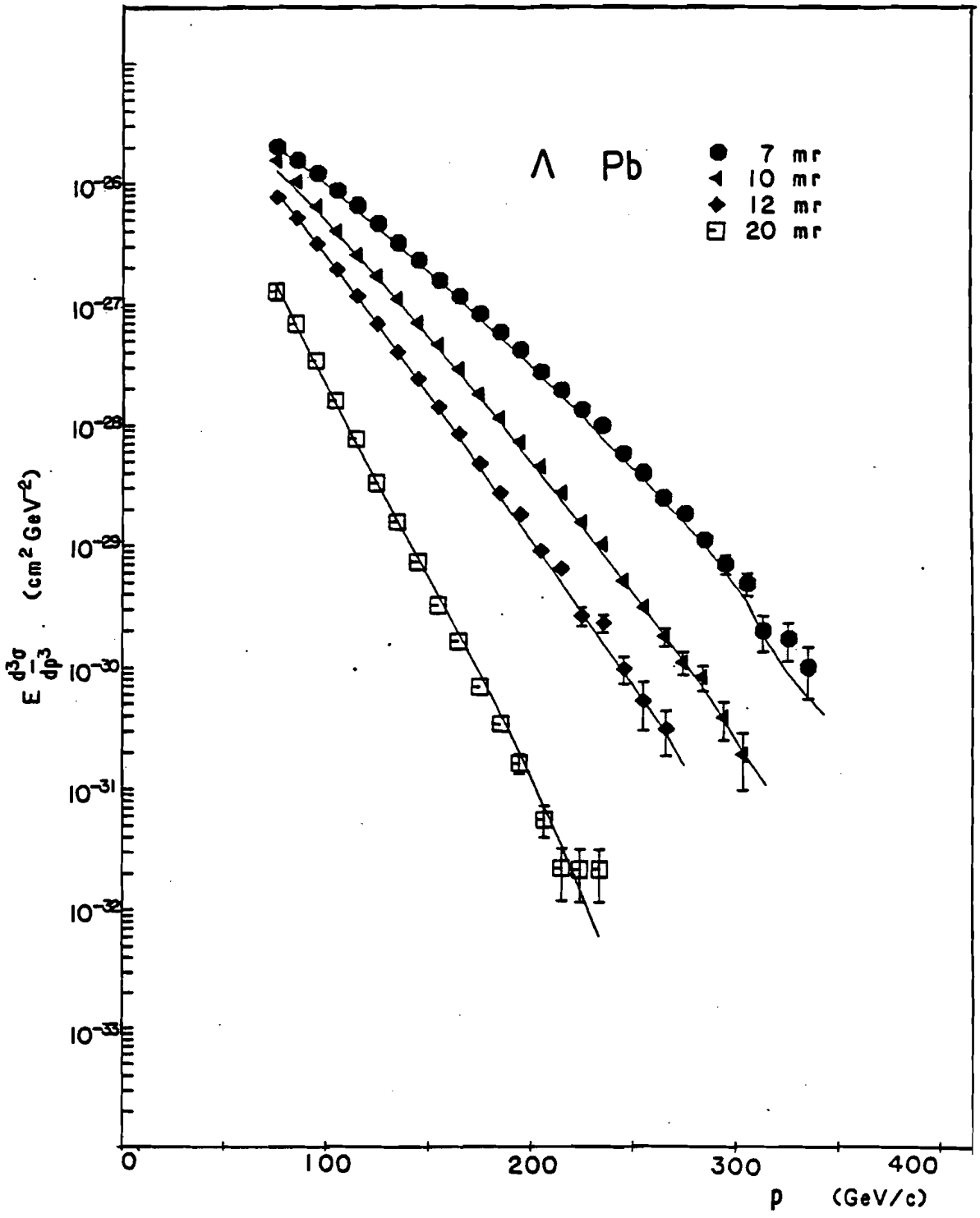
Λ Pb
7 mr
10 mr
12 mr
20 mr
10^{-26}
10^{-27}
10^{-28}
10^{-29}
10^{-30}
10^{-31}
10^{-32}
10^{-33}
$E\frac{d^3\sigma}{dp^3}$ (cm^2 GeV^{-2})
0
100
200
300
400
p (GeV/c)

Figure 6.7

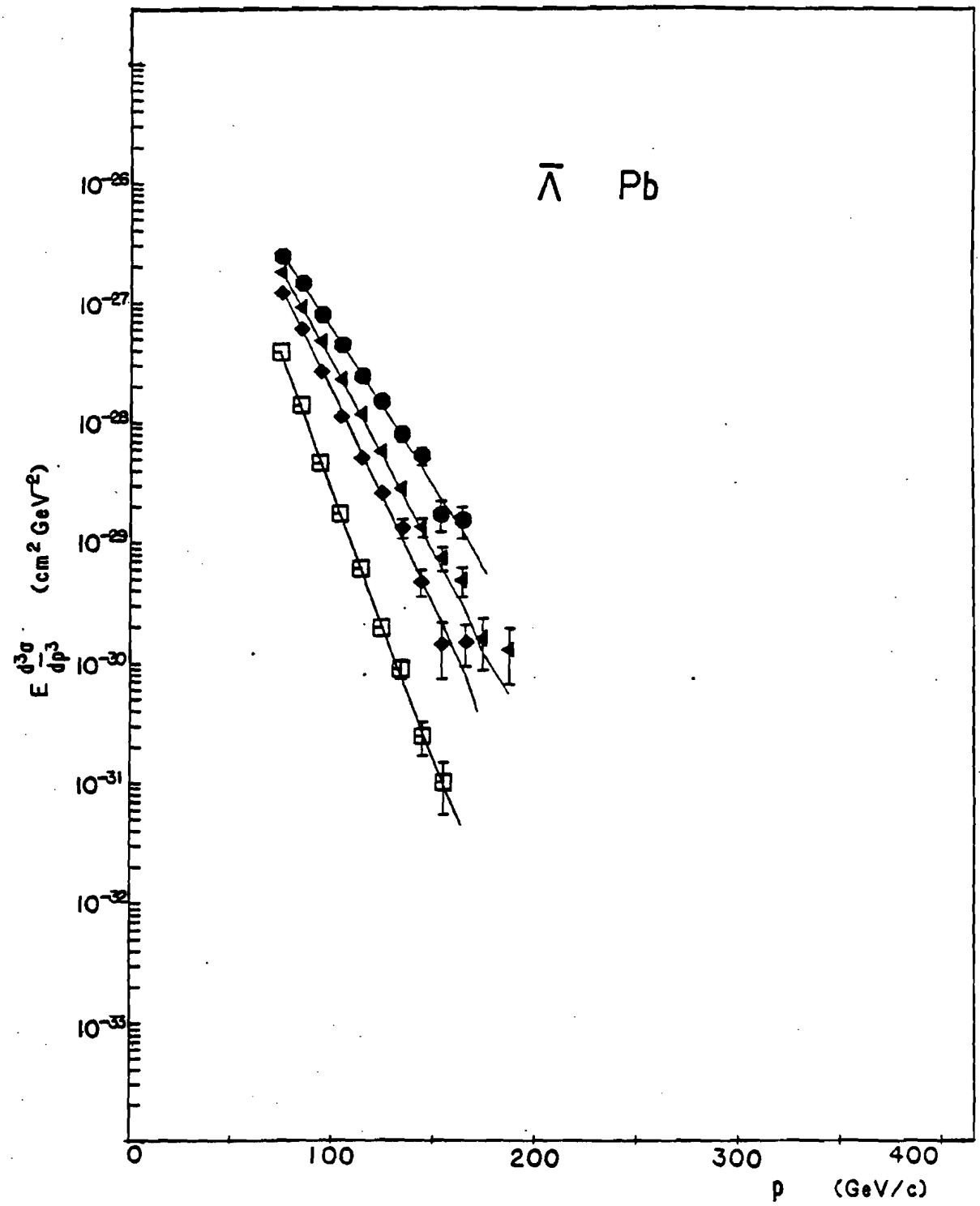
$\bar{\Lambda}$ Pb
$E\frac{d^3\sigma}{dp^3}$ (cm^2 GeV^{-2})
10^{-26}
10^{-27}
10^{-28}
10^{-29}
10^{-30}
10^{-31}
10^{-32}
10^{-33}
0
100
200
300
400
p (GeV/c)

Figure 6.8

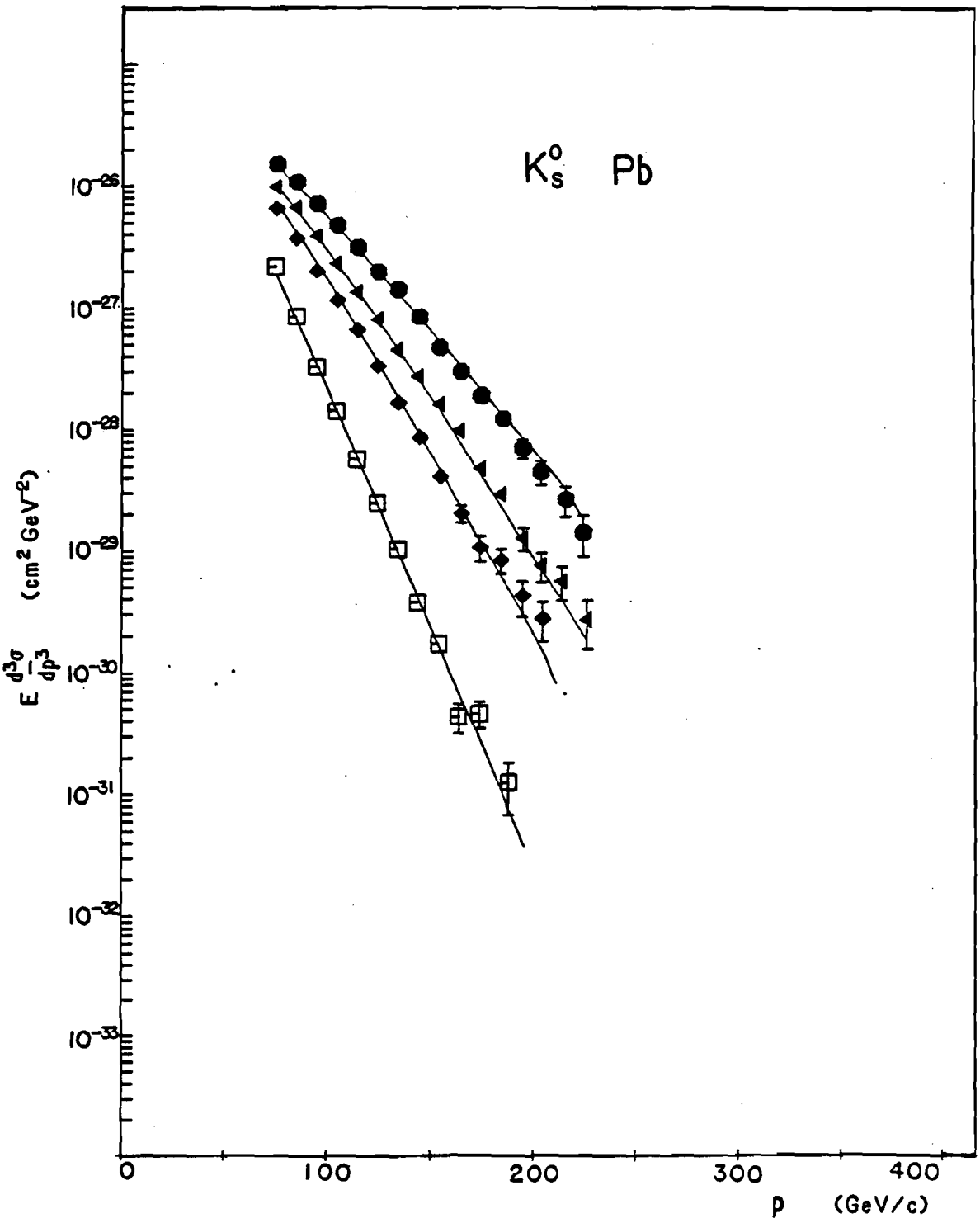
K_s^0 Pb
10^{-26}
10^{-27}
10^{-28}
10^{-29}
10^{-30}
10^{-31}
10^{-32}
10^{-33}
$E\frac{d^3\sigma}{dp^3}$ (cm^2 GeV^{-2})
0
100
200
300
400
p (GeV/c)

Figure 6.9

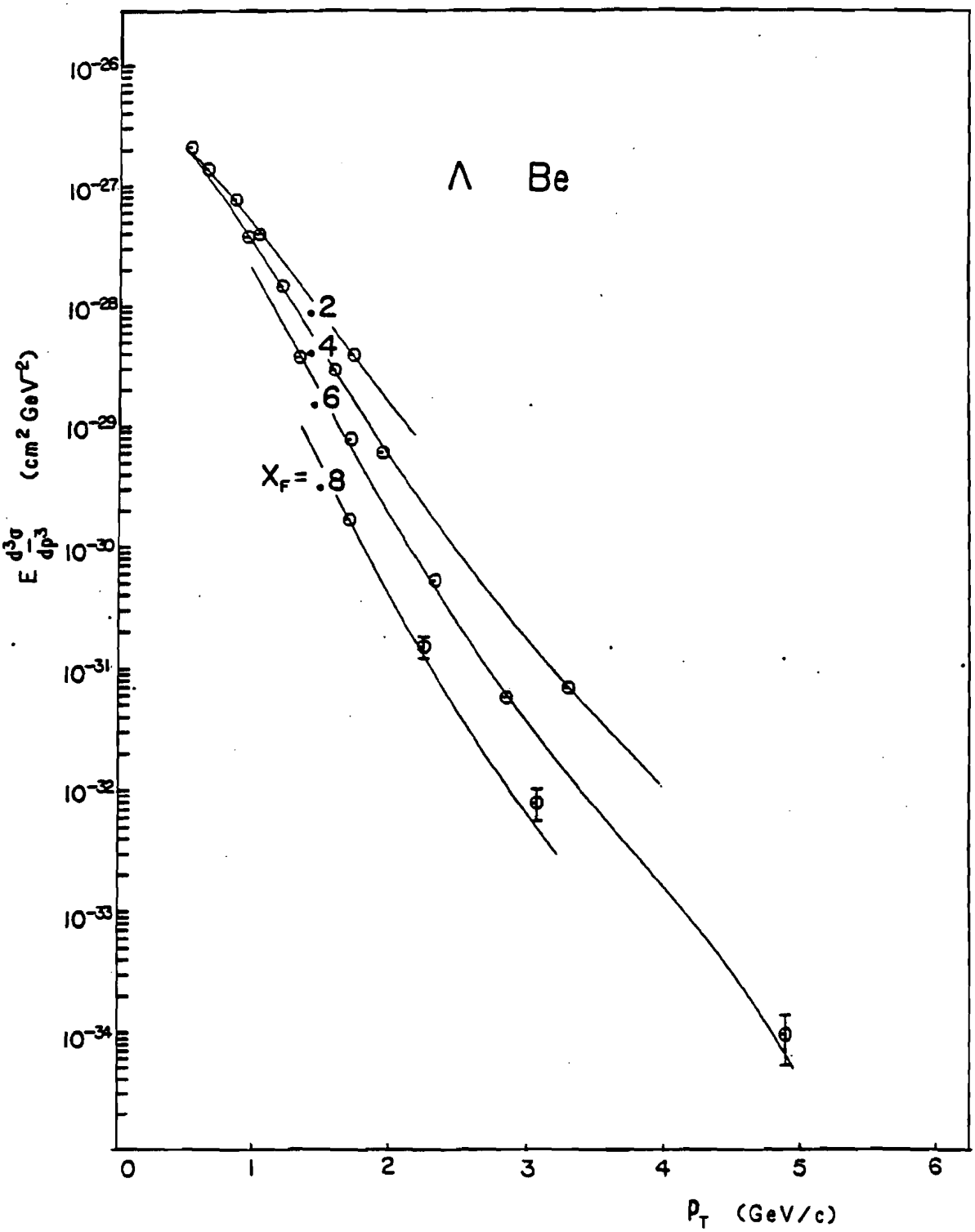

Figure 6.10a The Λ invariant cross sections are shown as a function of p_T for fixed values of x_F using the fits (Section 6.2) to interpolate the data to give the smooth curves.

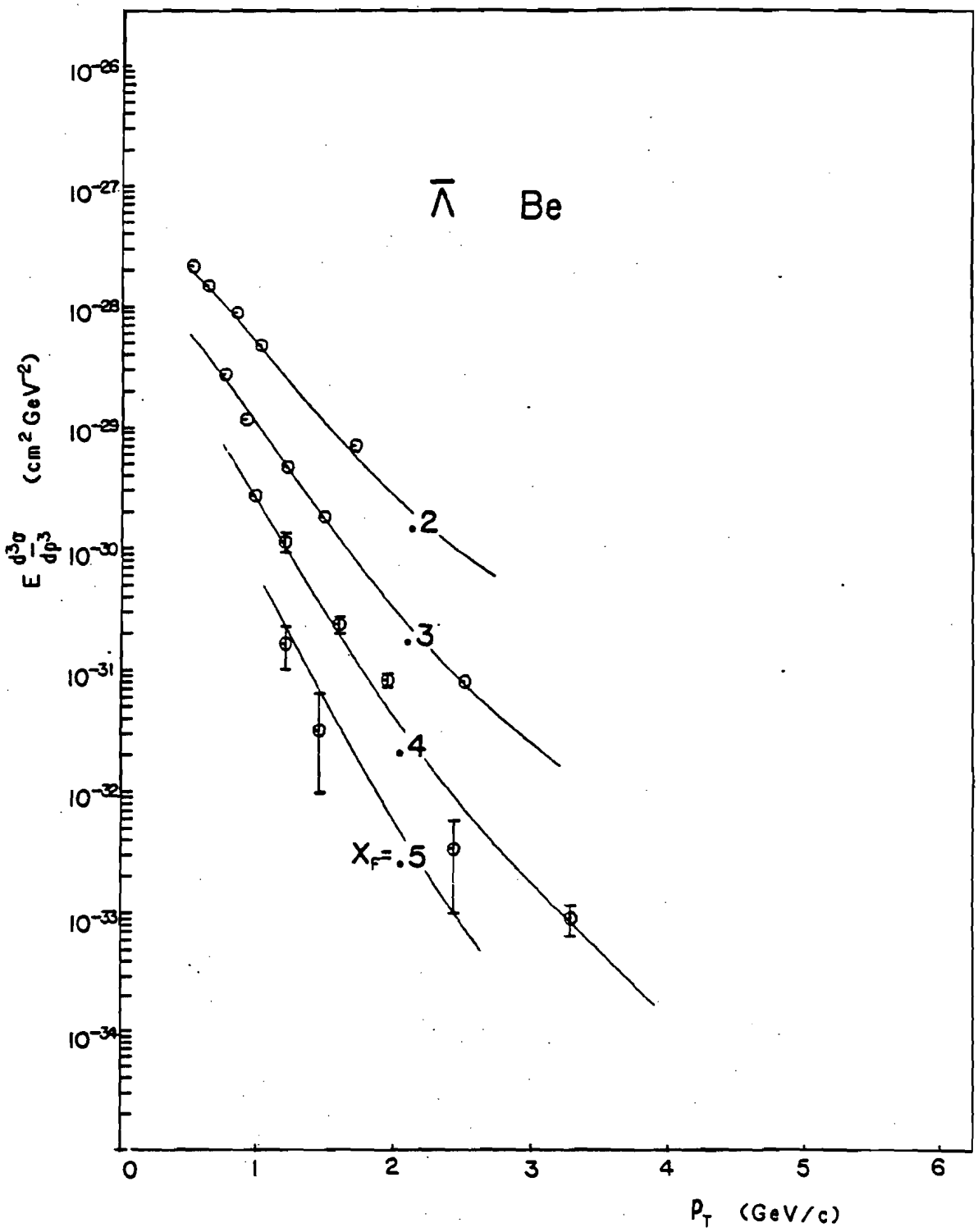

Figure 6.10 b The $\bar{\Lambda}$ invariant cross sections are shown as a function of p_T for fixed values of x_F using the fits (Section 6.2) to interpolate the data to give the smooth curves.

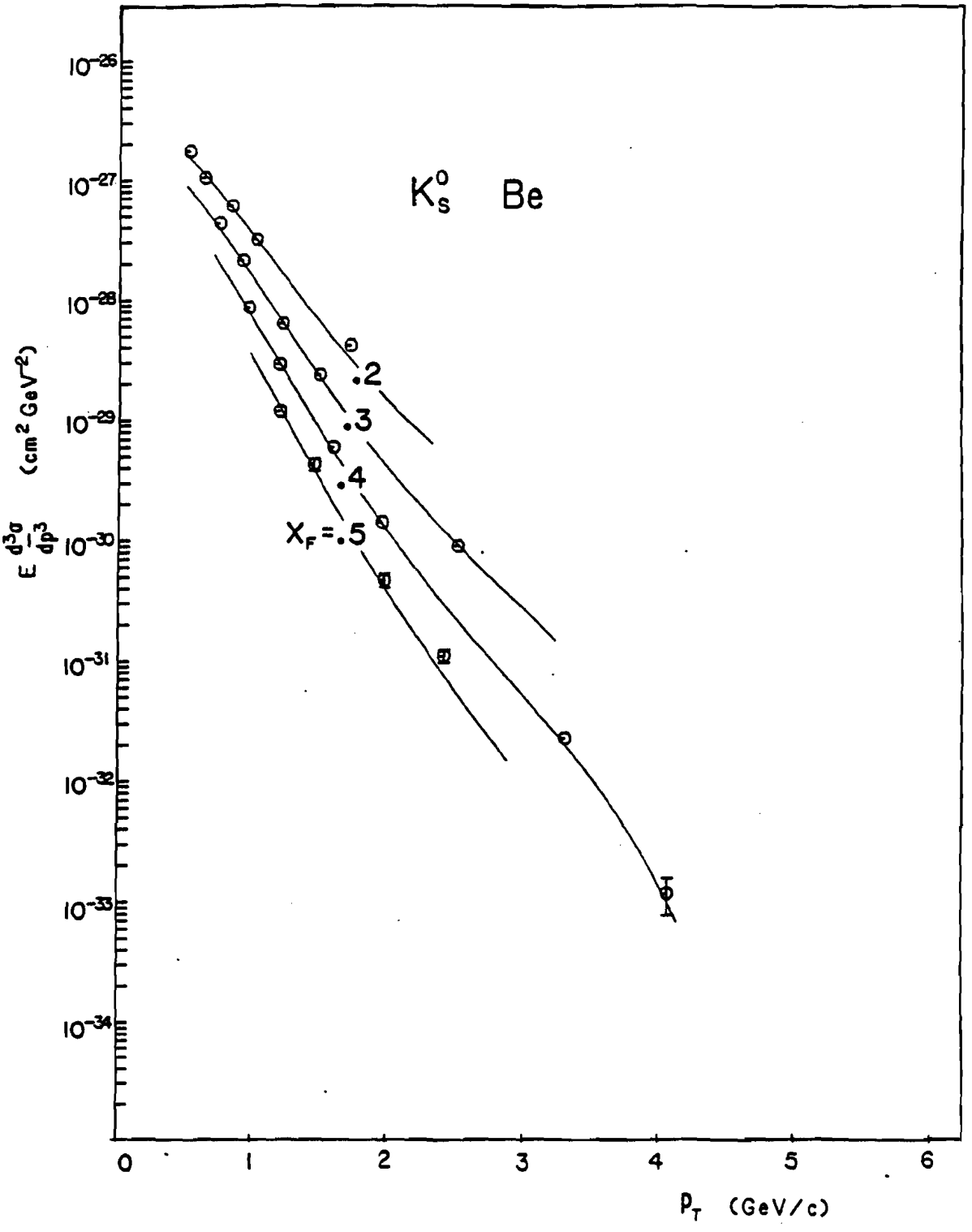

Figure 6.10c The K_S^0 invariant cross sections are shown as a function of p_T for fixed values of x_F using the fits (Section 6.2) to interpolate the data to give the smooth curves.

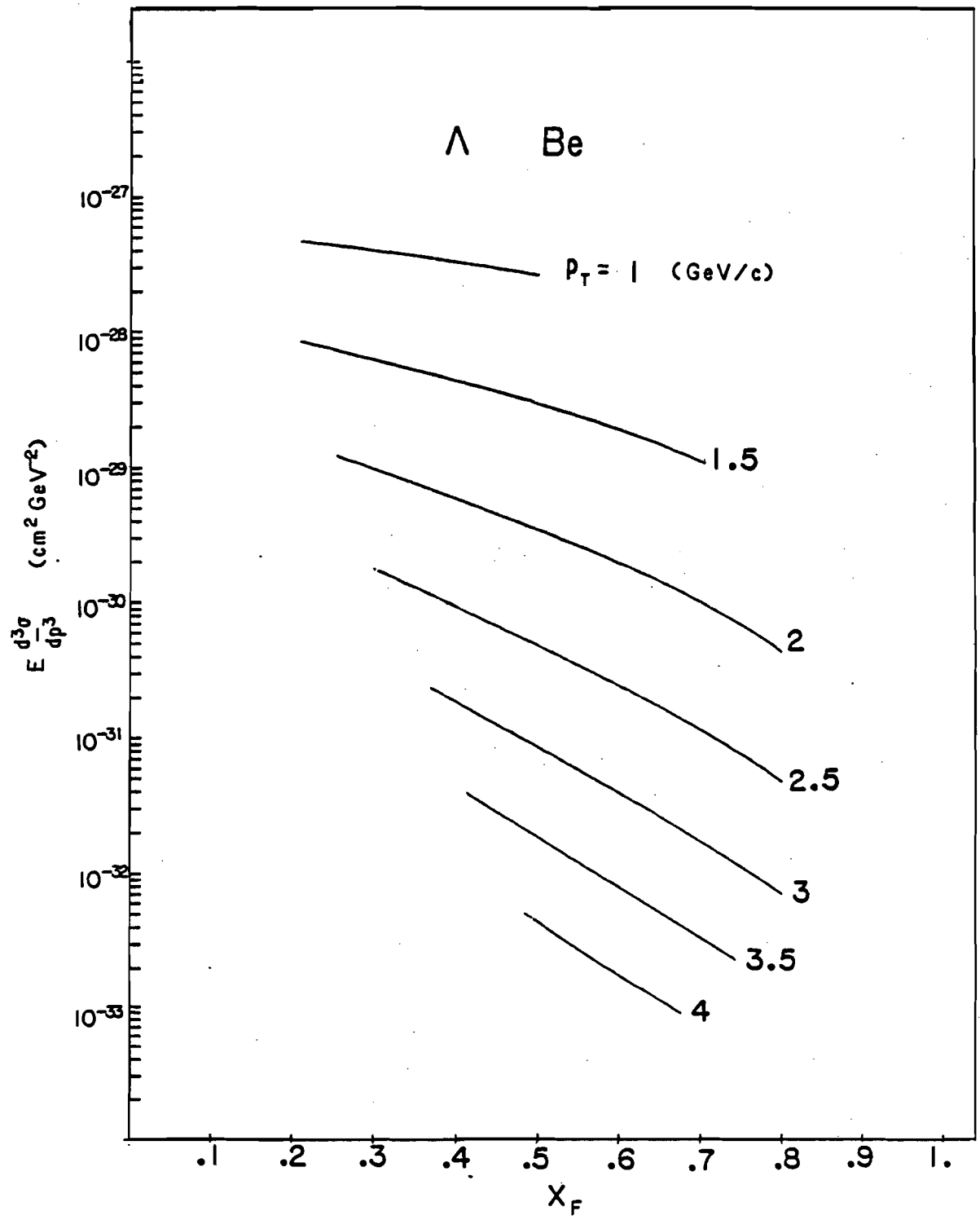

Figure 6.11a The Λ invariant cross sections are shown as a function of x_F for fixed values of p_T using the fits (see Section 6.2) to interpolate the data to give the smooth curves.

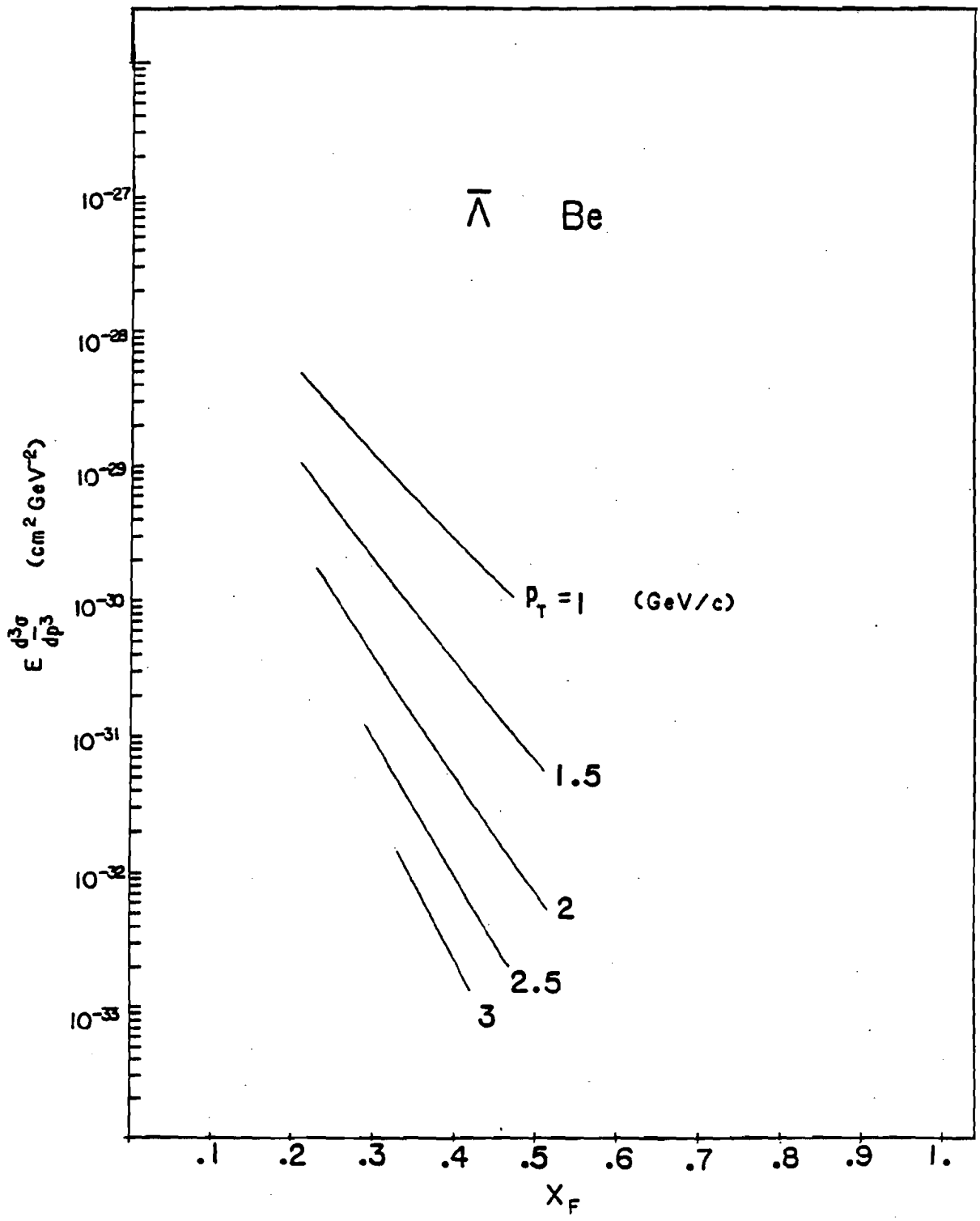

Figure 6.11b The $\bar{\Lambda}$ invariant cross sections are shown as a function of x_F for fixed values of p_T using the fits (see Section 6.2) to interpolate the data to give the smooth curves.

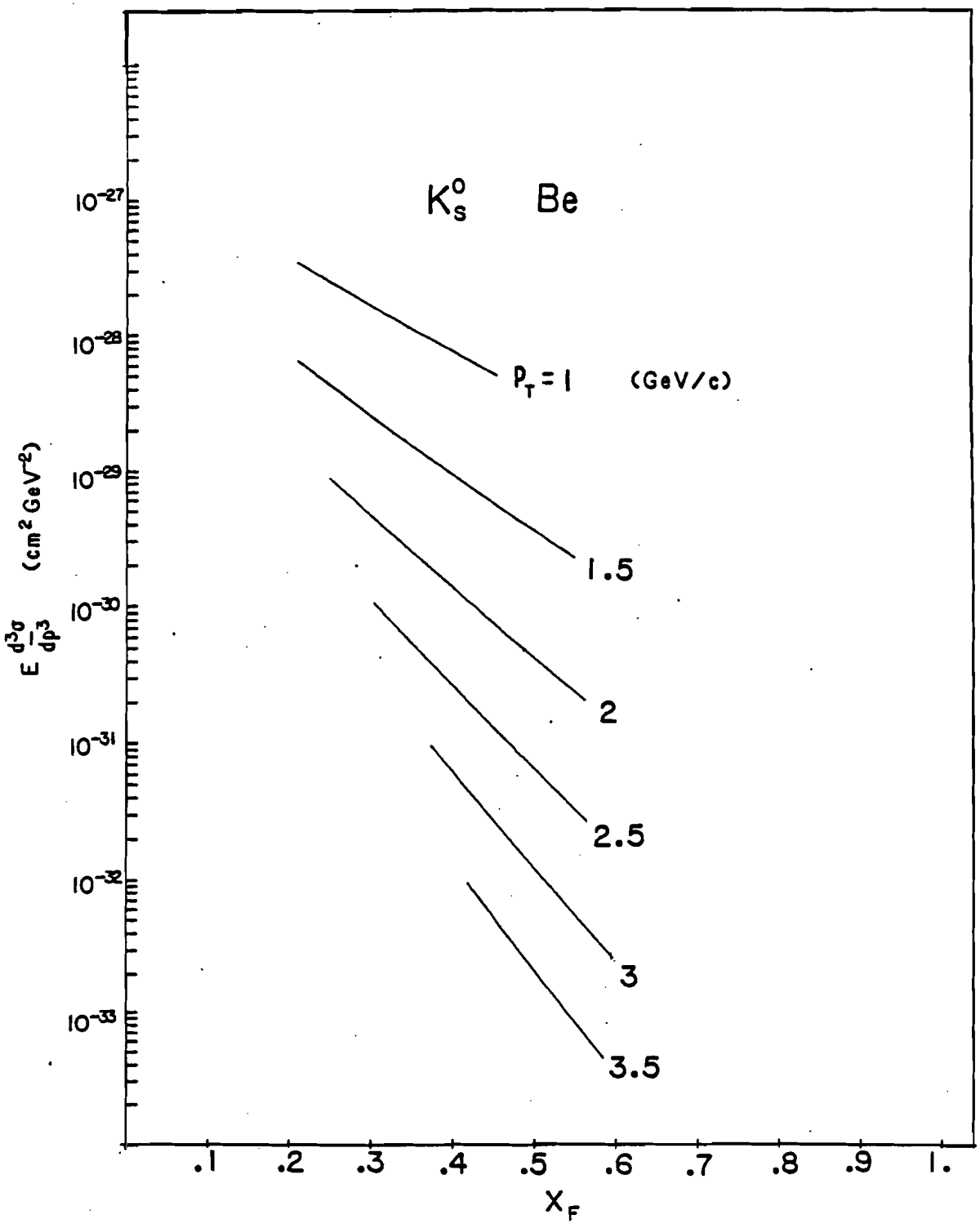

Figure 6.11 c The K_S^0 invariant cross sections are shown as a function of x_F for fixed values of p_T using the fits (see Section 6.2) to interpolate the data to give the smooth curves.

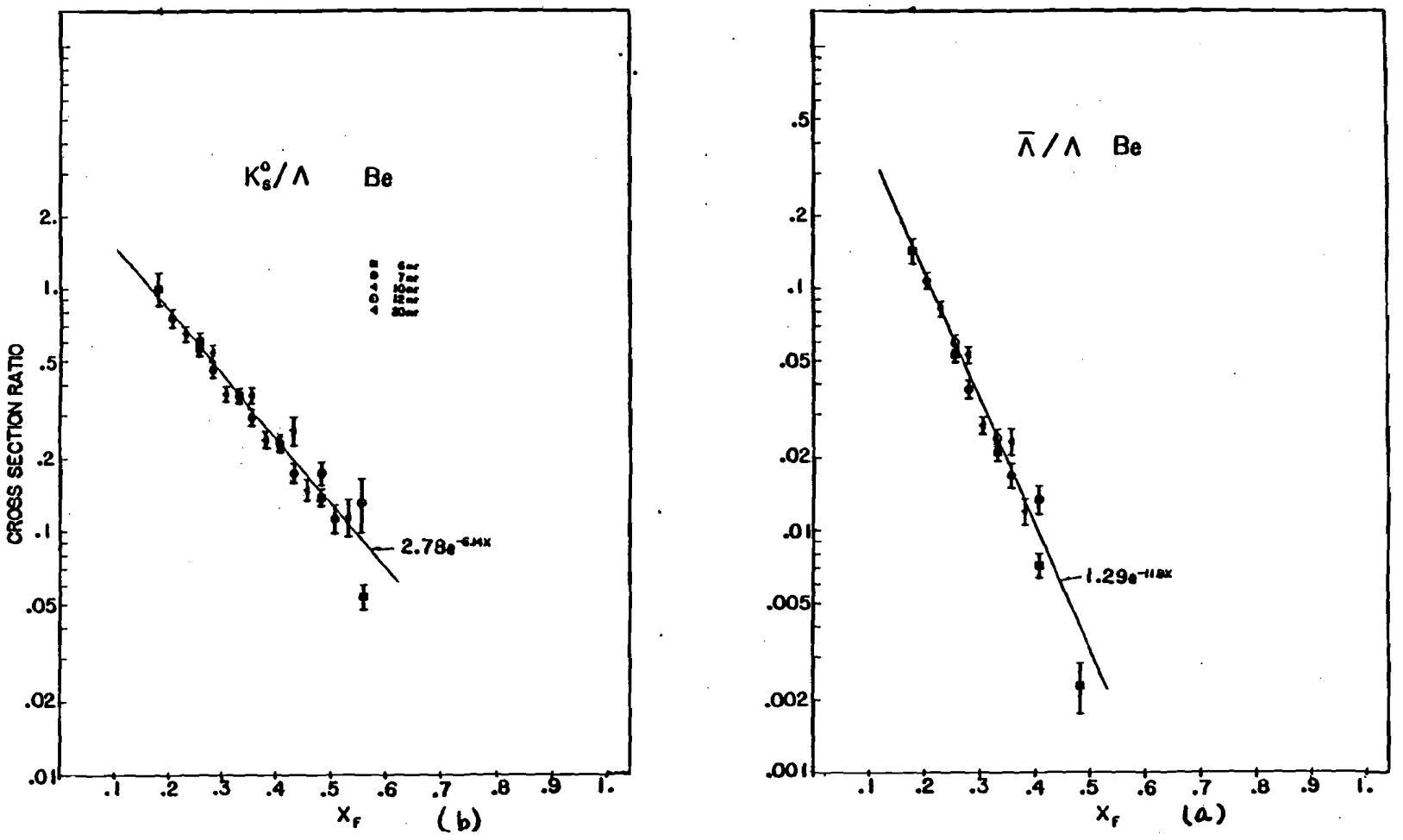

Figure 6.12a The ratio of the $\bar{\Lambda}$ (a) and K_s^o (b) invariant cross sections to the Λ cross section is shown for the beryllium target. The data from all angles and targets has been fit to an exponential function for $\bar{\Lambda}/\Lambda$ and K_s^o/Λ. Note the insensitivity of the ratio to the production angle.

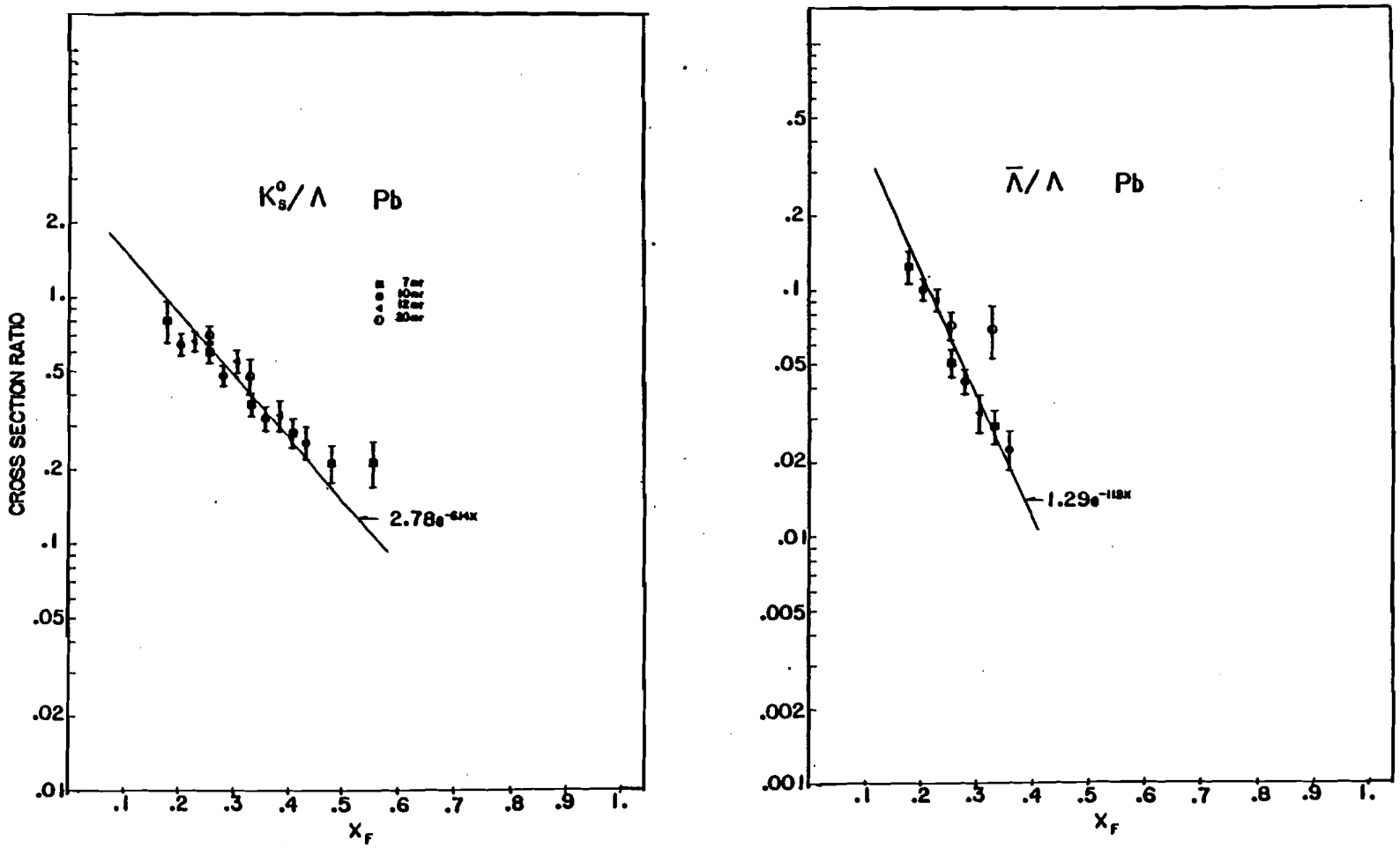

Figure 6.12b The same ratios and exponential fits of Figure 6.12a are shown here for the lead target. There is evidently little or no dependence of the ratio on the target material.

6.3 Discussion of the General Behavior

The cross sections exhibit one outstanding feature which is independent of particle and target; the fixed angle behavior tends to a simple exponential with momentum as $\theta_p \rightarrow$ 20mr. All 20 mr data are very well described by a function of the form A $\exp\{-b_i p\}$ where p is the momentum of particle $i=\Lambda$, $\bar{\Lambda}$, or K^0_s. For the Be data, $b_\Lambda=0.082\pm0.012$, $b_{\bar{\Lambda}}=0.127\pm0.018$, and $b_K=0.091\pm0.013$.

From Figs 6.10-6.12 one can see that the dependence on x_F is exponential for both the $\bar{\Lambda}$'s and K^0_s's, but for the Λ's the contours are not as steep and are described better by a product of an exponential and the form $(1-x_F)^n$ where n depends somewhat on p_T. This behavior becomes more evident at $p_T=0$ [11], and is typical of particles which can be created as fragments of the incident projectile (the 400 GeV proton). The $\bar{\Lambda}$'s show a much different behavior which is sharply peaked as $x_F \rightarrow 0$. A related observation is that the ratio of the to cross section extrapolates to near 1 as $x_F \rightarrow 0$. All of these features correlate well with the quark model since the Λ (uds) can be formed from the incident proton (uud) by the exchange of just one constituent (u->s). None of the constituents of the $\bar{\Lambda}$ ($\bar{u}\bar{d}\bar{s}$) exist as valence quarks in the initial system. However, the quark content of the products makes little difference near $x_F=0$ because the available energy is much

greater than the particle masses.

The transverse momentum dependence of the cross sections is qualitatively similar for all three particles: exponential behavior at small p_T (0.7 GeV/c<p_T< 2 GeV/c) with small but statistically significant deviations from an exponential beyond about 2 GeV/c. This can be seen in Figs 6.10 where x_F is fixed.

Another approach to assess the p_T dependence can be taken which isolates the kinematic behavior at all p_T. "Kinematic behavior" here indicates that part of the differential cross section behavior that depends on the proximity of the kinematic limits imposed through the relation,

$$E^*_{max} = \frac{s-M_x^2+M_h^2}{2\sqrt{s}} \qquad (6.3)$$

where M_x is the smallest mass for the unobserved particles consistent with conservation laws. For small p_T and large s, x_F is a good kinematic variable, but for the points where p_T is a significant fraction of $\sqrt{s}/2$ the transverse boundary comes into play. Therefore, another quantity is introduced called radial x or x_R defined as,

$$x_R = \frac{E^*}{E^*_{max}} \qquad (6.4)$$

The kinematic boundary is just $x_F=1$. It has been observed that inclusive reactions of charged hadrons and π^0 scale (i.e. independent of $\sqrt{s}$) at fixed x_R and p_T for $\sqrt{s} \gtrsim 10$ GeV [13].

At the Fermilab energy $\sqrt{s}$= 27.3 GeV, Eqn (6.4) can be approximated by,

$$x_R \simeq \sqrt{x_F^2+x_T^2+4m_\Lambda^2/s} \qquad (6.5)$$

where x_T is analogous to x_F, $x_T=2p_T/\sqrt{s}$. For a produced at 20 mr with p_T= 5 GeV/c; x_F=0.625, x_R=0.723, and x_T=0.36. Clearly there is no significant distinction between x_R and x_F for p_T< 2 GeV/c. The cross sections as a function of p_T for fixed x_R are shown in Figs. 6.13a-c. The data from Ref. [6] was taken at $\sqrt{s}$ = 23.8 GeV (300 GeV in lab). The curves are functions fit to all the data points shown of the form,

$$E\frac{d^3\sigma}{dp^3} = A\left[1+\frac{p_T^2}{m^2}\right]^{-n} \qquad (6.6)$$

where A, m^2 ,and n are fitted parameters which are tabulated in Table 6.1. Since the data from this experiment extends to a much larger p_T than any other Λ experiment to date, one cannot show that radial scaling holds for large p_T. It must be assumed. Nevertheless, Eqn (6.6) provides a means of comparing production of different hadrons since this

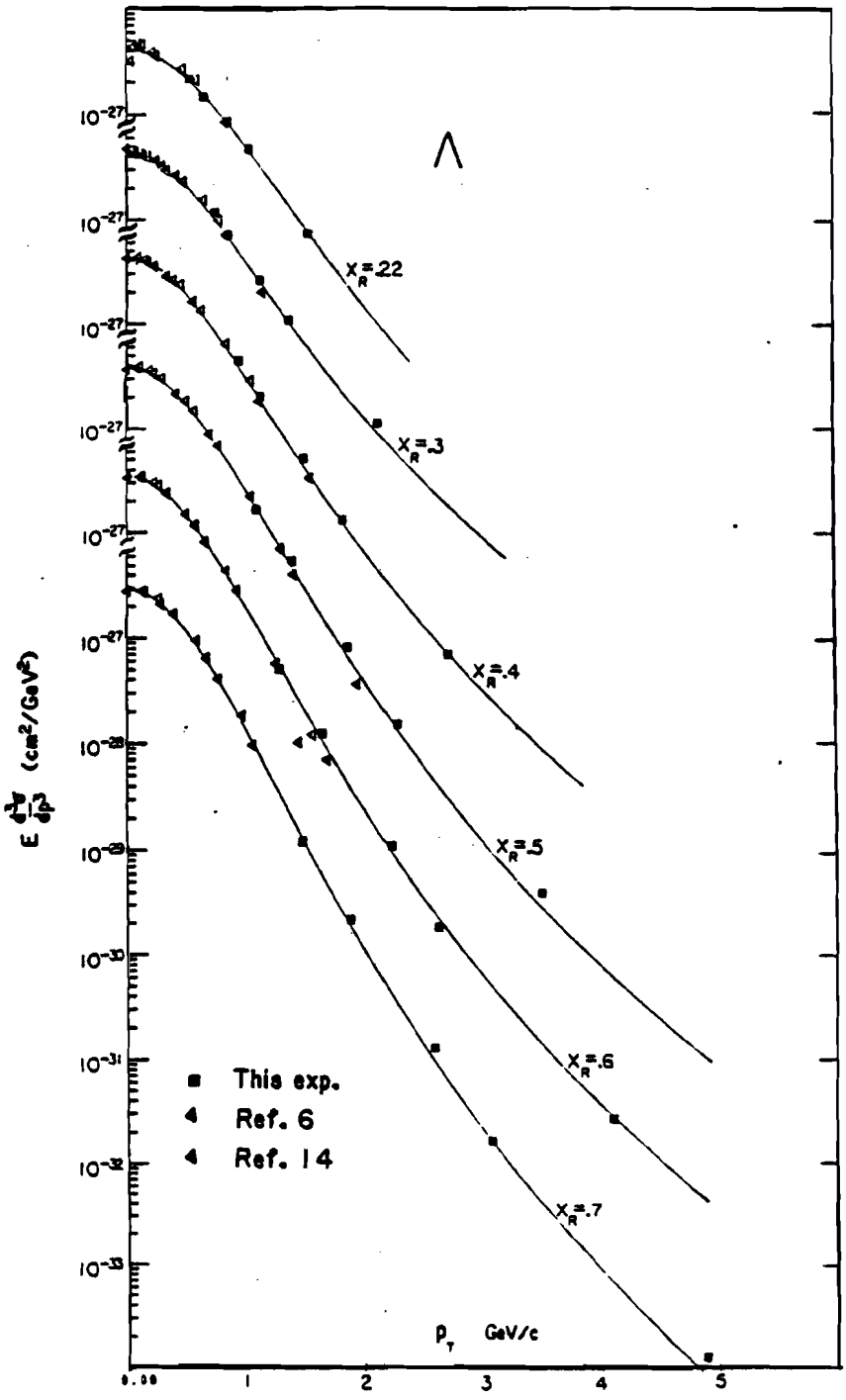

Figure 6.13a Data from $\sqrt{s}$=27.4 GeV and $\sqrt{s}$=23.7 GeV (Ref. 6) are shown for the Λ's at constant x_R. Note that the scale is multi-valued to artificially spread the data apart for clarity.

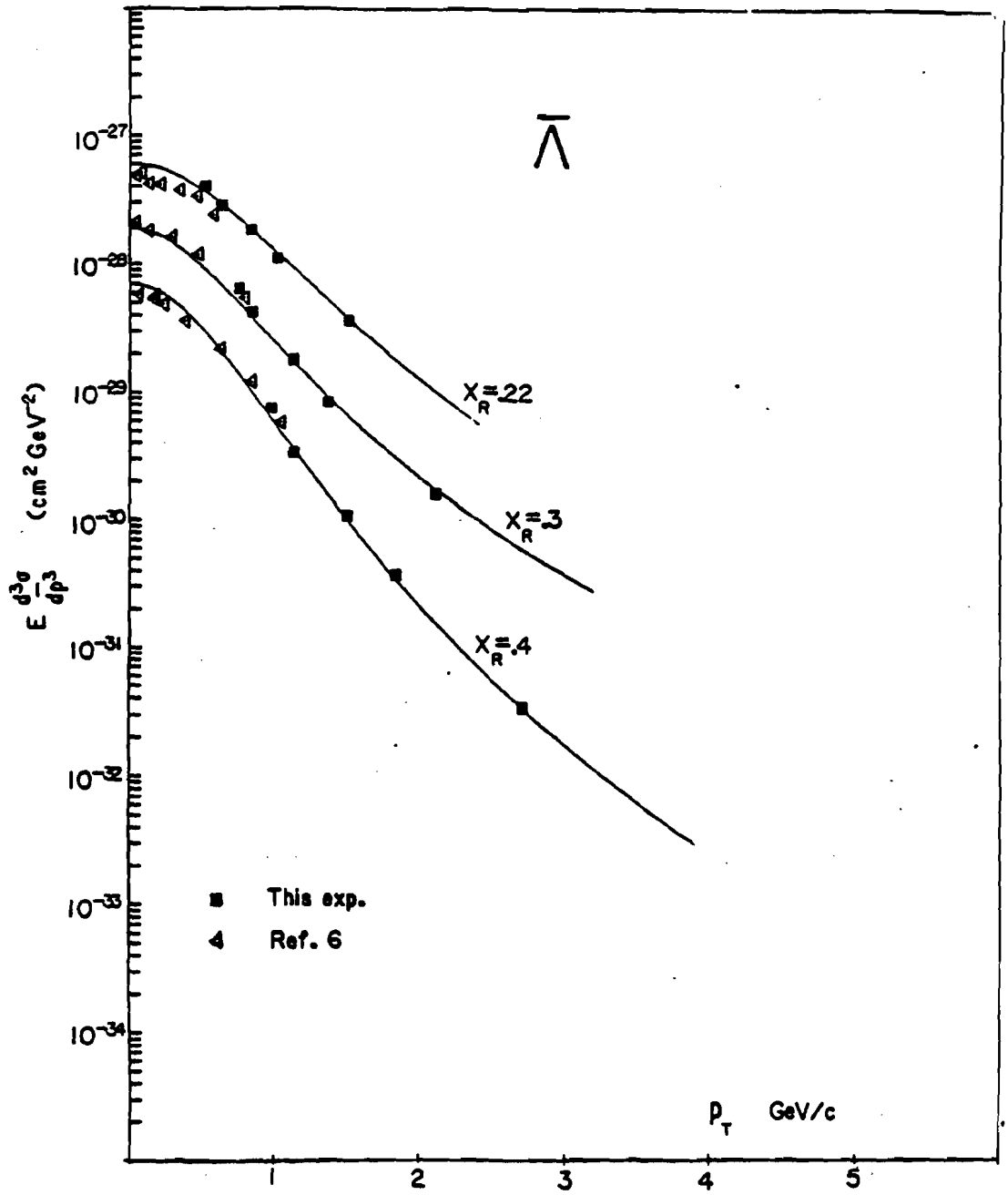

Figure 6.13b The $\bar{\Lambda}$ cross sections are plotted at constant x_R versus p_T with the fits from Table 6.1 shown as solid curves. The data from Ref. 6 were taken at 300 GeV.

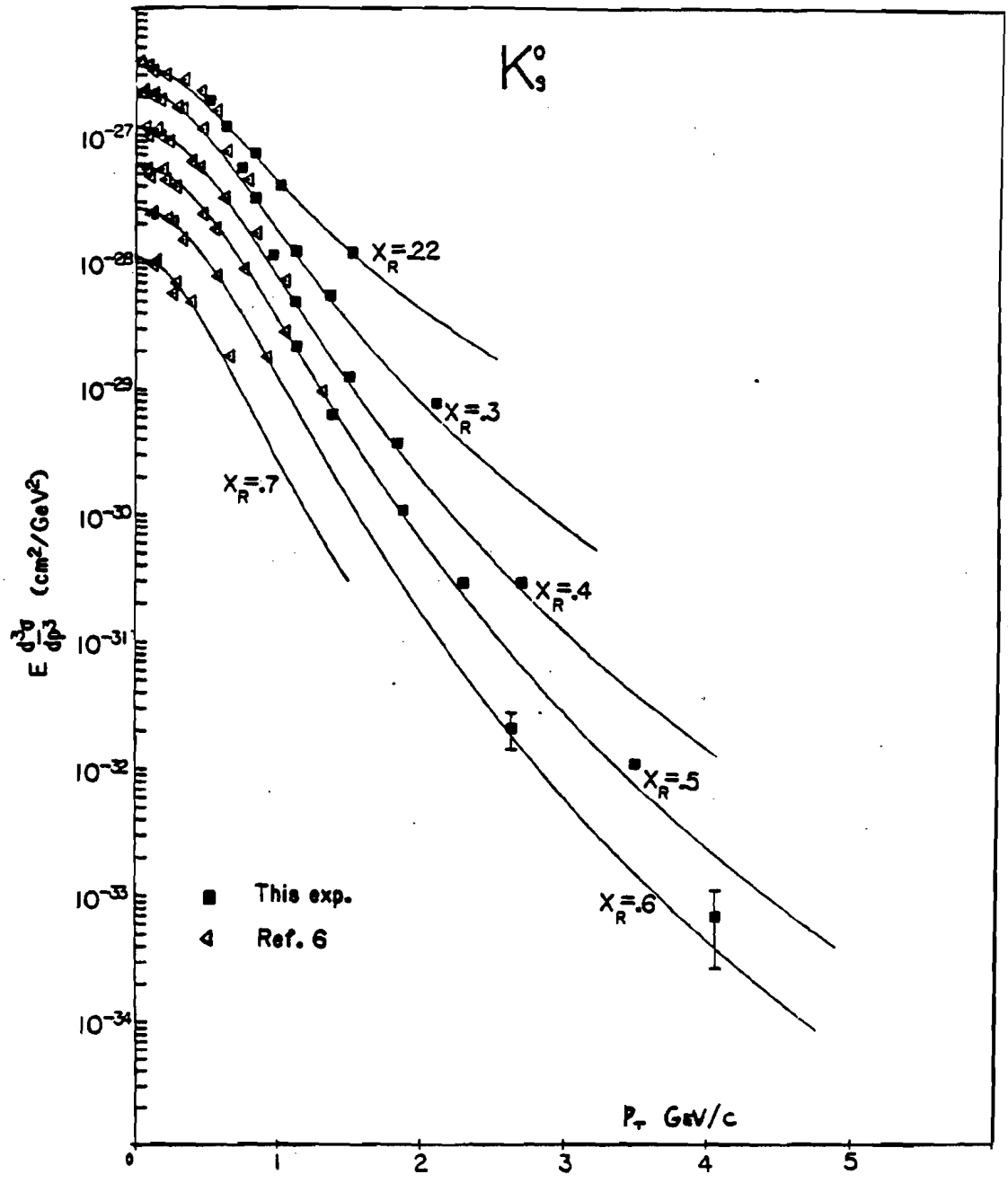

Figure 6.13 The K^0_S cross sections are plotted at constant x_R versus p_T with the fits from Table 6.1 shown as solid curves. The data from Ref. 6 were taken at 300 GeV.

	Λ	$\bar{\Lambda}$	K^0_s
x_R=0.22			
A	4.14±.08	0.607±.038	3.56 ±.13
m^2	1.87±.15	1.34 ±.180	0.630±.056
n	4.89±.91	2.81 ±.52	2.21 ±.19
χ^2/df	34/12	16/9	12/10
x_R=0.3			
A	4.48±.06	0.36±.04	2.29±.07
m^2	1.22±.08	0.58±.07	0.82±.06
n	4.01±.15	2.65±.03	3.20±.11
χ^2/df	14/18	34/8	10/13
x_R=0.4			
A	4.36±.06	0.071±.022	1.18±.06
m^2	1.33±.01	1.01 ±.17	1.05±.07
n	4.66±.02	3.64 ±.38	4.07±.13
χ^2/df	23/18	34/11	19/13
x_R=0.5			
A	3.95±.06		0.58±.05
m^2	1.55±.05		1.26±.10
n	5.43±.09		4.75±.17
χ^2/df	37/18		8/12
x_R=0.6			
A	3.56±.06		0.27±.07
m^2	1.52±.06		1.19±.81
n	5.66±.11		5.0 ±2.8
χ^2/df	14/17		6/7
x_R=0.7			
A	2.95±.06		0.11±.06
m^2	1.59±.08		0.66±1.1
n	6.26±.17		4. ±6.
χ^2/df	13/14		4.1/4

Table 6.1 Values of the fitted parameters of Eqn (6.6) describing the behavior of $Ed^3\sigma/dp^3$ at fixed x_R.

form seems to describe inclusive production of all hadrons reasonably well.

Note that for each particle the values for n in Table 6.1 tend to increase with x_R and that m^2 is approximately constant for all x_R. The parameter A does not vary much with x_R for Λ's (appropriate for a leading particle) while for $\bar{\Lambda}$ and K^0_s production A falls rapidly with x_R. These observations are consistent with those in Ref. 13.

6.4 Target Nucleon Dependence

The target nucleon dependence, or simply the A dependence (A is the atomic number of the nucleus) was derived from the cross sections computed from data taken with the beryllium, copper and lead targets. It has become traditional to express the A dependence in terms of an exponent which is a function of the variables x_F and p_T such that,

$$E\frac{d^3\sigma}{dp^3}(A) = A^{\alpha}\, E\frac{d^3\sigma}{dp^3}(A=1) \qquad (6.7)$$

This form is not motivated by theory but is empirically observed to hold. Figure 6.14 shows an example of how well this power fits the data from this experiment. Other

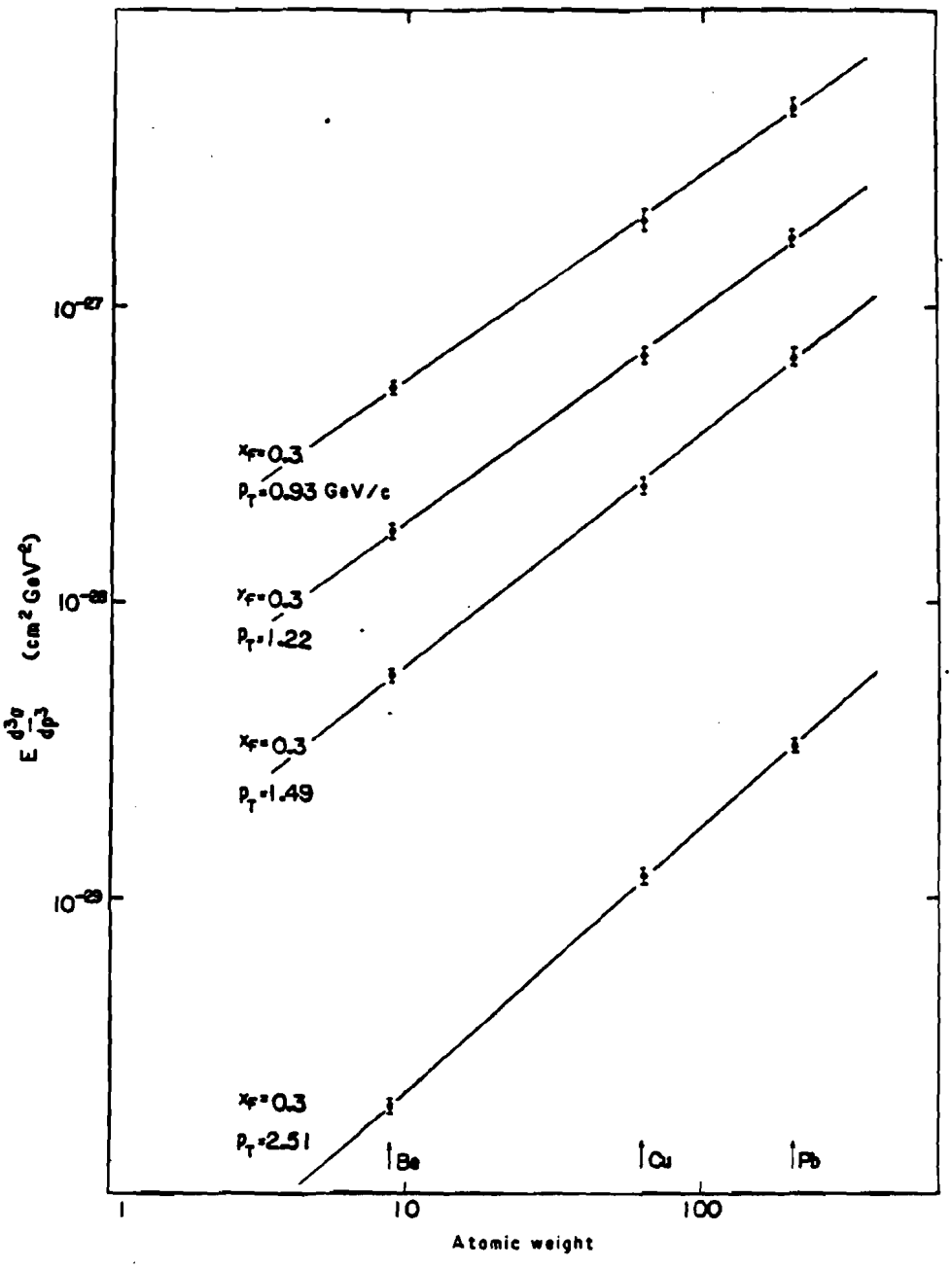

Figure 6.14 The data from the three targets are fit well with a power law hypothesis Eqn.(6.8) for all X_F including x_F=0.3 shown here.

experiments have verified this behavior for a larger number of targets [19].

The value of $\alpha(x_F, p_T)$ was computed by making a least squares fit to all three data points (Be, Cu, Pb) and the results are tabulated in Appendix D. In Figs. 6.15- 6.17 $\alpha(x_F, p_T)$ is plotted as a function of p_T for fixed values of x_F, and is derived from the fitted beryllium and lead interpolations (Eqn. (6.2)).

The rate of increase of α with p_T appears to depend on the particle type, with $d\alpha/dp_T$ being larger for $\bar{\Lambda}$ and K^0_S compared to Λ for $p_T < 2$ GeV/c. Data for charged particles shows that there is a maximum value for at approximately 4-6 GeV/c [20]. There are some indications of this behavior for the neutral particles Λ and K^0_S at the large p_T extreme of the data. Data from Ref [6] is also shown in the figures (300 GeV data). For $\bar{\Lambda}$'s and K^0_S's both data sets match at the values of $\alpha(x_F, p_T)$ common to both to within 8% in (the statistical errors in α are about 4%). In Figs. 6.15-6.17 the superposed curves shown are the results of simultaneously fitting both sets of data (this experiment's and that of Ref. 6) for beryllium and lead targets.

The exponent α behaves in a way that can be given a qualitative explanation. At p_T near 0, which is the part of phase space that dominates the total cross section, one would expect that α is mostly due to geometrical effects.

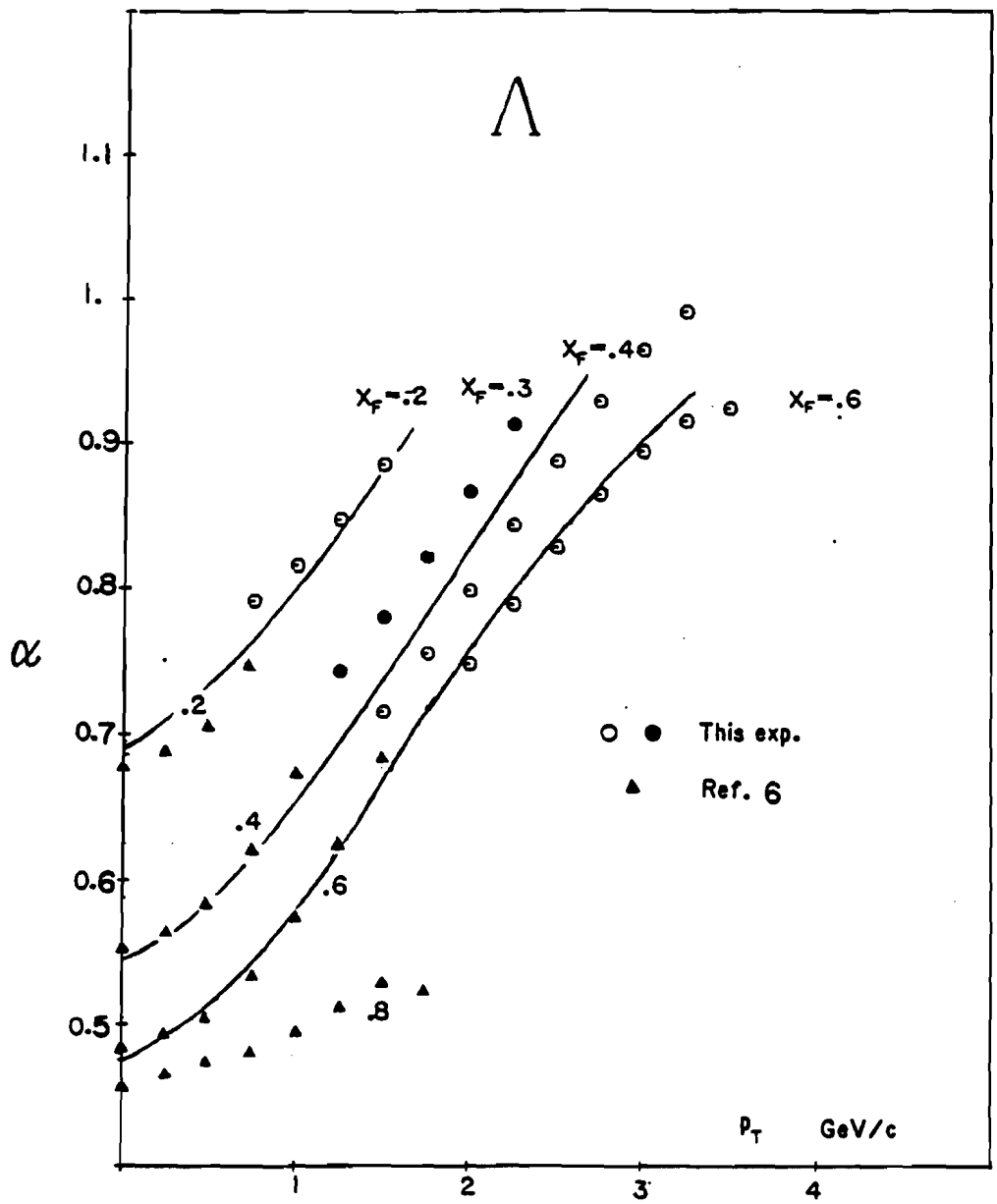

Figure 6.15 The values of α_Λ as a function of p_T are shown using the Pb and Be cross section fits, Eqn.(6.2). The data from Ref. 6 were taken at 300 GeV. The solid curve is the result of a fit of the form Eqn.(6.2) to both sets of data simultaneously for x_F = 0.2, 0.4 and 0.6.

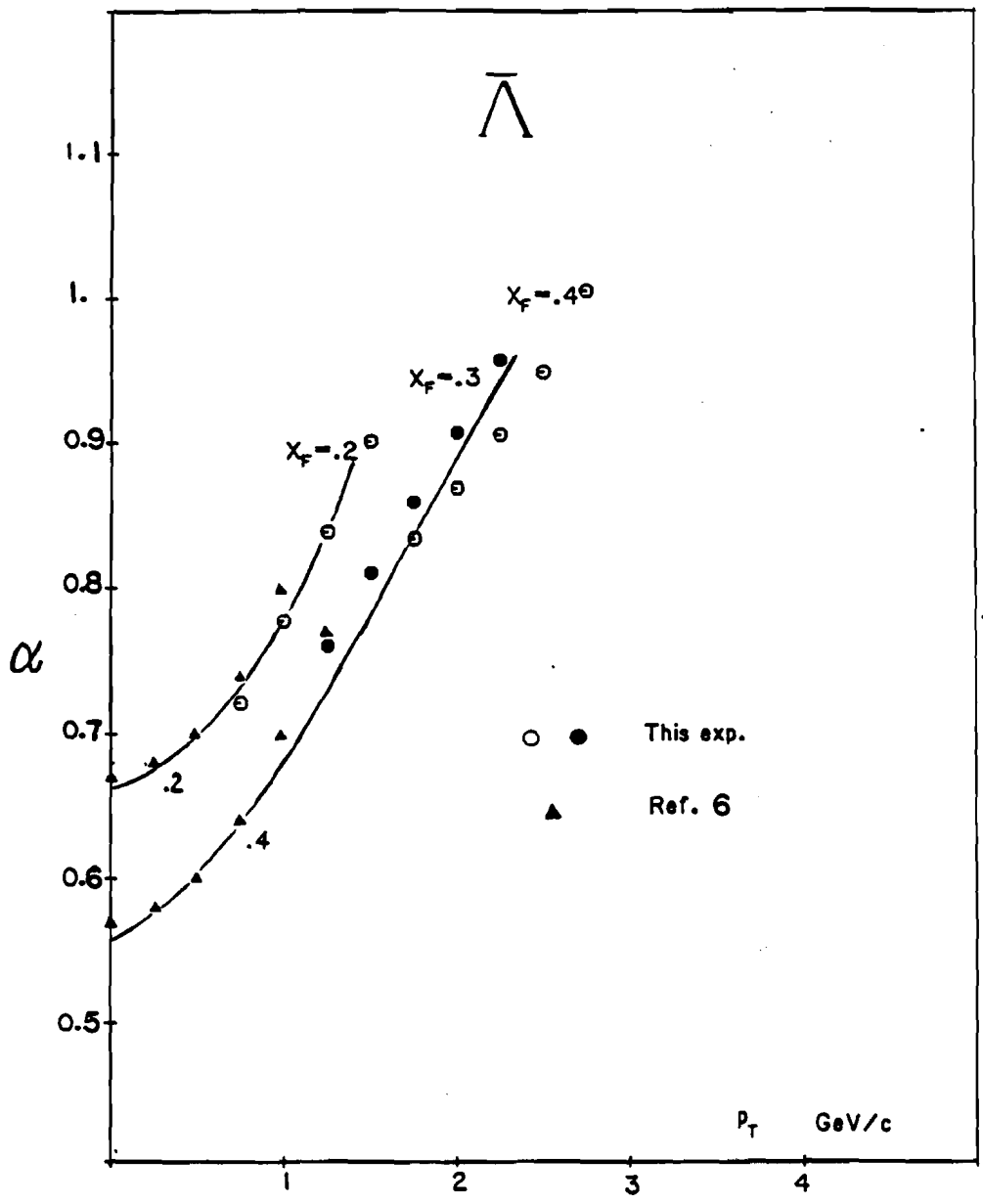

Figure 6.16 The values of $\alpha_{\bar{\Lambda}}$ as a function of p_T are shown using the Pb and Be cross section fits, Eqn.(6.2). The data from Ref. 6 were taken at 300 GeV. The solid curve is the result of a fit of the form Eqn.(6.2) to both sets of data simultaneously for x_F = 0.2 and 0.4.

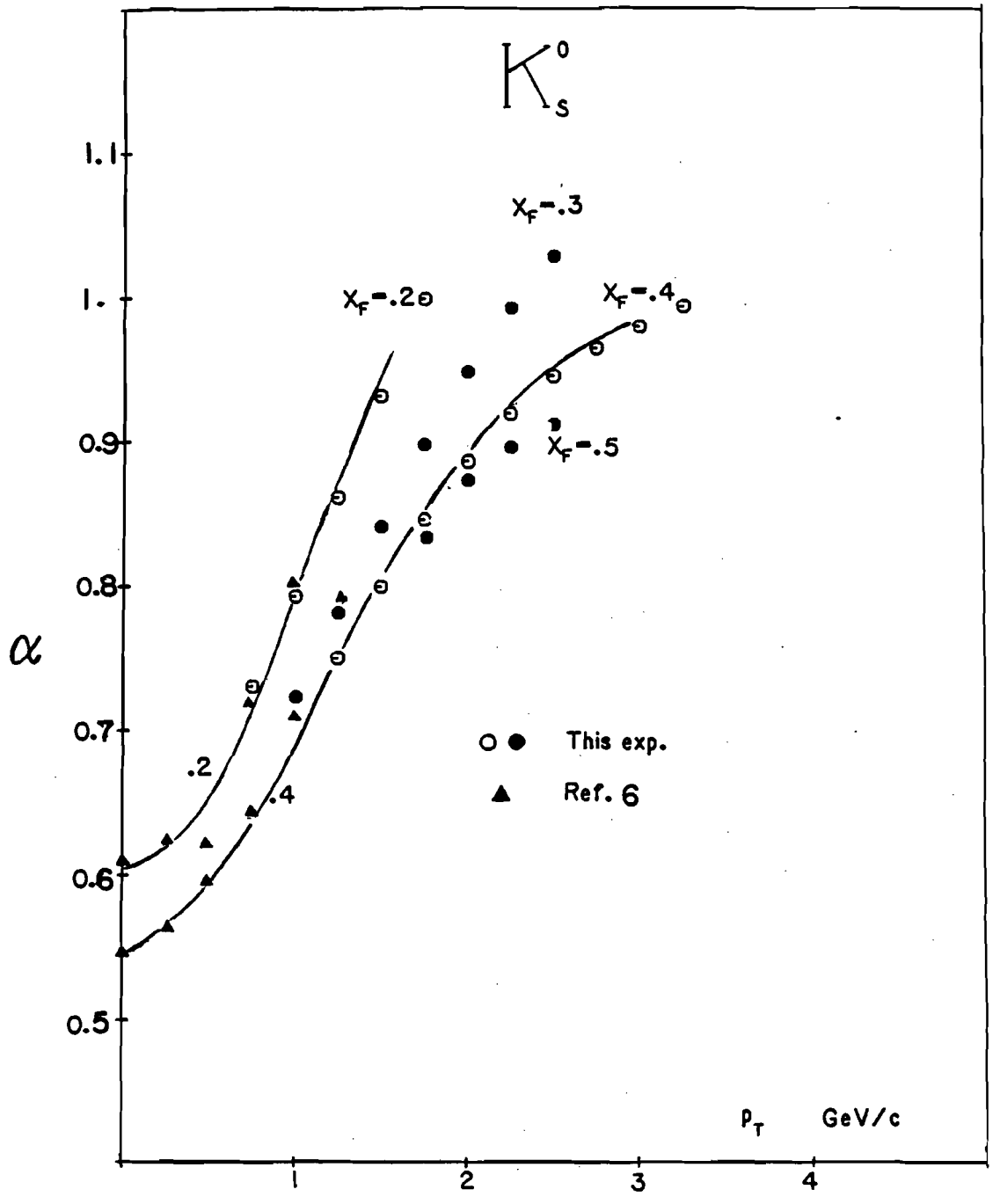

Figure 6.17 The values of α_K as a function of p_T are shown using the Pb and Be cross section fits, Eqn.(6.2). The data from Ref. 6 were taken at 300 GeV. The solid curve is the result of a fit of the form Eqn.(6.2) to both sets of data simultaneously for x_F = 0.2 and 0.4.

At Fermilab energies the nucleus is a spherical collection of smaller spheres (protons and neutrons) which shadow each other and hence give rise to a total cross section, σ, which goes like $\sigma \propto A^{2/3}$. Actually the measured dependence is proportional to $A^{0.69}$. At large p_T, collisions between constituents, the quarks, must dominate. Since quarks are point-like there is no shadowing and one would expect α --> 1.

An alternate way to describe the A dependence for Λ's is to use the transverse momentum and rapidity, y, instead of x_F and p_T. Rapidity is defined by

$$y = \frac{1}{2} \ln \left\{ \frac{E^* + p_l^*}{E^* - p_l^*} \right\} \qquad (6.8)$$

This implies that

$$dx \cong \frac{\sqrt{s}}{2} E \, dy \qquad (6.9)$$

Then the differential cross section can be expressed as

$$E \frac{d^3\sigma}{dp^3} = \frac{1}{\pi} \frac{d^2\sigma}{dy dp_T^2} \qquad (6.10)$$

where the factor of π comes from integrating over the

azimuth. Dividing by the appropriate absorption cross section one has the differential multiplicity,

$$E\,\frac{1}{\sigma}\,\frac{d^3\sigma}{dp^3} = \frac{d^2n}{\pi dy dp_T^2} \quad . \qquad (6.11)$$

Since the rapidity variable, y, in one refernce frame is related by an additive constant to y′ in another frame Lorentz boosted along the beam axis, the shape of Eqn.(6.11) is invariant under longitudinal transformations. The differential multiplicity is interpreted as being the number of Λ′s produced per interacting proton per differential element, $dydp_T^2$.

The differential multiplicity for the Λ′s at three values of p_T is shown in Fig. 6.18, using the nucleon-proton center of mass rapidity. The curves are the interpolations from the fits to the data, and the values for σ are from Reference 21. Note the ordering of the data, the heavy targets have higher multiplicities up to y= 2.2, where the curves cross each other. Since $\sigma \propto A^{0.69}$, this crossing is simply the point at which $\alpha(y,p_T) = 0.69$.

One can interpret the evolution of these curves, from beryllium to lead, as being the result of additional collisions inside heavier nuclei. An estimate for the mean number of collisions in a nucleus is

$$\bar{\nu} = A\sigma_N/\sigma_A \qquad (6.12)$$

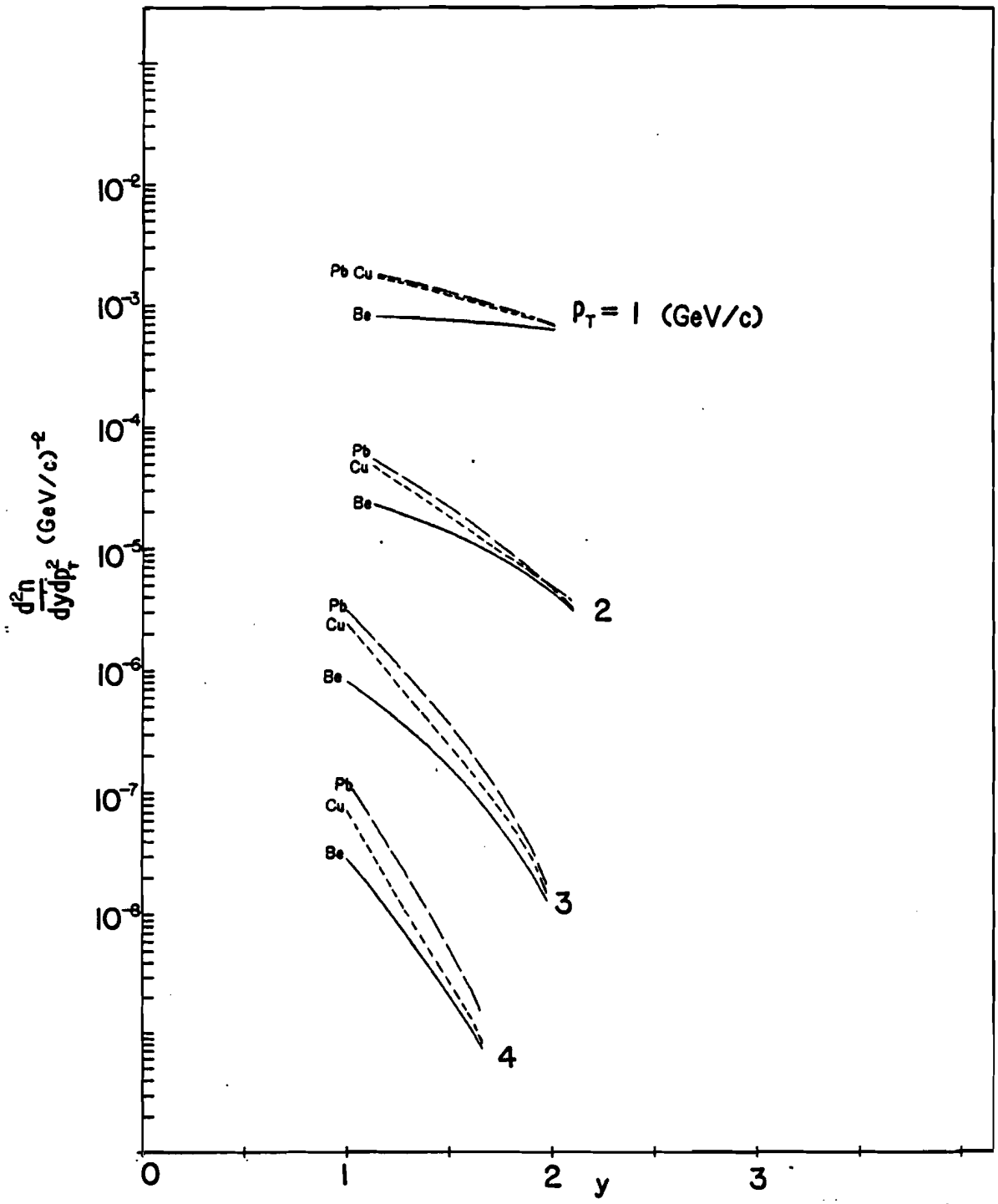

Figure 6.18 The differential multiplicity, Equation (6.12), is shown as a function of rapidity, y, for several values of p_T. Note that since $\alpha \gtrsim .69$ for the data shown here, the value of the differential multiplicity for lead is greater than beryllium, but for $\alpha \lesssim .69$ the opposite occurs (Ref. 22).

where σ_N, σ_A are the absorption cross sections for protons on a single nucleon and a nucleus of atomic weight A, respectively. Values of σ_N, and σ_A from Ref. 21 yield, $\bar{\nu}_{Be}$=1.4, $\bar{\nu}_{Cu}$=2.6, $\bar{\nu}_{Pb}$=3.6. Hence, one can imagine that one additional scattering (or absorption) from Be is, in some sense, equivalent to the production of Λ's from copper, and an aditional scattering from copper yields lead.

Another way of describing the A dependence is to write the cross section in powers of $A^{1/3}$ [22], the characteristic length ,

$$\frac{d^2\sigma}{dydp_T^2} = a(y,p_T)\ A^{2/3} + b(y,p_T)A + c(y,p_T)\ A^{4/3} \qquad (6.13)$$

The first term has the same behavior as the total cross section, the second term describes point-like collisions, and the last term is the rescattering correction term which can account for $\alpha(y,p_T) > 1$. Integrating over the appropriate range in y and dividing by σ , Eqn. (6.13) becomes

$$\frac{dn}{dp_T^2} = a'(p_T) + b'(p_T)\bar{\nu}_A + c'(p_T)\bar{\nu}_A^2 \qquad (6.14)$$

where it was assumed that $\sigma \propto A^{2/3}$ as an approximation. Now Eqn.(6.14) can be solved, since there is data from three targets at each p_T. The result of this exercise is shown

in Table 6.2. Notice that the relative contribution of c' is small except at large p_T, as expected.

p_T	a'	b'	c'
0.75 (GeV/c)	1.55×10^{-2}	2.17×10^{-2}	-3.53×10^{-3}
1.00	1.73×10^{-2}	8.71×10^{-3}	-1.37×10^{-3}
1.25	1.21×10^{-2}	4.65×10^{-3}	-6.83×10^{-4}
1.50	5.15×10^{-3}	2.71×10^{-3}	-3.56×10^{-4}
1.75	1.52×10^{-3}	1.67×10^{-3}	-2.06×10^{-4}
2.00	5.81×10^{-4}	3.86×10^{-4}	-3.30×10^{-5}
2.25	2.00×10^{-4}	1.05×10^{-4}	-3.24×10^{-8}
2.50	7.26×10^{-5}	3.05×10^{-5}	3.83×10^{-6}
2.75	2.99×10^{-5}	6.37×10^{-6}	3.56×10^{-6}
3.00	1.33×10^{-5}	-1.21×10^{-6}	2.38×10^{-6}
3.50	2.62×10^{-6}	-1.51×10^{-6}	5.97×10^{-7}
4.00	6.04×10^{-7}	-4.75×10^{-7}	1.49×10^{-7}

Table 6.2 The values of the parameters in Eqn (6.14) derived from the data. It is an alternative way of describing the the A dependence for the Λ.

6.5 Extrapolation to A = 1

Two formulations of the A dependence of the invariant cross section for Λ's have been given above, Eqns (6.7) and (6.14). It is a simple matter to set A=1 in the formulas and compare these extrapolations to data taken with a hydrogen target.

The extrapolation using the α parameter, Eqn (6.7) was computed by a least square fit for all three targets and is shown in Figs. 6.19-6.21 as a function of x_F for values of p_T from 1 to 3 GeV/c. The hydrogen data from Ref 4 is shown as a comparison. Figure 6.22 shows the extrapolation to A=1 using Eqn (6.14) as a function of p_T, again with data from Ref 4. A value of 33 mb [21] was used for the nucleon absorption cross section in the extrapolation of Eqn (6.14).

Both extrapolations predict values for the nucleon cross section that are too large and tend to diverge from the hydrogen data as p_T increases. This has also been observed in charged π and K production [19].

6.6 Indirect Λ Production

The are many modes for prompt Λ production besides the direct mechanism. Other sources of Λ's are the decays

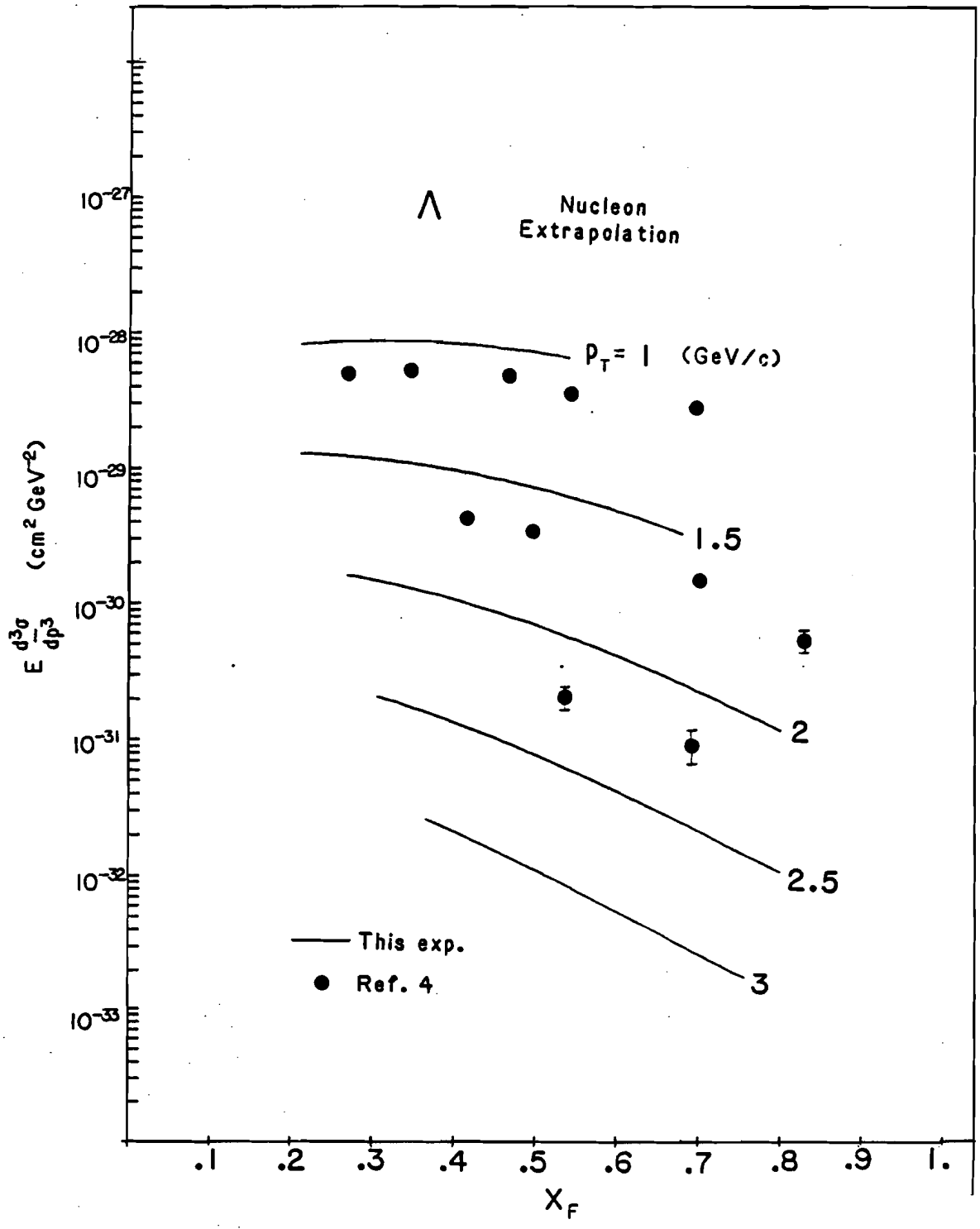

Figure 6.19 The extrapolated Λ nucleon cross sections using the power law, Equation (6.8), with A = 1. The extrapolations here are not compatible with the data from Ref. 4 .

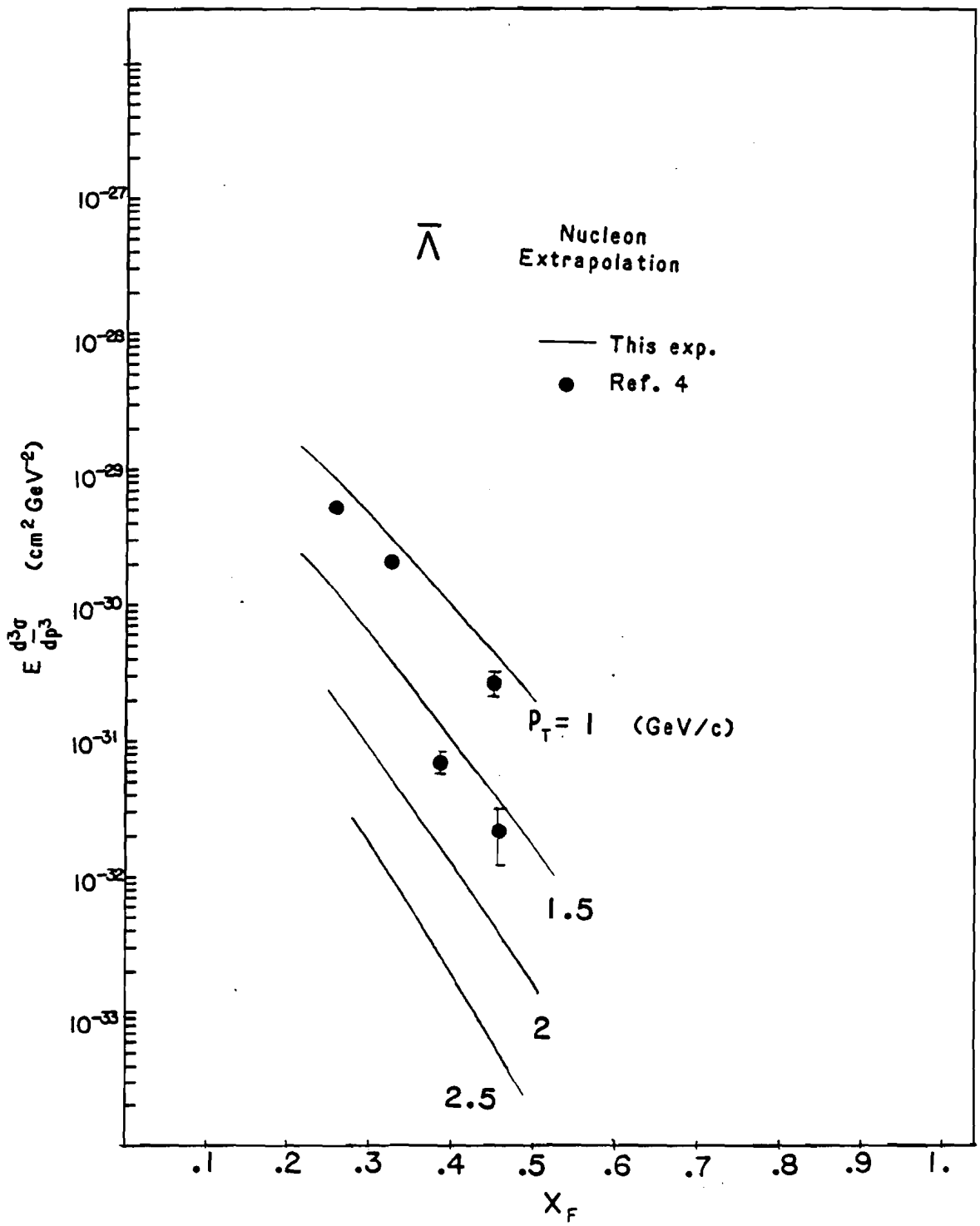

Figure 6.20 The extrapolated $\bar{\Lambda}$ nucleon cross sections using the power law Equation (6.8) with A = 1. Unlike the Λ's, the agreement between this experiment and Ref. 4 is good.

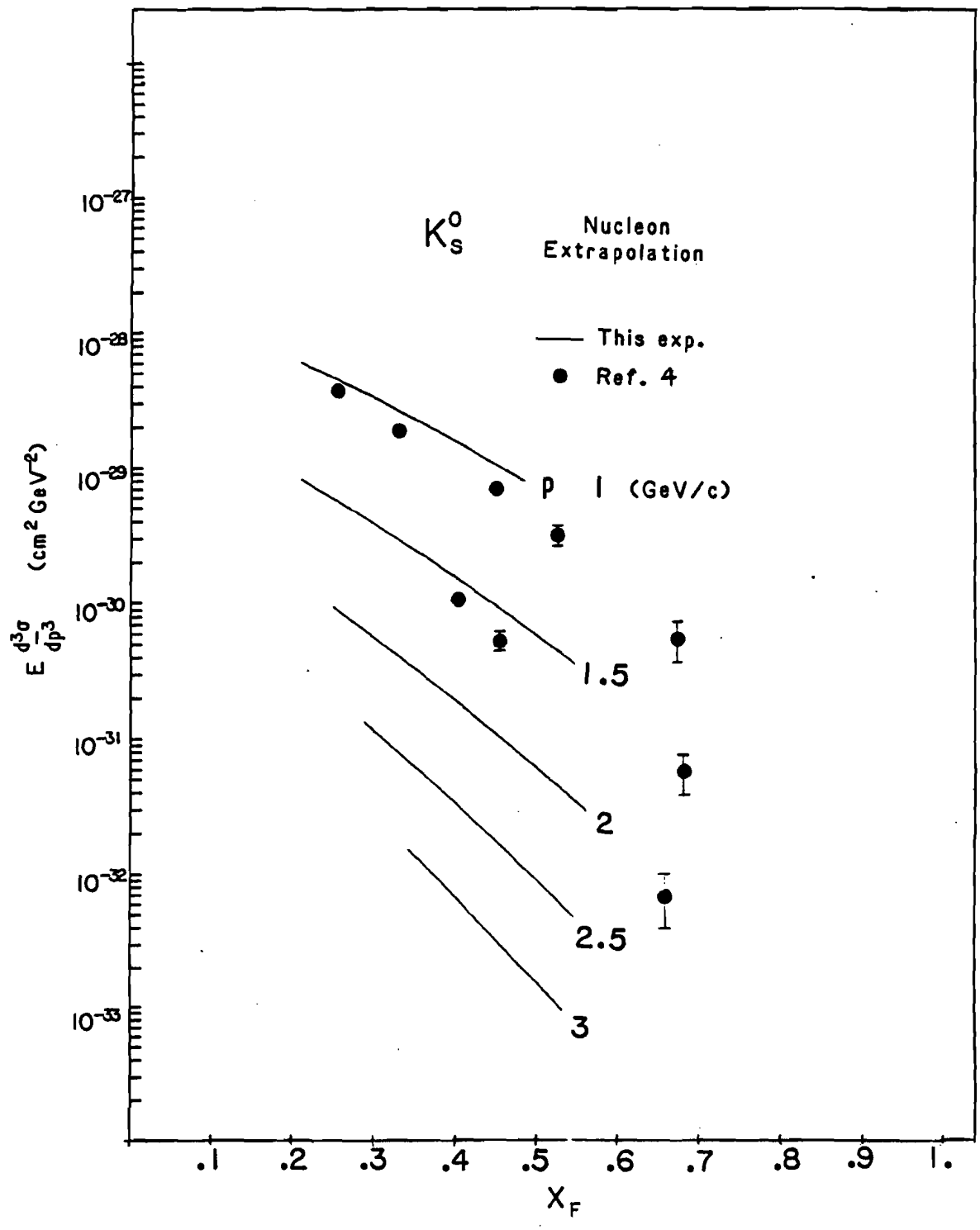

Figure 6.21 The extrapolated K_S^0 nucleon cross sections using the power law Equation (6.9) with A = 1. As with the Λ's, the comparison between the extrapolation and data from Ref. 4 is systematically bad.

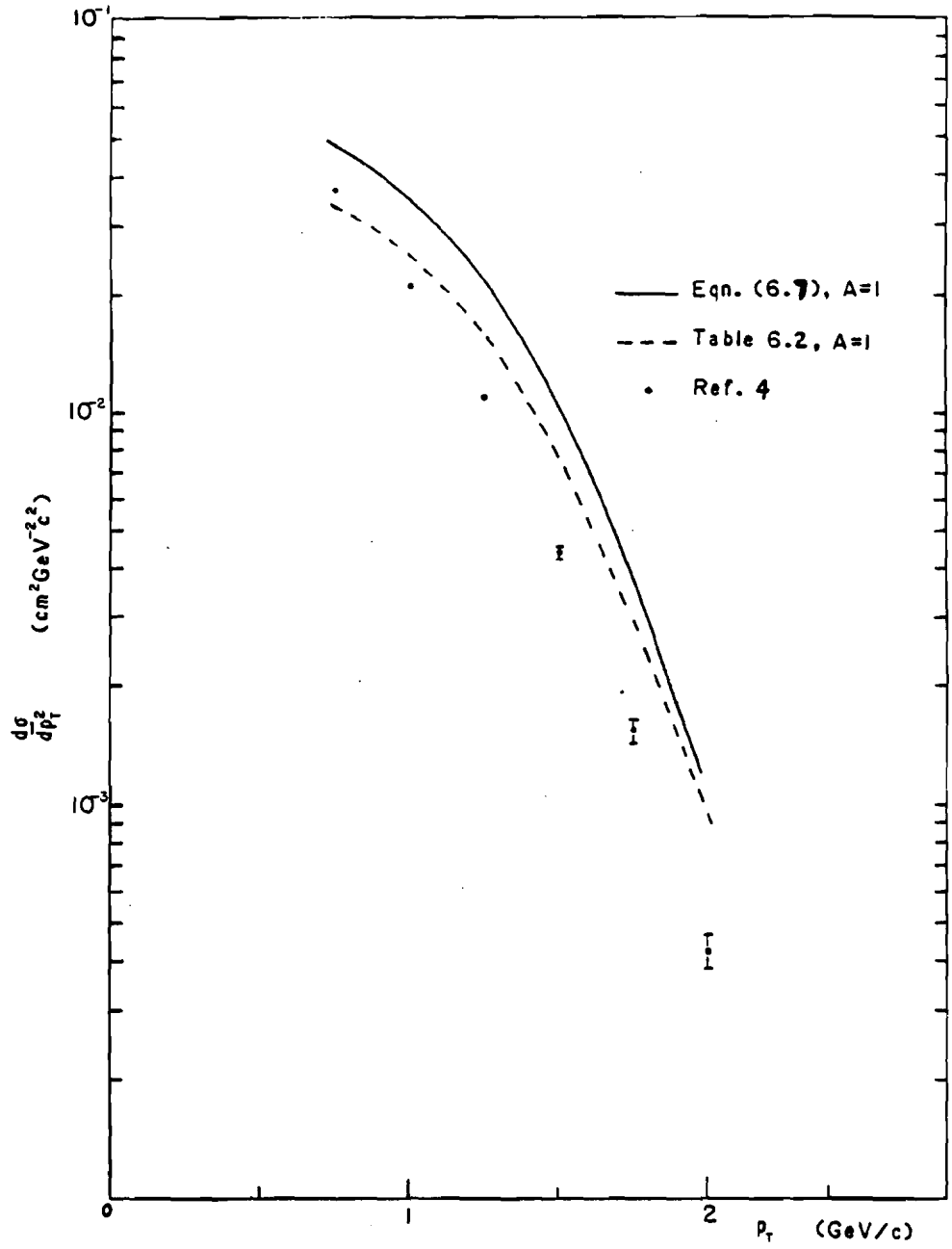

Figure 6.22 The extrapolation to A = 1 for Λ's using Equation (6.14) and Table 6.2 is shown together with the power law extrapolation, Equation (6.7) and data from Ref. 4 . The agreement between the data and fits becomes very poor as p_T increases from 1 to 2 GeV/c. A value of 33 mb was used in computing the extrapolation from Equation (6.14) (the broken curve).

of the Σ° and its excited states and other S=-1 excited states. The experiment could not distinguish between the different sources of the observed Λ. These same considerations must also apply to $\bar{\Lambda}$ production.

Unfortunately, the high energy production rates of these states have rarely been measured, if at all. Some information is available but it is not complete. For example, at 40 GeV, in neutron-proton interactions, the ratio of $1/2(\Sigma^{+}+\Sigma^{-})$ production to production is about 10% for most of the x_F range, with the ratio decreasing as $x_F \rightarrow 1$ [24]. Similar measurements exist for the (1520) state [25].

The theoretical calculations differ widely in their predictions, ranging from a direct contribution of 60% [26] to as low as 5% [27]. The calculations of the observed Λ cross sections show that the dominant particles are expected to be low mass states, the Λ, Σ°, and $\Sigma(1385)$. The Σ° always yields a Λ, and the $\Sigma(1385)$ yields a Λ 93% of the time (assuming all charged states are equally likely). Hence the inclusive "Λ" cross sections measured here are a collection of S=-1 states.

CHAPTER 7

Presentation and Discussion of Polarization Data

7.1 The Data

The values of the polarization, $\mathbb{P}$, obtained from the analysis of Chapter 5 are differentiated by the target used, nominal production angle, and momentum. In describing the behavior of $\mathbb{P}$ the variables p_T and x_F will be used as well as the laboratory based variables, θ_Λ, and p_Λ the momentum. The data from this experiment can be described very simply using either set, but for consistency the data is tabulated in terms of p_Λ and θ_Λ in Appendix G.

The Λ polarization as a function of x_F for all fixed incident proton angles is shown in Fig. 7.1. Only Λ's produced with the beryllium target are included. The

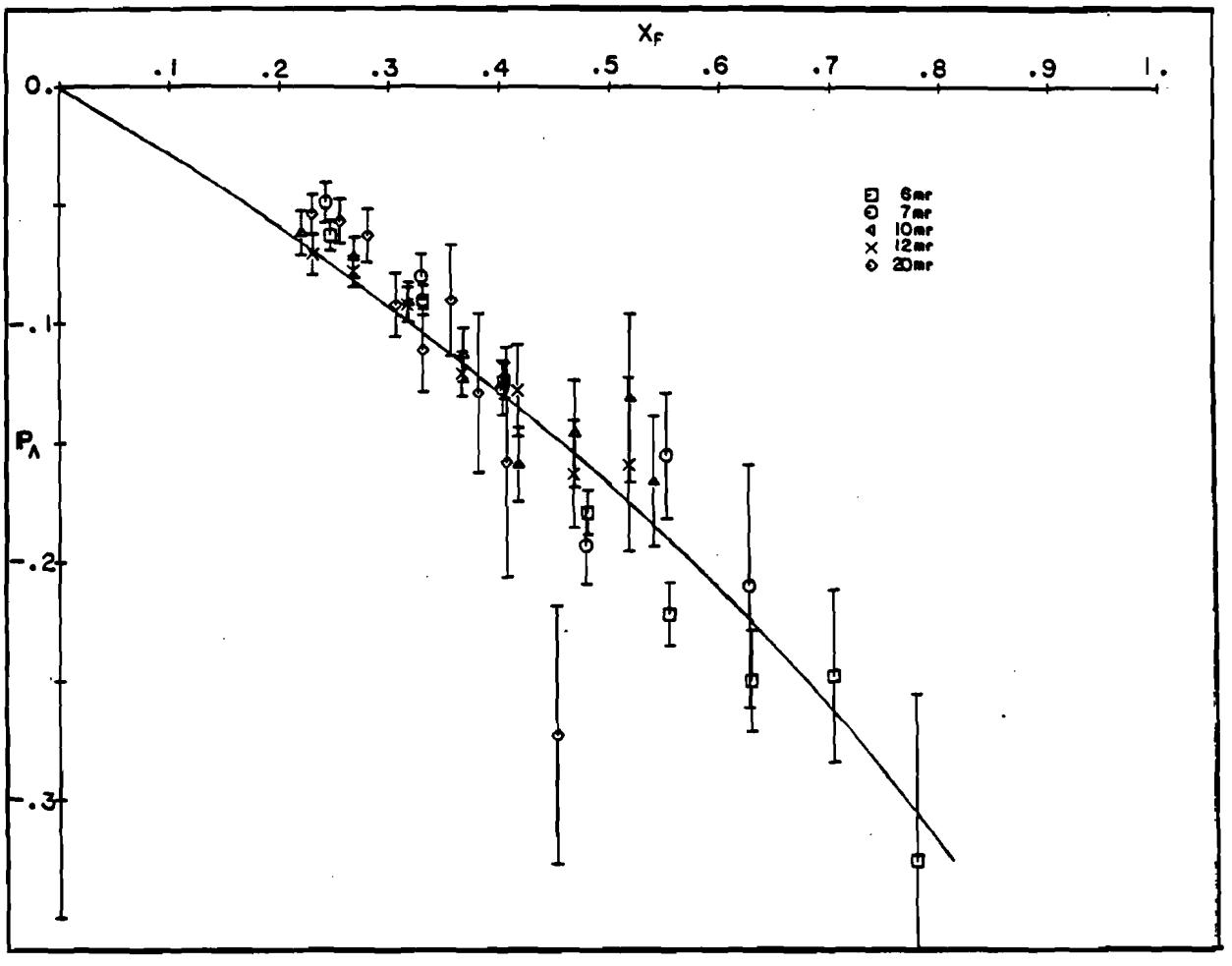

Figure 7.1 Λ Polarization from beryllium for all incident proton angles is shown as a function of x_F. The fact that P_Λ seems insensitive to θ_p implies that P_Λ is not dependent on p_T.

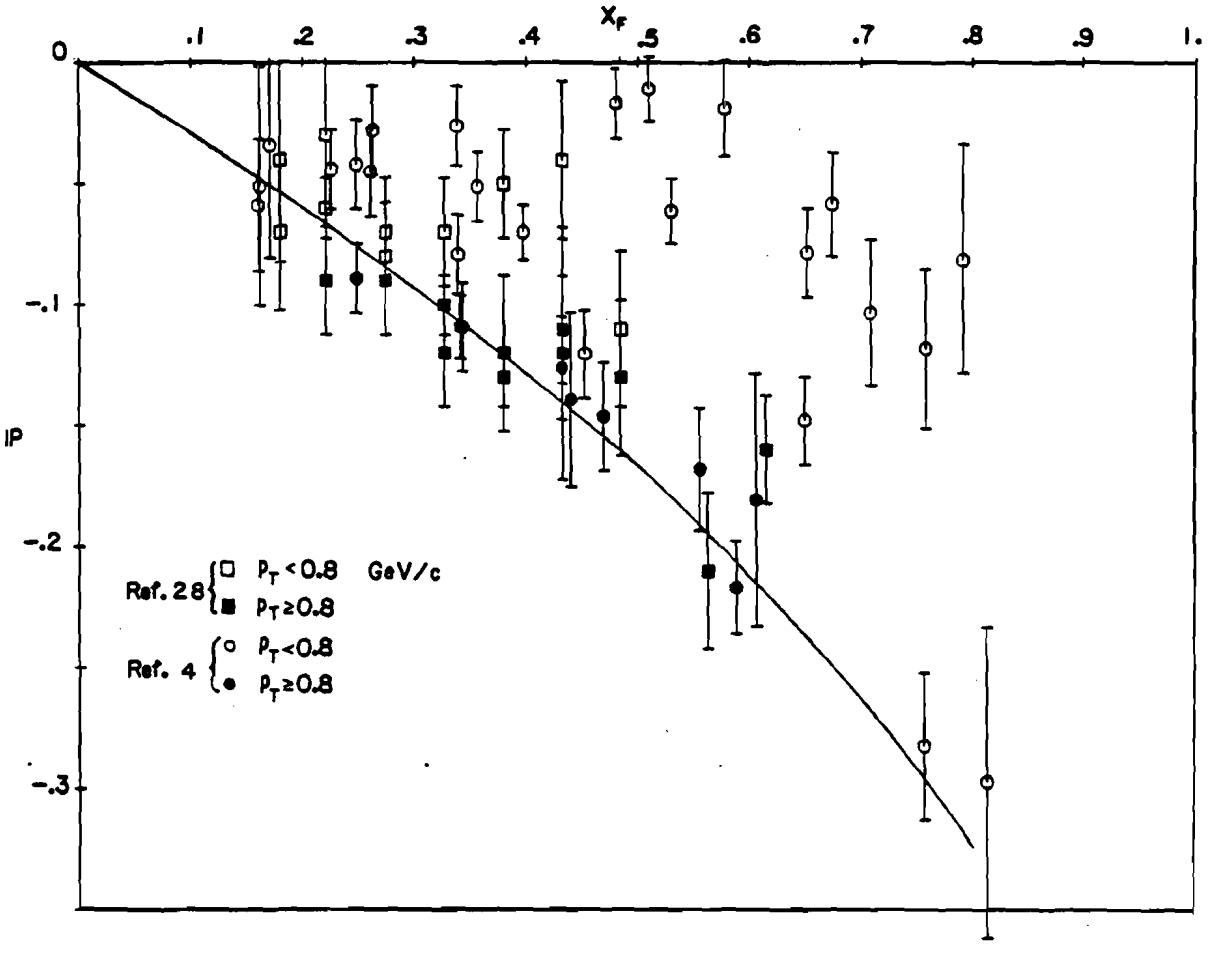

Figure 7.2 Polarization data from Refs. 4 and 28 are shown. The data are differentiated by p_T, not θ_p, to show that the larger p_T points are consistent with data from this experiment. The solid curve is the same as that in Fig. 7.1.

central feature in the figure is that the polarization is insensitive to Θ_p in the range of Θ_p available to this experiment. From this graph alone one can conclude that for the particular kinematic range explored by this experiment the polarization $\mathbb{P}$ is nearly a linear function of x_p. The sign of the polarization is negative relative to $\vec{p}_i \times \vec{p}_\Lambda$ at the target.

The dependence of $\mathbb{P}$ on p_T is implicit in Figure 7.1 since p_T is just the product of the Λ momentum and Θ_p. The implication is that $\mathbb{P}$ is independent of p_T to a good approximation. Data from Ref. 4 (H_2 target) and Ref. 28 show that this is not true at small p_T, $p_T \lesssim 1$ GeV/c. This is shown in Fig 7.2. Note that the data taken at the larger Θ_p, and hence large p_T, tend to follow the same behavior as the data in Fig 7.1. In the region of phase space where the sets of data overlap there is good agreement. Again, the fuctional fit Eqn (7.3) is superposed on the figure (the same function shown on Fig 7.1) as a benchmark between the data sets. The range in p_T in this experiment is 0.8 GeV/c to 3.7 GeV/c and that of Refs. 4 and 6 is 0.2 GeV/c to about 1.5 GeV/c.

One aspect of the behavior below 0.8 GeV/c is imposed by the physics of the process giving rise to the Λ. At a transverse momentum of zero, the production angle is also equal to zero and so the parity allowed direction in the reaction is not defined. Hence, as $p_T \rightarrow 0$, $\mathbb{P} \rightarrow 0$.

This behavior is clearly seen in the H_2 data for $p_T \lesssim 1$ GeV/c, but there is no substantial indication of this in the data from this experiment.

The inclusion of the hydrogen target data completes the qualitative picture of inclusive Λ polarization from small p_T to near 4 GeV/c. $\mathbb{P}$ becomes independent of p_T or "saturates" around $p_T \simeq 1$ GeV/c, and below this value $\mathbb{P}$ decreases as p_T becomes small. There is no evidence that $\mathbb{P}$ decreases at large values of transverse momentum.

7.2 Functional Fits to the Λ Polarization

A phenomenological fit to the polarization data can be done to quantify the features described qualitatively above, with a functional form consistent with the physics. In addition to the physical requirement that $\mathbb{P} = 0$ at $p_T = 0$, it was also required that $\mathbb{P} \leq 1$ at $x_F = 1$ and that $\mathbb{P} \rightarrow -\mathbb{P}$ for $x_F \rightarrow -x_F$. The last condition is a formal symmetry for proton-proton interactions. It is adopted here as an approximate symmetry and it implies that $\mathbb{P} = 0$ when $x_F = 0$, which the data seem to support.

The data from this experiment appears to be independent of p_T and was fit with a function of the form,

$$\mathbb{P} = c_1 x_F + c_2 x_F^3 . \qquad (7.1)$$

Standard chi-square minimization techniques yielded the values $c_1 = -0.239 \pm 0.008$, and $c_2 = -0.44 \pm 0.05$ with a chi-square per degree of freedom, χ^2/d.f., of 1.74. If c_2 is set to zero $c_1 = -0.301 \pm 0.004$ with χ^2/d.f.= 3.72.

The data from Refs. 4 and 28 was combined with this experiment's to give a larger sample covering the small p_T sector of $[x_F, p_T]$ space, and this total sample fit to an appropriate function. The target difference can no longer be ingnored in the polarization data since a target dependence of $\mathbb{P}$ has been observed in this experiment and elsewhere[28]. The polarization results for copper and lead targets are given in Section 7.5. The most unambiguous way to determine the ratio of the H_2 target polarization, $\mathbb{P}_H$, to the beryllium target polarization, $\mathbb{P}_{Be}$, is to introduce this ratio, r, as an additional unconstrained parameter to the function that is minimized. Symbolically,

$$\mathbb{P}_H = r\mathbb{P}_{Be}. \qquad (7.2)$$

The intersection of the kinematic regions occupied by both sets of data encompasses 11 of 42 data points in the H_2 data set, 12 of 23 points from Ref. 28 and 17 of 41 data points from this experiment. Since the union of the two data sets now covers the low p_T region, the fitting function must include an explicit dependence on p_T. An appropriate function is,

$$\mathbb{P} = (c_1 x_F + c_2 x_F^3)\ (1-\exp\{-c_3 p_T^2\}) \qquad (7.3)$$

The exponential term provides the function with the "saturation" behavior observed qualitatively.

The fit yielded the values for the coefficients; $c_1 = -0.295 \pm 0.010$, $c_2 = -0.18 \pm 0.04$, $c_3 = 2.48 \pm 0.12$, $r = 1.09 \pm 0.03$, with $\chi^2/\text{d.f.} = 1.8$.

Many other functional forms were tried instead of Eqn.(7.3), including a bilinear form and Eqn(7.3) with p_T^2 replaced by p_T, but all gave larger χ^2 values.

7.3 Systematic Error Estimation and Backgrounds.

Under the assumption that parity is conserved in the interaction, the x-component of the polarization, $\mathbb{P}_x$, must be zero. Therefore, measuring $\mathbb{P}_x$ gave an indication of the accuracy of the bias cancellation, and any non-zero value for $\mathbb{P}_x$ originated in the apparatus or analysis. It was found that $\mathbb{P}_x \leq 0.003 \pm 0.001$ for all production angles less than 20 mr. At 20 mr $\mathbb{P}_x = +0.009 \pm 0.002$. These results were independent of the Λ momentum to within statistical errors.

A second test for false polarization signals was performed on the data by measuring $\mathbb{P}$ for $K_S^0 \rightarrow \pi^+\pi^-$ at 6 and 20 mr. For 6 mr all three components were negligible, $\mathbb{P}_i \leq 0.006 \pm 0.010$, and for 20 mr $\mathbb{P}_{x,y} \leq 0.007 \pm 0.013$ and $\mathbb{P}_z = -0.011 \pm 0.014$. These results are not surprising,

Functional fit to the data (E555−E441)

$$\mathbb{P}_\Lambda = (-.29X - .19X^2)(1 - e^{-2.5p_T^2})$$

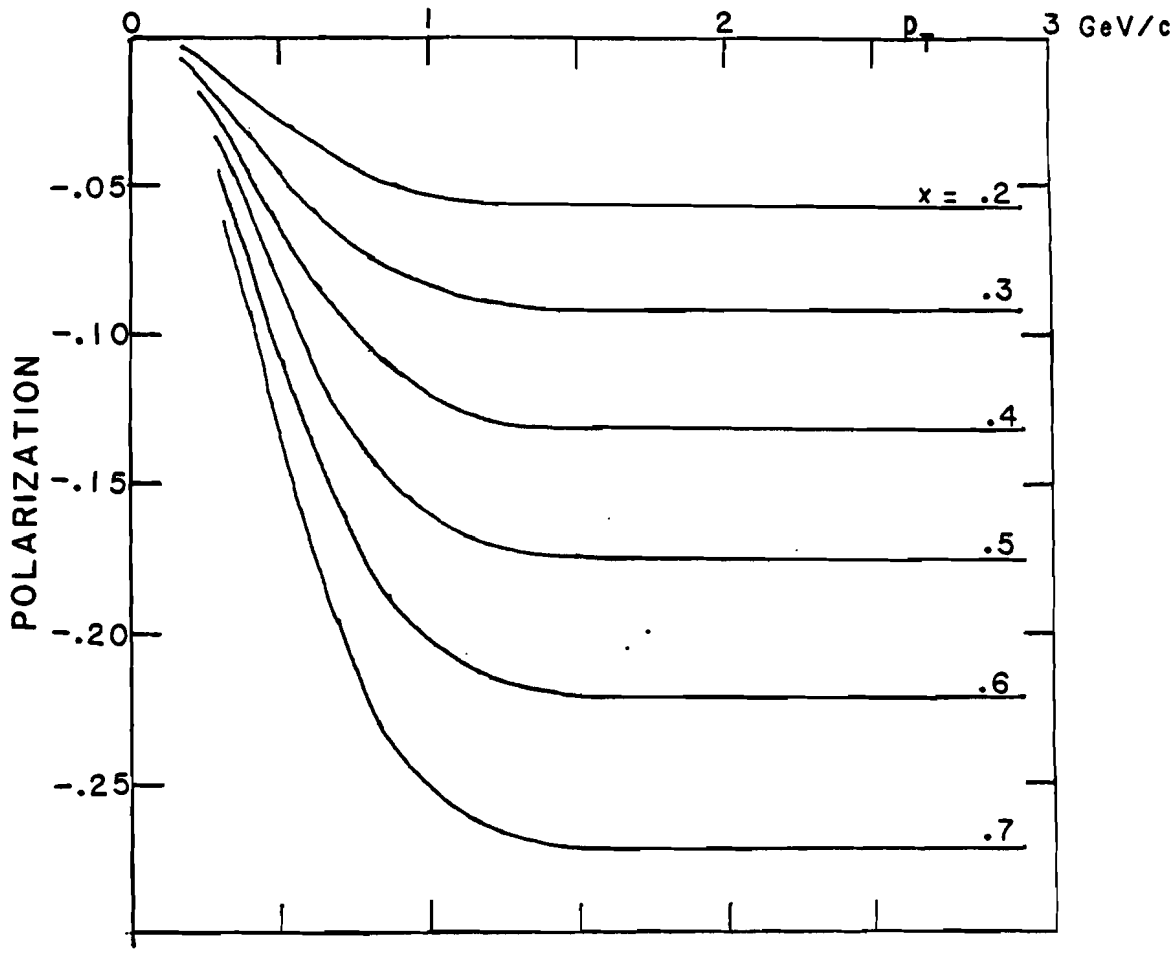

Figure 7.3 The behavior of Equation (7.3) with parameters fit to the data from this experiment and Ref. 6, as described in the text is shown as a function of p_T.

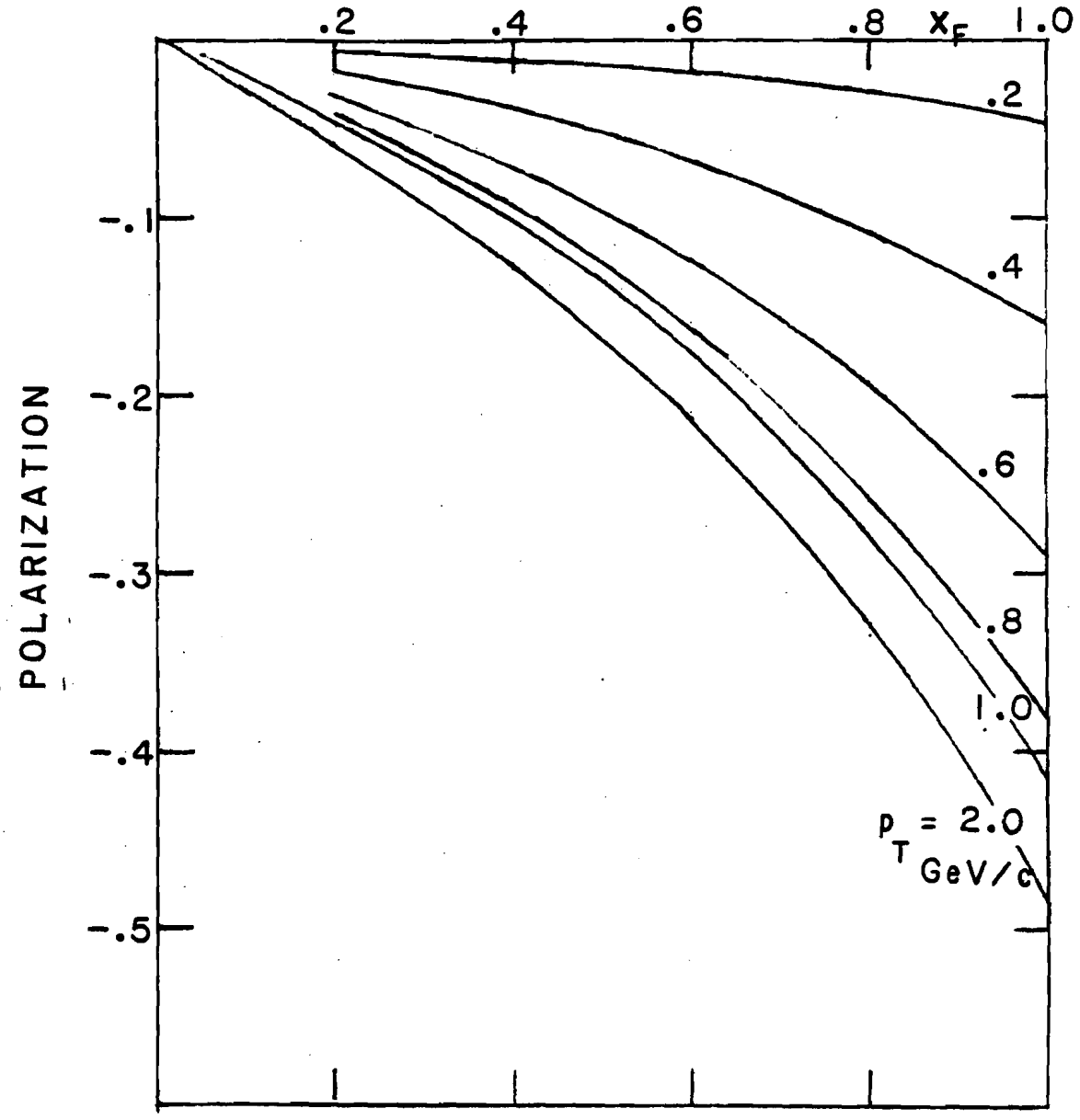

Figure 7.4 The same function of Figure (7.3) is now presented as a function of x_F.

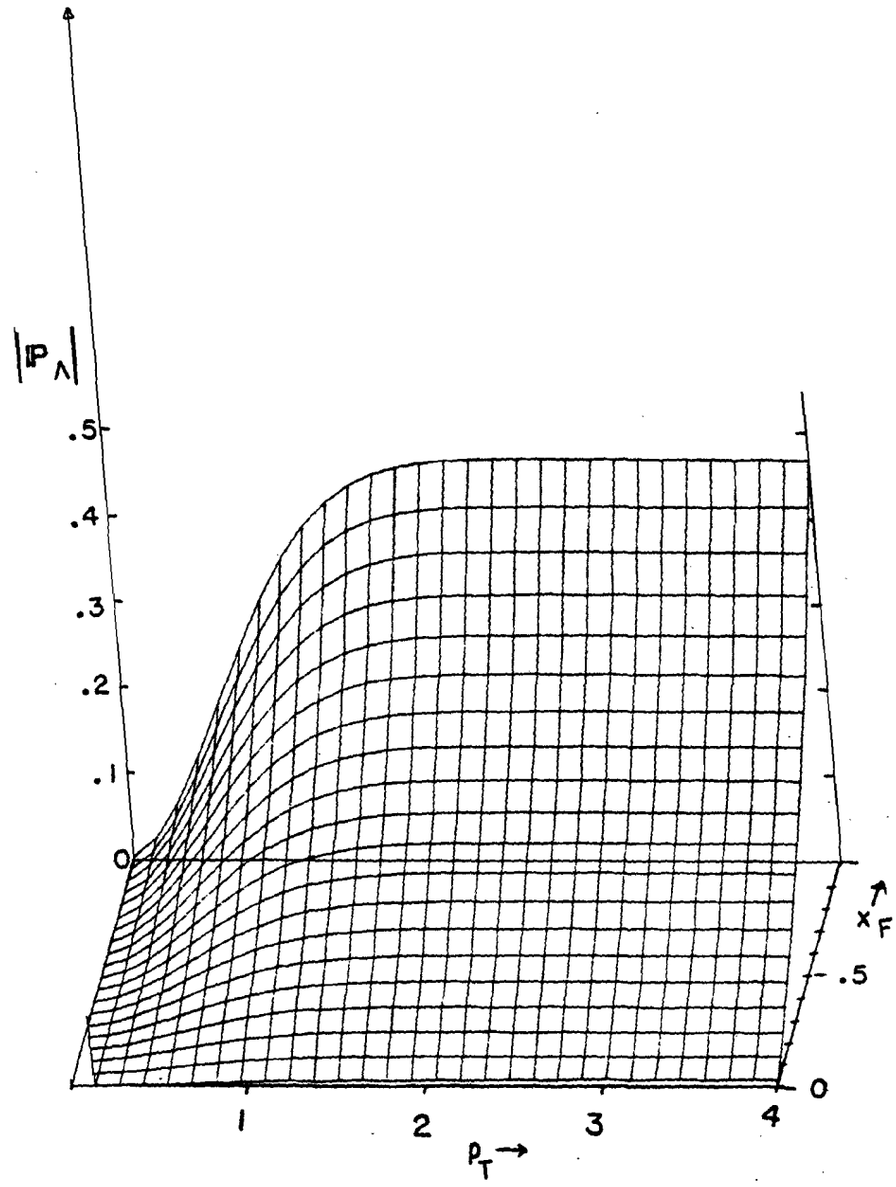

Figure 7.5 The magnitude of the function Equation (7.3) is shown as a function of both variables.

since the data taking conditions at the highest production angles were the least understood. One significant source of systematic uncertainties was due to the effects of localized chamber inefficiencies from the large flux of charged particles from decays and other neutrals converting upstream of the spectrometer magnet M2. These ineffiencies induce an acceptance loss in specific regions of cosO space, and since these losses are not simulated in the Hybrid Monte Carlo, a false signal may result. A systematic error of 0.003 is assigned components $\mathbb{P}_i$ for $\Theta_p <$ 20 mr, and a systematic error of 0.010 is assigned to the components $\mathbb{P}_i$ for Θ_p = 20 mr.

An unpolarized background contamination in the Λ sample like that due to K_S^0 decays will not have a measurable effect on $\mathbb{P}$, but it may affect $\mathbb{B}$. However, a known polarized source of background decays could potentially distort the true value of $\mathbb{P}$. The Ξ^0's are known to be both polarized and a measurable background in the sample, as mentioned before. The effect of Ξ^0's can be estimated from their known polarization behavior (which is approximately the same as the Λ's [28]) and the precession angles for the Λ's and Ξ^0s, ϕ_Λ , ϕ_Ξ. Given that $\phi_\Lambda = 140^\circ$ and $\phi_\Xi = 280^\circ$ measured from the y-coordinate axis it is straightfoward to calculate that the Ξ^0 background increases the measured $\mathbb{P}_z$ by 0.3% and decreases $\mathbb{P}_y$ by about 1% at a momentum of 90 GeV/c, and these estimates are

reduced by a factor of two at 130 GeV/c. There are no other known sources of polarized non-Λ events.

The biases $\mathbb{B}_i$ are illustrated in Figs 7.6-8 for all angles as a function of momentum. Confidence in the passive (cancelling) nature of the $\mathbb{B}_i$'s is supported by these facts:

-The $\mathbb{B}_i$'s do not depend on θ_p.

-The polarization results from this experiment are consistent with previous results even though the apparatus was different.

-The values of χ^2 from Eqn.(5.17) are not large (the $\mathbb{B}_i$ are fitted parameters).

Event reconstruction inefficiencies cannot be properly simulated by the HMC method of analysis as used in this experiment. These losses do indeed cause problems, but they are restricted to the lowest momentum Λ's. The main symptom is a large negative value for $\mathbb{B}_z$ which decrases rapidly with decreasing momentum and ranges from about -0.02 at 95 GeV/c to about -0.50 at 50 GeV/c. Because the ratio of $\mathbb{P}$ to $\mathbb{B}$ is akin to a signal to noise ratio no Λ polarization results are used below 85 GeV/c.

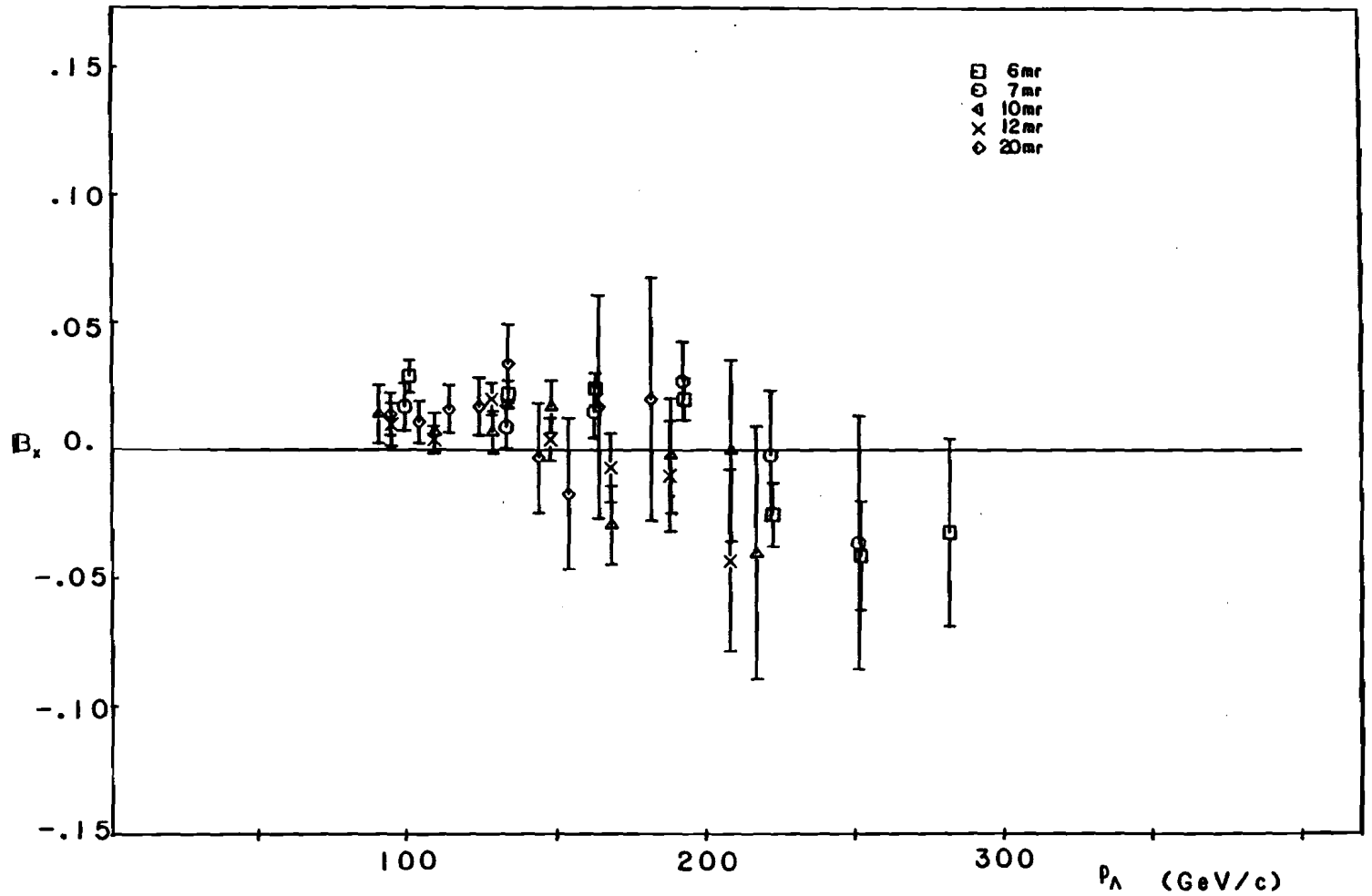

Figure 7.6 The measured bias, B_x, as a function of momentum. It is independent of θ_p.

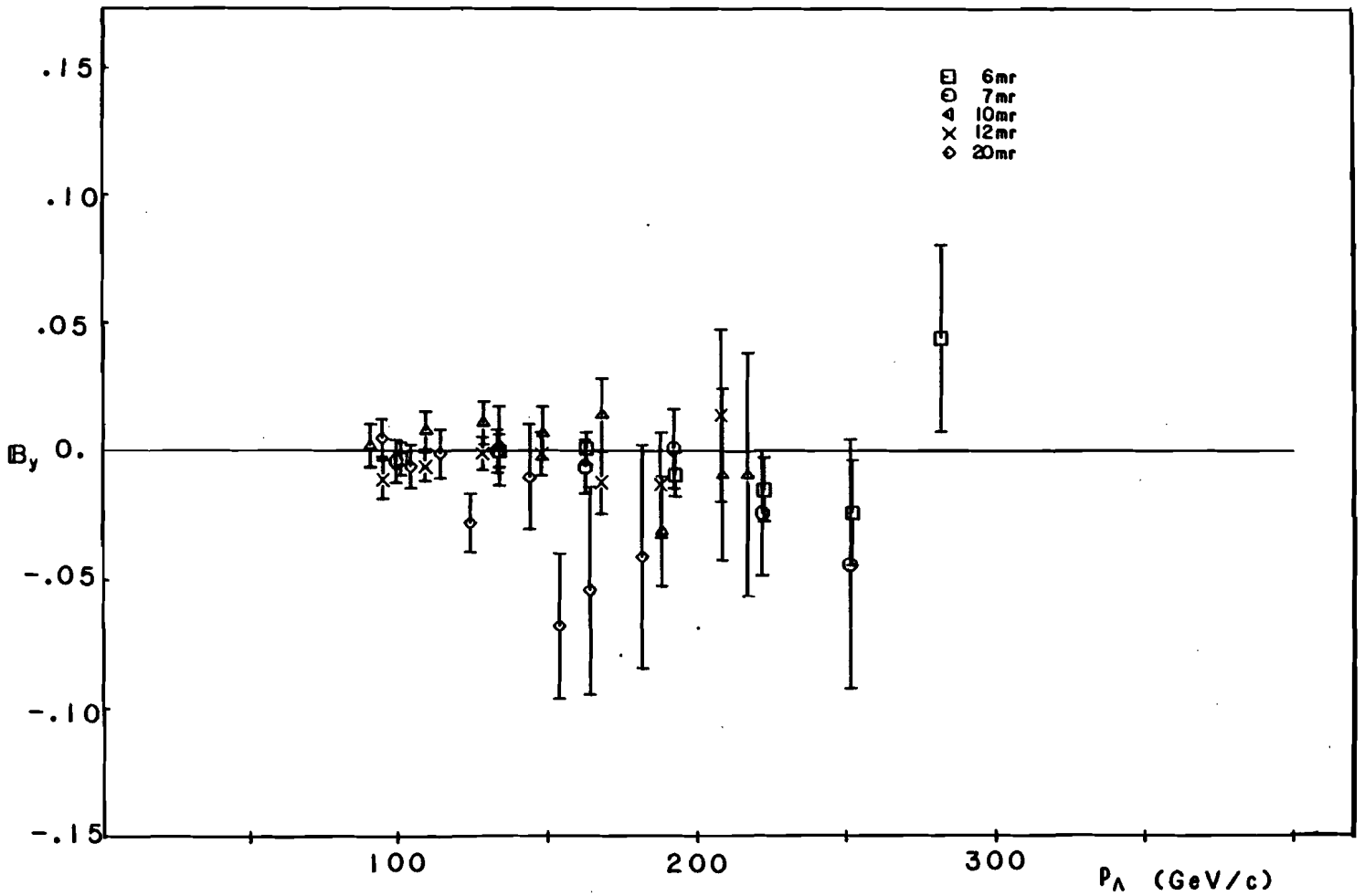

Figure 7.7 The measured bias, B_y, as a function of momentum.

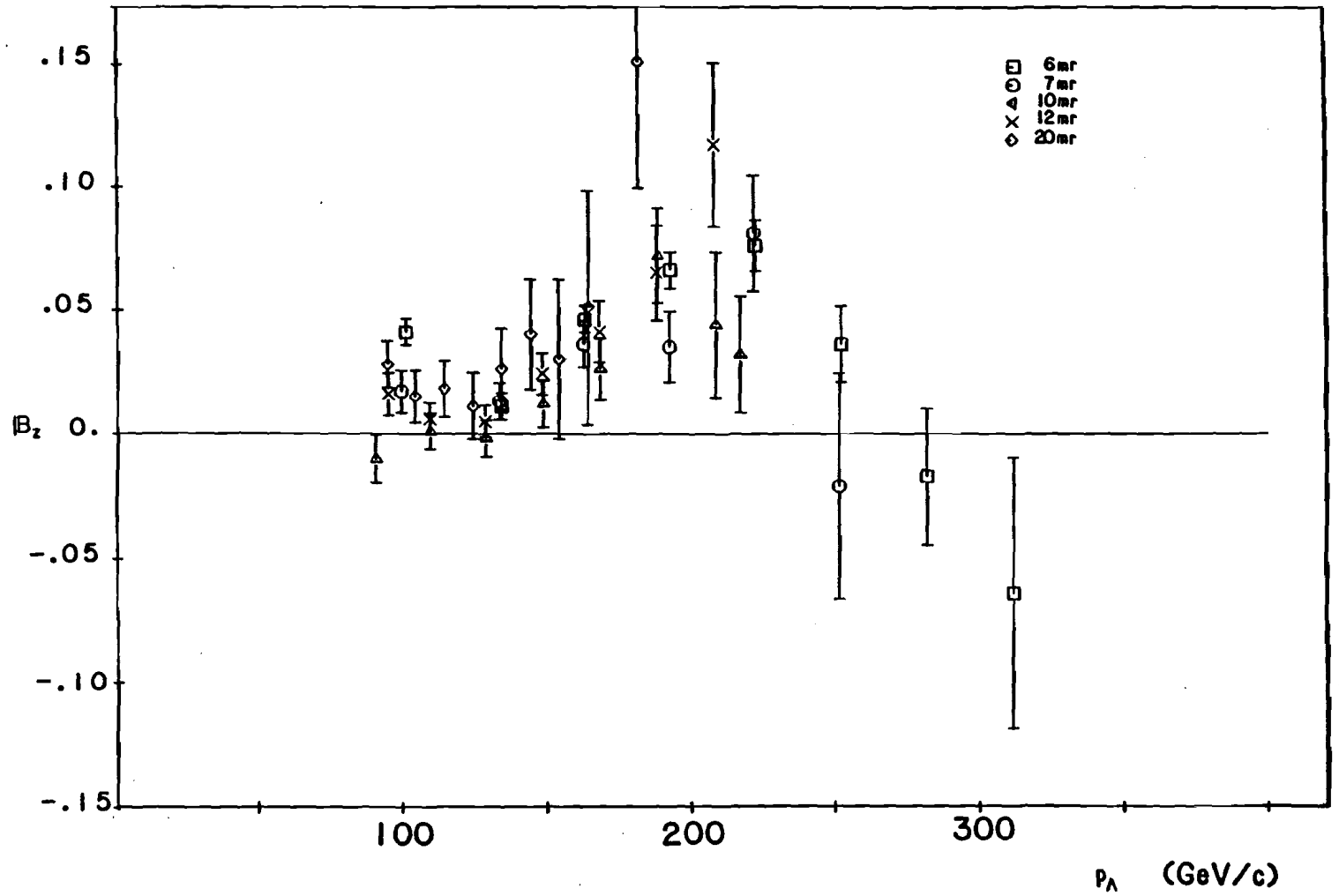

Figure 7.8 The measured bias, B_z, as a function of momentum.

7.4 $\bar{\Lambda}$ Polarization Search

The analysis machinery for the Λ's was also applied to the $\bar{\Lambda}$ events to search for a measurable polarization signal. Previous measurements showed a null result to a precision of 0.02 in $\mathbb{P}_{\bar{\Lambda}}$ up to a transverse momentum of 0.95 GeV/c [29].

The production angles 10, 12, and 20 mr were analyzed for polarization with a total sample of 788,327 events. The results are tabulated in Appendix G and are shown graphically Figure 7.9 . The range in p_T covered by the data is from 0.6 to 2.4 GeV/c. The global average (over momentum and production angle) of the polarization is $\mathbb{P}_{\bar{\Lambda}}$ =+0.006±0.005 (statistical error only) at p_T= 1.2 GeV/c and x_F=0.16. For comparison, the Λ polarization extrapolated to the same p_T and x_F using Eqn.(7.1) is calculated to be $\mathbb{P}$ (p_T=1.2,x_F=0.16)=-0.026±0.002.

7.5 A Dependence

The polarization analysis was segregated by targets. All results from this experiment given in earlier sections of this Chapter are from the beryllium (Be) target data. The polarizations from copper and lead targets, $\mathbb{P}_{Cu}$ and $\mathbb{P}_{Pb}$, are shown in Figs 7.10. The data were taken at production

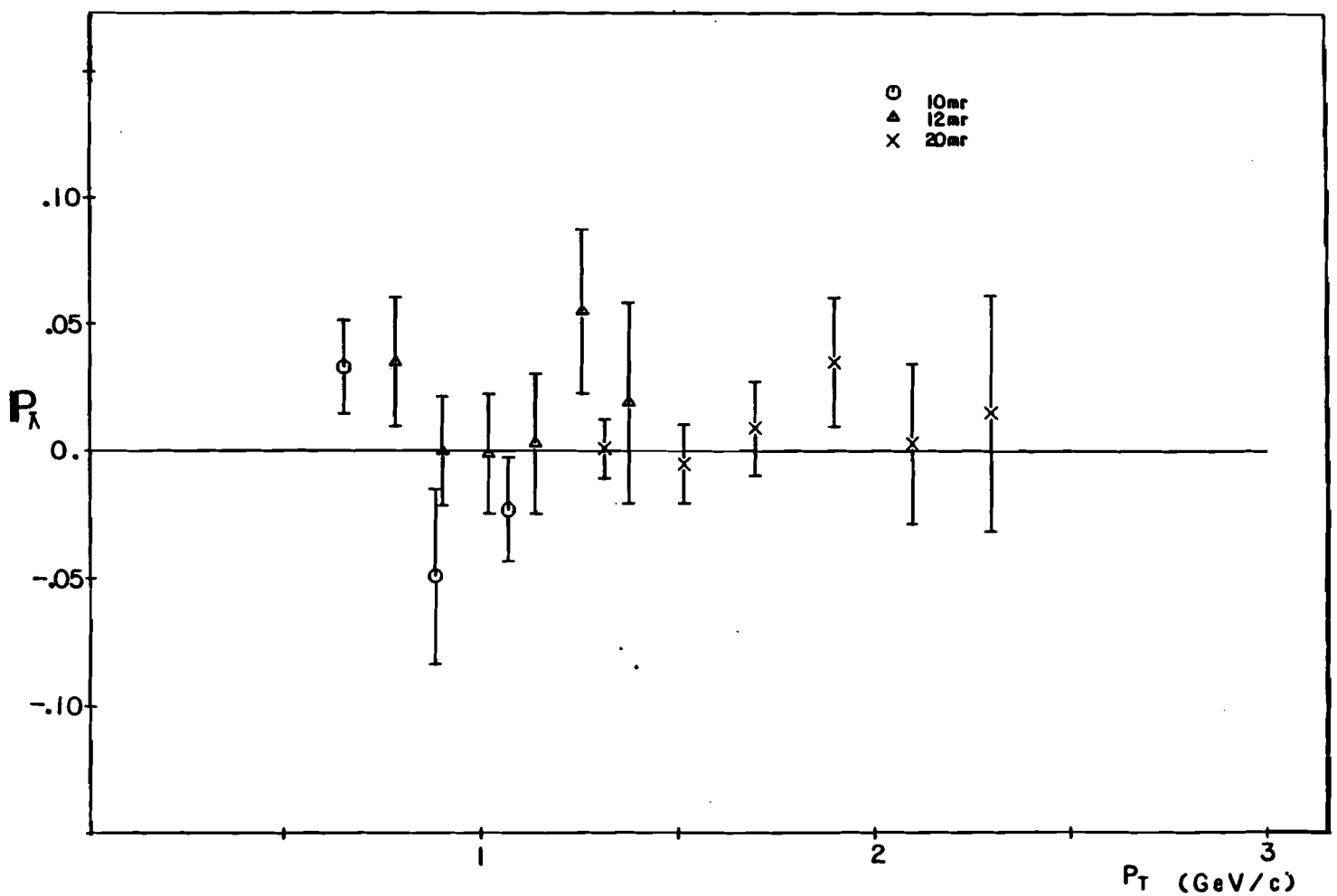

Figure 7.9 The polarization results for the $\bar{\Lambda}$ samples are shown at 10, 12 and 20 mr using Equation 5. and $\mu_{\bar{\Lambda}}$ = + 0.614. The polarization is consistent with zero to a transverse momentum of 2.3 GeV/c.

angles (Θ_p) of 7, 10 , 12, and 20mr. The data have the same qualitative behavior as the Be data, although the statistical errors are much larger. To make a meaningful comparison of the Cu or Pb data to the Be data, $\mathbb{P}_{Be,Cu,Pb}$ was momentum averaged for each Θ_p. Figure 7.11 shows the data from all three targets as a function of p_T. The cuts on the data are the same for all targets at each production angle. Nevertheless, the observed momentum spectra at the same angle will depend on the target, and hence the polarization will not be expected to be the same due to the x_F dependence of $\mathbb{P}$. The difference between the means of the momentum spectra of the lead target to the beryllium data was measured to be 5%. This effect has not been removed from the data samples. This implies that the expected difference in the polarizations will also be approximately 5%, which is small compared to the errors in $\mathbb{P}$.

The A dependence of the polarization is a statistically significant effect. The ratios of $\mathbb{P}_{Cu}$ and $\mathbb{P}_{Pb}$ to $\mathbb{P}_{Be}$ are shown in Fig. 7.12a with the mean of the ratios indicated. In Fig 7.12b the lead and copper data are combined and divided by $\mathbb{P}_{Be}$. There is no evidence that the ratio varies with p_T at the present level of statistical accuracy. A power law assumption fits the three available points well, but when extrapolated to A=1 yields $\mathbb{P}_H/\mathbb{P}_{Be} \simeq$ 1.36, a much larger effect than that actually computed from

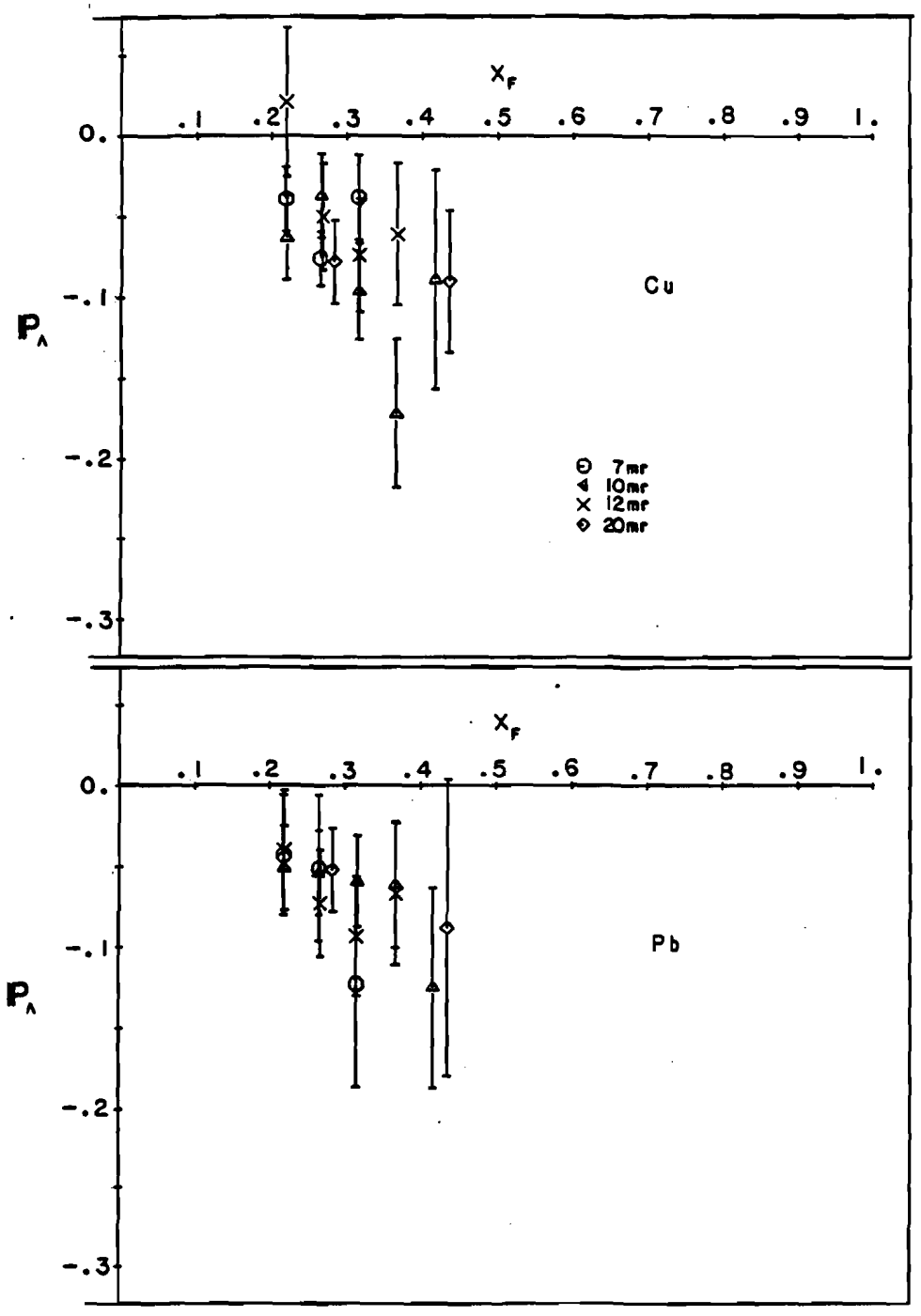

Figure 7.10 (a-b) Shown is the polarization measured for the copper and lead targets for all θ_P. The errors are large but the qualitative behavior is still evident and similar to that for the beryllium target (Figure 7.1).

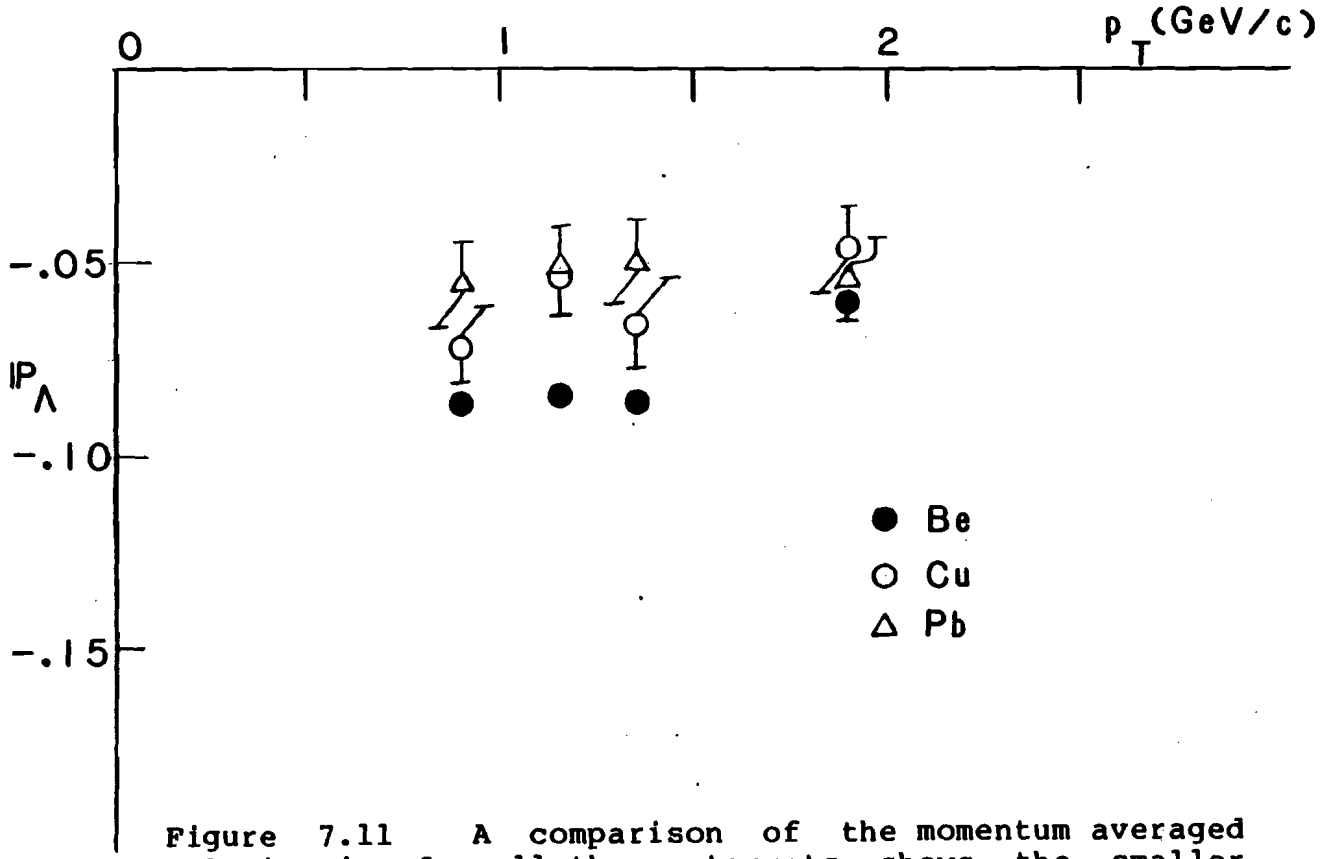

Figure 7.11 A comparison of the momentum averaged polarization for all three targets shows the smaller polarization magnitudes for the heavy targets. The points are from 7, 10, 12 and 20 mr data (left to right).

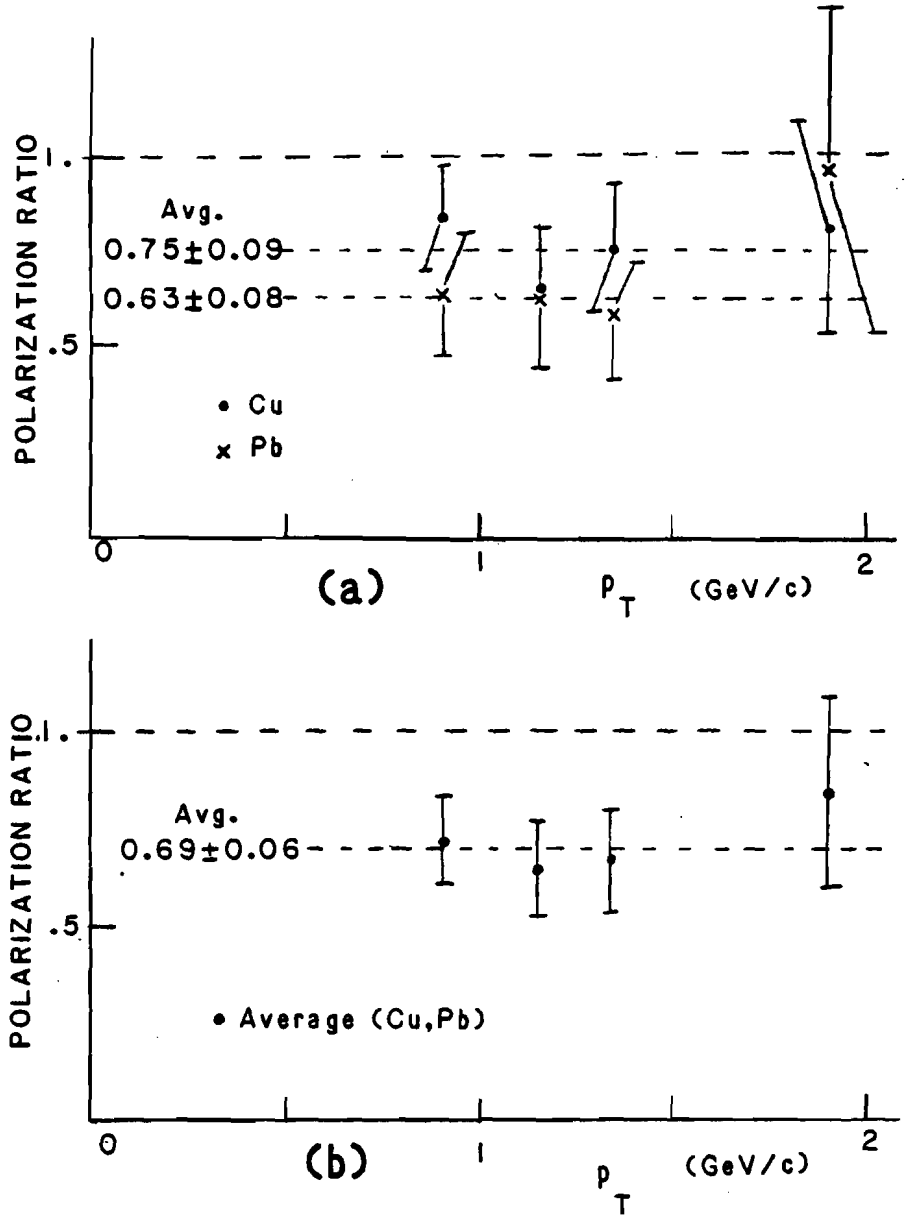

Figure 7.12 (a-b) The ratio of the momentum averaged copper and lead polarization to the polarization from beryllium is shown. In (a) the copper and lead are separate but in (b) the copper and lead data are combined to show the effect with improved statistical power.

the fits in Section 7.2.

7.6 Helicity Search

Helicity, h, is defined as the projection of the spin vector of a particle, $\vec{s}$, onto its momentum vector, $\vec{p}$,

$$h = \vec{s} \cdot \vec{p}$$

If the average helicity, $\langle h \rangle = \mathbb{H}$ of a sample of Λ events is not zero then there exists a component of polarization along the direction of the neutral beam, before entering the magnet M1. One would measure a non-zero value for $\mathbb{P}$ at the target. Since this is a violation of parity in the interactions giving rise to the Λ's, a measurement of $\mathbb{H}$ is a test of parity violation in hadronic collisions at large $\sqrt{s}$.

To determine $\mathbb{H}$ from the data, the effects of the precession of $\mathbb{P}$ must be removed as in the χ^2 function for $\mathbb{P}$, Eqn(5.15). The computation of $\mathbb{H}$ is easily incorporated in such a function by adding a term fitting a component orthogonal to $\mathbb{P}$ at the target,

$$\chi^2 = \sum_{ijk} \frac{\{\mathbb{A}_{y_{ijk}} - (\mathbb{B}_{y_i} \pm \mathbb{P}_i \cos\phi_k + \mathbb{H}_i \sin\phi_k)\}^2}{\sigma_y^2} + \frac{\{\mathbb{A}_{z_{ijk}} - (\mathbb{B}_{z_i} \pm \mathbb{P}_i \sin\phi_k + \mathbb{H}_i \sin\phi_k)\}^2}{\sigma_z^2} \tag{7.4}$$

The momentum and angle averaged result is $\mathbb{H}$ = +0.0033±0.0042 for p_T=1.1 GeV/c. There is no significant diffference between the $\mathbb{P}$'s determined in Eqn.(7.4) and the $\mathbb{P}$'s determined from Eqn.(5.15). Unfortunately the systematic errors dominate the ucertainty in $\mathbb{H}$ and limit the sensitivity to 0.003 for θ_p equal to 6, 7, 10, 12mr, and to ±0.009 for θ_p equal to 20mr. The measure of parity violation can also be expressed as the ratio of $\mathbb{H}$ to $\mathbb{P}$ from the same sample. The momentum and angle averaged value is $\mathbb{H}/\mathbb{P}$ =+0.049±0.094. Previous measurements using polarization data also at $\sqrt{s}$=27 GeV but at p_T=0.8 GeV/c again yielded a null result of $\mathbb{H}/\mathbb{P}$ =-0.024±0.023 [30].

7.7 The Effect of Non-direct Λ's

The value measured for $\mathbb{P}$ is certainly affected by the relative abundance of Λ's in the sample which result from the decays of Σ^0, Σ^{0*}, or other higher mass S= -1 states. To understand the effect of this contamination , consider the case where the observed neutral beam is actually a fraction β of direct Λ's, and a fraction $1-\beta$ of Σ's. From angular momentum and parity conservation arguments it is known that the polarization of the Σ transmitted to the daughter Λ is $-\frac{1}{3}\mathbb{P}$ (for uniform acceptance over θ and ϕ). Thus the Λ polarization measured in the spectrometer is given by,

$$\mathbb{P}_\Lambda^{meas} = \beta \mathbb{P}_\Lambda - \frac{1}{3}\mathbb{P}_\Sigma + \frac{\beta}{3}\mathbb{P}_\Sigma \qquad (7.5)$$

A reasonable asumption one can make about the polarization (it has not yet been measured) is that it is approximately equal to the measured values for Σ^+ and Σ^- polarization , $\mathbb{P}_{\Sigma^+} \simeq \mathbb{P}_{\Sigma^-} \simeq -\mathbb{P}_\Lambda$ [31,32]. Hence, the above estimate for the measured polarization becomes,

$$\mathbb{P}_\Lambda^{meas} \simeq \frac{2\beta+1}{3}\,\mathbb{P}_\Lambda \qquad (7.6)$$

This implies that the direct Λ polarization is diluted, with the dilution factor depending on the relative production cross sections, and on x_F since the daughter Λ's will have a softer momentum spectrum than the Σ's.

7.8 Discussion of the Results

The inclusive polarization phenomenon has been observed for all S= -1 or -2 baryons for which there is data. It has not been seen at the same level for inclusively produced protons [33]. This immediately suggests that in the quark model, the strange, or heavy quark, plays a fundamental role in the spin alignment of the final state. The Λ has a particularly simple quark-spin wavefunction in the direct product group SU(6).

In the SU(6) respecting wavefunction the s quark carries all of the spin information in the ground state Λ since the u and d quarks form a J=0 (singlet) state. Most

models of Λ polarization appeal to this simplification which seems justified to a large extent since the magnetic moments are known to be within about 20% of their expected SU(6) values.

Assuming SU(6) symmetry, the Λ's will be polarized if the s quark is produced in a polarized state, and so one must either propose a mechanism for producing polarized s-s pairs, or assert that P is due to some kind of interaction in the final state which then decays to a Λ.

A model for inclusive polarization by Heller [35] assumes the s quark is produced polarized (by gluon bremmstrahlung) and uses SU(6) symmetric wave functions for the initial and final states. It predicts the correct sign of $\mathbb{P}$ for hyperons (relative to the Λ) with one s quark in the final state. De Grand and Miettinen have introduced a model for polarization asymmetry [34] based on manipulation of hyperon SU(6) wave functions with a few simple (but ad hoc) rules. It assumes that the initial and final states can be separated into a quark + diquark state. The model correctly reproduces the sign of the polarization for all observed hyperons relative to the Λ. The same authors also propose a dynamical model to explain the origin of the spin alignment of the quarks. They propose that the alignment is caused by a Thomas precession of the spin of the recombining parton. This relativistic spin-orbit force occurs because the force between the fast proton fragment

and the slow quark(s) created in the reaction is not, in general, parallel to the initial momentum of the slow quark(s). Using simple assumptions about the distribution of the momentum fraction carried by the quarks and the form of the amplitude the authors arrive at a functional form for the behavior of Λ polarization as a function of p_T and x_F. This function is plotted in Fig. 7.13 as well as the empirical fit to the data, Eqn.(7.3). The model is consistent in the gross features such as the p_T dependence, but does not have as strong of a x_F dependence as the data.

A paper by Andersson, Gustafson and Ingleman [36] appeals to a semiclassical argument to produce a polarized Λ. In this model the authors assume that the $s\bar{s}$ quark pair created in the color field of the spinless ud diquark obtains angular momentum perpendicular to the production plane which is compensated by the alignment of the s (and $\bar{s}$) quark spin. The sign of $\mathbb{P}$ is due simply to a trigger selection effect: the p_T of the created s quark will preferentially lie in the same hemisphere as the p_T of the observed Λ.

Other models for Λ polarization use quark-gluon scattering to align the s quark [37] or the inteference of Σ^0 and Σ^{0*} amplitudes [38]. Triple-Regge models have also been applied to the problem [39,40] but non zero results are not possible without making the approach cumbersome.

Craigie has attempted [41] to reconcile Λ

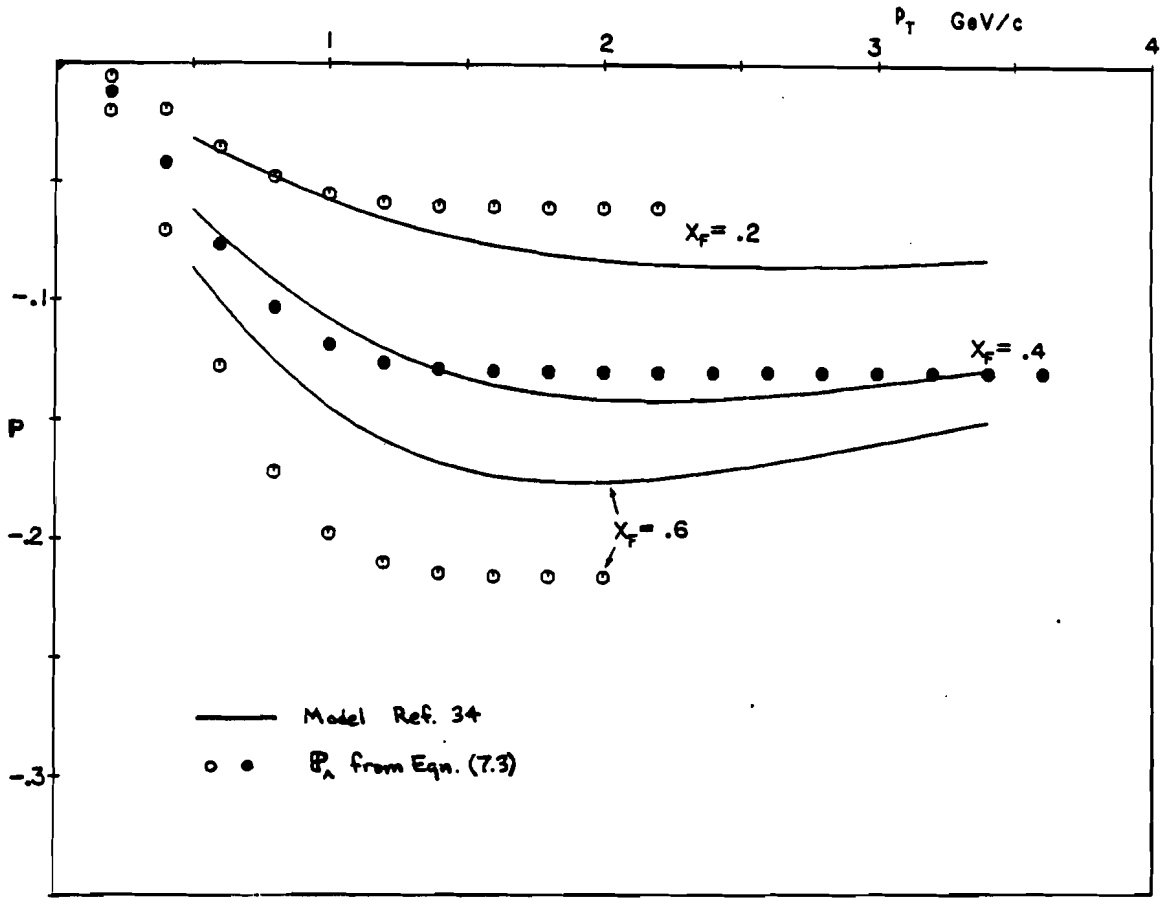

Figure 7.13 A comparison of the Λ polarization data, as represented by Eqn.(7.3), and the model of Ref. 34 is shown . The parameters of the model used in this figure are the same as those given in the reference.

polarization with perturbative QCD theory but it is hard to account for large polarizations from fundamental theory. There is one prediction of QCD applied to spin asymmetries which seems firm. The theory, like QED, predicts that at "large" p_T the polarization must vanish, or at least be very small [42]. This is equivalent to the limit of massless quarks so that helicity is conserved in the interactions of quarks and gluons. Hence transverse asymmetries must vanish. The question remains, though, "what is large p_T?".

7.9 Conclusions

The detailed behavior of inclusive Λ production, the cross section and the polarization, is now known within a wide range of x_F and p_T. In effect, the cross section results are a measure of the incoherent sum of amplitudes giving a final state Λ, but the polarization is a measure of the overall phase of the amplitudes. One might hope to correlate the behavior of the polarization with the Λ cross section at some particular p_T such as $p_T \simeq 1$ GeV/c where there is the distinct change in the behavior of $\mathbb{P}(p_T)$. There are however no clear indications of a change in $Ed^3\sigma/dp^3$. In fact the behavior of the Λ cross section is monotonous compared to the polarization.

The absence of observable polarization in the $\bar{\Lambda}$ data seems to reflect the difference in the Λ and $\bar{\Lambda}$ production mechanisms. The $\bar{\Lambda}$'s are always formed from quarks created by the p-p interactions. Hence the $\bar{s}$ quark (or $\bar{u}$ or $\bar{d}$) has an equal chance of accelerating or decelerating in order to recombine with the $\bar{u}$ and $\bar{d}$. The dynamical models predict no polarization from such "symmetric" recombinations.

The study of inclusively produced polarized Λ's has yielded results which are very simple in behavior but the origins of the phenomena lack a fundamental understanding. The way has been paved for further research into high energy spin physics using polarized beams and targets which may make comparisons of experiments to theory more amenable [43,44].

Appendix A

IC and SEM Calibration

The calibration of the IC with its associated charge digitizers was acheived by recording the number of protons seen by the scintillation counters and simultaneously recording the number of counts from the the IC digitizer for 50 spills. This procedure was done at very low intensities, $5x10^5$ protons per second. The calibration for the IC at these minimal intensities was found to be $1.58\pm0.08x10^4$ protons per count.

The SEM, however, was not sensitive to such low beam fluxes and could not be calibrated using the scintillation counters. Instead it was calibrated in a bootstrap fashion from the IC. It was determined, though, that there was no proton intensity at which both the IC and SEM had linear responses. The response of the IC or SEM could be monitored at each production angle be comparing their response to single spectrometer elements (i.e. MWPC 1 or S2) or the T1 trigger. The counters and chambers were known to respond linearly to within 5% (see Section 2.4) except with high intensties ($> 5x10^{10}$) at 20 mr. These very high intensity runs were excluded in the comparisons.

Figure A.1 shows the response of the IC versus the T1 trigger for 10, 12 and 20 mr. The onset of non-linearity is well defined and occurs at $2.55\pm0.09 \times10^5$ counts which corresponds to 4.03×10^9 protons. This break point was determined by fitting two lines through the data and constraining the line through the lower IC counts to have zero slope. The IC, although showing saturation effects above 2.55×10^5 counts, has a consistent response to 7×10^5 counts. The SEM response relative to the T1 trigger is shown in Fig A.2. The response is poor and exhibits fluctuations for IC 5.00×10^5 (SEM 6.5×10^3). From these observations it was concluded that the SEM was reliable only for 6.5×10^3 or more counts.

Hence the IC is used as the beam monitor for IC 5.0×10^5 counts by allowing the calibration to continuously vary if IC > 2.55×10^5. For IC $\leq 2.55\times10^5$ the calibration number, K_{IC}, is

$$K_{IC} = 1.58\pm0.08\times10^4 \text{ protons/count}$$

And for the rest of the IC range ($2.55\times10^5 < IC < 5\times10^5$),

$$K_{IC} = 1.58\times10^4 + (0.0417\pm0.0045)(IC-2.55\times10^5) \quad (A.1)$$

At IC $= 5\times10^5$ counts, the number of counts on the SEM was found to be $6.50\pm0.08\times10^3$. Then Eqn (A.1) implies that the calibration factor for the SEM is $2.02\pm0.24\times10^6$ protons per count. Since IC was not reliable above 5×10^5 counts and data was aquired at intensities exceeding this value, the

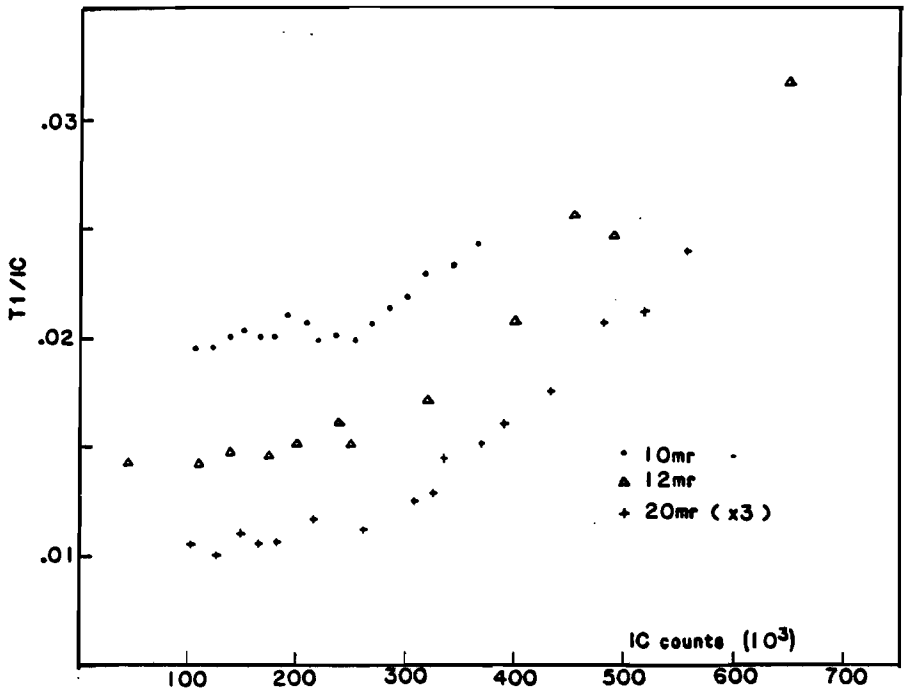

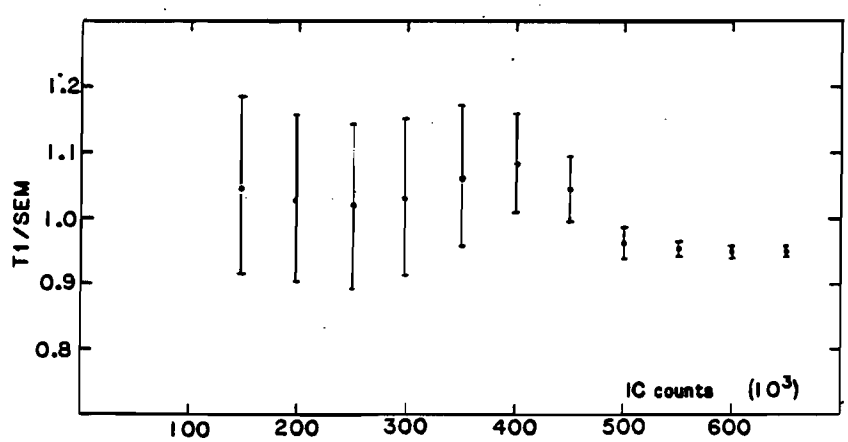

Figures A.1 (top) Values of T1/IC for a data run at each of three production angles. The break point of the linear region is thus independent of time.

A.2 (bottom) The response of the SEM as a function of IC counts is shown. The error bars shown are not statistical but represent the envelope of the spill to spill fluctuations in the SEM ouput.

SEM, with this calibration constant, was used as the primary monitor.

Appendix B

Target Absorption Corrections

Let the target have a density, ρ, total absorption cross section per nucleus, σ, and a length L, measured along the z-axis. Then for an element of length dz, the number of particles created is,

$$dn' = \frac{n_0' N_0 \rho \sigma}{A} dz \qquad (B.1)$$

where n_0' is the number of incident protons at the position of the element, L-z. The number of protons incident on the front face of the target, n_0, is attenuated at L-z by,

$$n_0' = n_0 \exp\left\{-\frac{(L-z)}{\lambda_1}\right\} \qquad (B.2)$$

where λ_1 is the proton absorption length. Similarly, the number of created particles (Λ, $\bar{\Lambda}$ or K_1^0) emerging from the end of the target is,

$$n = n' \exp\left\{\frac{-z}{\lambda_2}\right\} \qquad (B.3)$$

and λ_2 is the appropriate absorption length for the particle in the target material. Substituting (B.2) and (B.3) in (B.1) gives the number of created particles observed with the measured incident beam in an element of the target,

$$dn = n_0 \frac{N_0 \rho}{A} \sigma \exp\left\{-\frac{(L-z)}{\lambda_1}\right\} \exp\left\{\frac{-z}{\lambda_2}\right\} dz \qquad (B.4)$$

Integrating over the length of the target one obtains a relation between the actual cross section, σ, and the value of the cross section obtained from the data modified by the absorption effects, σ',

$$\sigma = c\ \sigma'$$

The correction factor, c, is then,

$$c = \frac{k\ L}{e^{-L/\lambda_1}(1-e^{-Lk})} \qquad (B.5)$$

where k is the constant,

$$k = \frac{\lambda_1 - \lambda_2}{\lambda_1 \lambda_2}$$

which contains the unknown parameter λ_2. This parameter can be eliminated by using the measured ratio of the

yields, r, between the 0.5 interaction length beryllium target (length L), and a beryllium target of a different length L'. By (B.5),

$$r = \frac{e^{-L'/\lambda_1}(1-e^{-L'k})}{e^{-L/\lambda_1}(1-e^{-Lk})} \qquad \text{(B.6)}$$

The constant k is elimiated for an arbitrary L' by numerically inverting r(k)---> k(r) and substituting in (B.5). The calcualtion used the target lengths given in Chapter 2 and λ_1= 36.7 cm [12a]. The following table lists the two values of r for each particle and the values of the correction factor (B.5).

Targets

L/λ_1	r_Λ	c_Λ	$r_{\bar{\Lambda}}$	$c_{\bar{\Lambda}}$	r_K	c_K
0.2	2.22	1.30	2.09	1.35	2.17	1.28
0.3	1.50	1.31	1.47	1.34	1.52	1.25

The numbers used in the analysis, Table 4.1, are the values of c averaged over the two target ratios.

The values of c for the copper and lead targets

could not be obtained in the above manner since only one target for each material was used. To infer c_{Cu} and c_{Pb} some approximations must be made to allow the use of r, measured only with beryllium. As in Reference 9, the observation was made that c is insensitive to variations in L/λ_1. It was found that c varies by only 0.6% when L/λ_1 varies from 0. to 0.5. Therefore, (B.5) can be approximated in the limit $L/\lambda_1 \dashrightarrow 0$ by

$$c \simeq \frac{L}{\lambda_2}\left(1-e^{-L/\lambda_2}\right)^{-1} \qquad \text{(B.7)}$$

Assume also that the particle absorption length for target j scales like the proton absorption length,

$$\lambda_2^j = \frac{\lambda_1^j}{\lambda_1}\lambda_2 \qquad \text{(B.8)}$$

Then (B.7) becomes,

$$c \simeq \frac{L_j\lambda_1}{\lambda_2\lambda_1^j}\left\{1-\exp\left(\frac{L_j\lambda_1}{\lambda_2\lambda_1^j}\right)\right\}^{-1} \qquad \text{(B.9)}$$

With the same approximation used in (B.7), (B.6) is

$$r \simeq \frac{e^{-L'/\lambda_1}\left(1-e^{-L'/\lambda_2}\right)}{e^{-L/\lambda_1}\left(1-e^{-L/\lambda_2}\right)} \qquad \text{(B.10)}$$

Now (B.9) and (B.10) are numerically solved to eliminate λ_2 and give the estimated correction c for copper and lead

given in Table 4.1. The values used in the calculation were λ_1^{Cu}= 14.8 cm and λ_1^{Pb}= 18.5 cm. The table below lists the values of c_{Cu} and c_{Pb} derived from the given values of r for each particle.

Target L/λ_1	r_{Be}	c_{Cu}	c_{Pb}
0.2	2.22	1.22	1.18
0.3	1.50	1.23	1.19
0.2	2.09	1.28	1.24
0.3	1.47	1.29	1.24
0.2	2.17	1.20	1.17
0.3	1.52	1.18	1.15

Appendix C

This Appendix contains four tables of data and correction factors used in the computations of the cross sections. Table C.1 is a compilation of the number of Λ's, $\bar{\Lambda}$'s and K_S^0's per incident proton (yields) corrected (run by run) for the electronic dead time. Table C.2 lists the momentum dependent correction factors described in Sec. 4.4. Finally Table C.4 lists the number of decays used in the cross section analysis per angle and target.

$$\text{Yield} = \frac{N}{I} \cdot d$$

BE	p	Λ $\theta_p > 0$	Λ $\theta_p < 0$	$\bar{\Lambda}$	K^0_s
6 MR	75.	2.858E-08	3.126E-08	8.958E-09	1.343E-09
	85.	9.524E-08	1.380E-07	8.273E-09	1.744E-09
	95.	1.643E-07	2.091E-07	6.319E-09	1.919E-09
	105.	2.037E-07	2.307E-07	5.326E-09	1.969E-09
	115.	2.254E-07	2.385E-07	3.826E-09	1.731E-09
	125.	2.231E-07	2.471E-07	2.662E-09	1.413E-09
	135.	2.115E-07	2.282E-07	1.880E-09	1.082E-09
	145.	1.895E-07	2.006E-07	1.111E-09	8.072E-10
	155.	1.640E-07	1.707E-07	7.630E-10	5.778E-10
	165.	1.394E-07	1.440E-07	3.836E-10	4.109E-10
	175.	1.158E-07	1.196E-07	2.230E-10	2.681E-10
	185.	9.640E-08	9.956E-08	1.119E-10	1.698E-10
	195.	7.800E-08	8.036E-08	6.180E-11	1.311E-10
	205.	6.162E-08	6.364E-08	2.617E-11	6.739E-11
	215.	4.844E-08	5.003E-08	0.	4.661E-11
	225.	3.659E-08	3.779E-08	0.	2.225E-11
	235.	2.739E-08	2.829E-08	0.	0.
	245.	2.016E-08	2.082E-08	0.	0.
	255.	1.422E-08	1.469E-08	0.	0.
	265.	1.012E-08	1.046E-08	0.	0.
	275.	7.015E-09	7.246E-09	0.	0.
	285.	4.923E-09	5.085E-09	0.	0.
	295.	3.357E-09	3.467E-09	0.	0.
	305.	2.185E-09	2.257E-09	0.	0.
	315.	1.306E-09	1.349E-09	0.	0.
	325.	9.773E-10	1.009E-09	0.	0.
	335.	5.684E-10	5.871E-10	0.	0.
	345.	3.381E-10	3.492E-10	0.	0.
	355.	1.788E-10	1.846E-10	0.	0.
	365.	1.134E-10	1.171E-10	0.	0.
	375.	6.859E-11	7.084E-11	0.	0.
	385.	3.584E-11	3.702E-11	0.	0.
7 MR	75.	1.772E-08	3.718E-08	6.434E-09	8.957E-10
	85.	5.800E-08	9.831E-08	5.675E-09	1.049E-09
	95.	9.582E-08	1.426E-07	4.431E-09	1.153E-09
	105.	1.123E-07	1.601E-07	3.143E-09	1.056E-09
	115.	1.174E-07	1.574E-07	2.186E-09	8.891E-10
	125.	1.103E-07	1.416E-07	1.123E-09	6.855E-10
	135.	9.425E-08	1.189E-07	8.029E-10	4.708E-10
	145.	7.878E-08	9.752E-08	5.812E-10	3.380E-10
	155.	6.345E-08	7.724E-08	2.660E-10	2.166E-10
	165.	5.008E-08	6.049E-08	1.397E-10	1.397E-10
	175.	3.864E-08	4.667E-08	7.735E-11	9.314E-11
	185.	2.970E-08	3.588E-08	1.322E-11	5.501E-11
	195.	2.238E-08	2.704E-08	5.088E-12	3.462E-11
	205.	1.677E-08	2.026E-08	5.057E-12	2.447E-11
	215.	1.217E-08	1.470E-08	0.	1.134E-11
	225.	8.285E-09	1.001E-08	0.	4.871E-12
	235.	5.785E-09	6.988E-09	0.	0.
	245.	3.887E-09	4.695E-09	0.	0.
	255.	2.563E-09	3.096E-09	0.	0.
	265.	1.856E-09	2.242E-09	0.	0.
	275.	1.052E-09	1.271E-09	0.	0.
	285.	6.836E-10	8.257E-10	0.	0.
	295.	3.860E-10	4.662E-10	0.	0.
	305.	2.821E-10	3.408E-10	0.	0.
	315.	1.432E-10	1.730E-10	0.	0.
	325.	8.073E-11	9.752E-11	0.	0.
	335.	5.026E-11	6.071E-11	0.	0.
	345.	4.670E-11	5.641E-11	0.	0.
	355.	1.722E-11	2.080E-11	0.	0.

TABLE C.1

$$\text{Yield} = \frac{N}{I} \cdot d$$

BE	p	Λ $\theta_p > 0$	Λ $\theta_p < 0$	$\bar{\Lambda}$	K^0_s
10 MR	75.	1.187E-08	2.319E-08	4.174E-09	5.214E-10
	85.	3.258E-08	5.144E-08	3.278E-09	5.927E-10
	95.	4.592E-08	6.367E-08	2.218E-09	5.233E-10
	105.	4.595E-08	6.088E-08	1.415E-09	4.262E-10
	115.	4.193E-08	5.239E-08	7.834E-10	3.054E-10
	125.	3.599E-08	4.305E-08	4.399E-10	1.989E-10
	135.	2.787E-08	3.276E-08	2.284E-10	1.276E-10
	145.	2.062E-08	2.377E-08	1.344E-10	7.633E-11
	155.	1.483E-08	1.682E-08	7.272E-11	4.814E-11
	165.	1.016E-08	1.144E-08	3.256E-11	2.800E-11
	175.	6.780E-09	7.629E-09	1.014E-11	1.583E-11
	185.	4.527E-09	5.094E-09	5.682E-12	8.699E-12
	195.	2.988E-09	3.362E-09	0.	4.737E-12
	205.	1.833E-09	2.062E-09	0.	2.594E-12
	215.	1.202E-09	1.353E-09	0.	1.671E-12
	225.	7.232E-10	8.137E-10	0.	6.361E-13
	235.	4.321E-10	4.862E-10	0.	0.
	245.	2.620E-10	2.948E-10	0.	0.
	255.	1.466E-10	1.649E-10	0.	0.
	265.	9.199E-11	1.035E-10	0.	0.
	275.	5.042E-11	5.673E-11	0.	0.
	285.	2.820E-11	3.173E-11	0.	0.
	295.	1.639E-11	1.844E-11	0.	0.
	305.	8.103E-12	9.117E-12	0.	0.
	315.	3.941E-12	4.434E-12	0.	0.
	325.	4.279E-12	4.814E-12	0.	0.
12 MR	75.	7.169E-09	1.150E-08	2.472E-09	2.939E-10
	85.	1.858E-08	2.409E-08	1.773E-09	3.135E-10
	95.	2.443E-08	2.781E-08	1.073E-09	2.482E-10
	105.	2.224E-08	2.424E-08	6.119E-10	1.881E-10
	115.	1.792E-08	1.839E-08	3.223E-10	1.254E-10
	125.	1.294E-08	1.270E-08	1.704E-10	7.569E-11
	135.	8.744E-09	8.438E-09	8.434E-11	4.184E-11
	145.	5.731E-09	5.444E-09	4.153E-11	2.266E-11
	155.	3.702E-09	3.446E-09	2.092E-11	1.203E-11
	165.	2.318E-09	2.141E-09	1.126E-11	6.593E-12
	175.	1.413E-09	1.306E-09	4.348E-12	3.582E-12
	185.	8.696E-10	8.033E-10	1.396E-12	2.004E-12
	195.	5.064E-10	4.678E-10	8.698E-13	1.017E-12
	205.	3.065E-10	2.832E-10	5.282E-13	6.067E-13
	215.	1.822E-10	1.683E-10	0.	3.106E-13
	225.	1.064E-10	9.827E-11	0.	1.486E-13
	235.	5.948E-11	5.494E-11	0.	2.838E-14
	245.	3.178E-11	2.935E-11	0.	0.
	255.	1.988E-11	1.836E-11	0.	0.
	265.	8.934E-12	8.252E-12	0.	0.
	275.	3.365E-12	3.109E-12	0.	0.
	285.	2.621E-12	2.421E-12	0.	0.
	295.	1.834E-12	1.694E-12	0.	0.
20 MR	75.	8.135E-10	1.387E-09	4.868E-10	6.055E-11
	85.	1.681E-09	2.315E-09	2.479E-10	3.907E-11
	95.	1.766E-09	2.137E-09	1.084E-10	2.291E-11
	105.	1.241E-09	1.437E-09	4.607E-11	1.254E-11
	115.	7.673E-10	8.366E-10	1.787E-11	6.186E-12
	125.	4.263E-10	4.449E-10	7.192E-12	2.752E-12
	135.	2.195E-10	2.251E-10	2.773E-12	1.302E-12
	145.	1.082E-10	1.089E-10	9.940E-13	5.135E-13
	155.	5.100E-11	5.047E-11	4.437E-13	2.099E-13
	165.	2.474E-11	2.429E-11	1.180E-13	1.020E-13
	175.	1.205E-11	1.183E-11	1.081E-14	3.905E-14
	185.	5.574E-12	5.472E-12	2.118E-14	1.229E-14
	195.	2.513E-12	2.467E-12	0.	5.819E-15
	205.	1.425E-12	1.399E-12	0.	6.105E-15
	215.	5.856E-13	5.749E-13	0.	1.362E-15
	225.	2.195E-13	2.155E-13	0.	1.405E-15
	235.	1.071E-13	1.051E-13	0.	0.
	245.	4.931E-14	4.841E-14	0.	0.
	255.	1.989E-14	1.953E-14	0.	0.

TABLE C.1 cont.

$$\text{Yield} = \frac{N}{\Gamma} \cdot d$$

COPPER	P	Λ $\theta_p > 0$	Λ $\theta_p < 0$	$\bar{\Lambda}$	K_s^o
7 MR	75.	2.305E-08	3.821E-08	5.408E-09	8.230E-09
	85.	7.036E-08	9.426E-08	4.865E-09	1.043E-08
	95.	1.083E-07	1.274E-07	3.858E-09	1.097E-08
	105.	1.195E-07	1.346E-07	2.665E-09	1.077E-08
	115.	1.219E-07	1.292E-07	1.577E-09	7.990E-09
	125.	1.071E-07	1.087E-07	1.171E-09	6.183E-09
	135.	9.227E-08	9.202E-08	9.853E-10	4.339E-09
	145.	7.311E-08	7.348E-08	4.772E-10	2.856E-09
	155.	6.211E-08	5.976E-08	1.314E-10	2.246E-09
	165.	4.784E-08	4.568E-08	1.668E-10	1.648E-09
	175.	3.589E-08	3.426E-08	5.950E-11	9.114E-10
	185.	2.901E-08	2.769E-08	0.	4.204E-10
	195.	2.083E-08	1.988E-08	0.	5.119E-10
	205.	1.557E-08	1.487E-08	2.813E-13	1.463E-10
	215.	1.236E-08	1.180E-08	0.	1.179E-10
	225.	8.006E-09	7.643E-09	0.	1.821E-10
	235.	5.594E-09	5.340E-09	0.	1.994E-13
	245.	3.398E-09	3.244E-09	0.	0.
	255.	2.719E-09	2.596E-09	0.	0.
	265.	1.696E-09	1.619E-09	0.	0.
	275.	1.310E-09	1.250E-09	0.	0.
	285.	5.811E-10	5.547E-10	0.	0.
	295.	4.683E-10	4.471E-10	0.	0.
	305.	2.783E-10	2.657E-10	0.	0.
	315.	3.652E-10	3.487E-10	0.	0.
	325.	6.659E-11	6.357E-11	0.	0.
	335.	6.650E-11	6.349E-11	0.	0.
	345.	2.592E-11	2.474E-11	0.	0.
10 MR	75.	1.770E-08	2.668E-08	3.835E-09	4.855E-09
	85.	4.397E-08	5.335E-08	3.193E-09	5.688E-09
	95.	5.730E-08	6.127E-08	2.133E-09	5.095E-09
	105.	5.313E-08	5.441E-08	1.247E-09	4.070E-09
	115.	4.595E-08	4.429E-08	7.577E-10	3.039E-09
	125.	3.796E-08	3.502E-08	4.874E-10	1.960E-09
	135.	2.908E-08	2.637E-08	2.767E-10	1.395E-09
	145.	2.198E-08	1.955E-08	1.729E-10	8.663E-10
	155.	1.547E-08	1.353E-08	1.003E-10	5.431E-10
	165.	1.065E-08	9.239E-09	2.794E-11	2.960E-10
	175.	7.357E-09	6.385E-09	8.000E-12	2.195E-10
	185.	4.829E-09	4.191E-09	0.	8.466E-11
	195.	3.321E-09	2.882E-09	0.	4.677E-11
	205.	2.190E-09	1.901E-09	0.	2.326E-11
	215.	1.424E-09	1.236E-09	0.	1.287E-11
	225.	8.701E-10	7.552E-10	0.	3.778E-12
	235.	5.223E-10	4.533E-10	0.	0.
	245.	2.741E-10	2.379E-10	0.	0.
	255.	1.906E-10	1.654E-10	0.	0.
	265.	1.321E-10	1.147E-10	0.	0.
	275.	5.876E-11	5.099E-11	0.	0.
	285.	2.633E-11	2.285E-11	0.	0.
	295.	3.436E-11	2.982E-11	0.	0.
	305.	1.297E-11	1.126E-11	0.	0.
	315.	1.886E-12	1.637E-12	0.	0.
	325.	3.462E-12	3.004E-12	0.	0.

TABLE C.1 cont

$$\text{Yield} = \frac{N}{I} \cdot d$$

COPPER	p	Λ $\theta_p > 0$	Λ $\theta_p < 0$	$\bar{\Lambda}$	K_s^0
12 MR	75.	8.391E-09	1.672E-08	2.444E-09	3.256E-09
	85.	2.073E-08	3.337E-08	1.886E-09	3.365E-09
	95.	2.496E-08	3.329E-08	1.260E-09	2.907E-09
	105.	2.180E-08	2.952E-08	6.402E-10	2.136E-09
	115.	1.667E-08	2.124E-08	3.472E-10	1.495E-09
	125.	1.193E-08	1.455E-08	1.622E-10	9.866E-10
	135.	7.869E-09	9.431E-09	1.225E-10	4.974E-10
	145.	5.310E-09	6.243E-09	7.620E-11	2.887E-10
	155.	3.695E-09	4.273E-09	3.009E-11	1.671E-10
	165.	2.197E-09	2.520E-09	2.060E-11	9.796E-11
	175.	1.320E-09	1.515E-09	3.969E-12	4.079E-11
	185.	8.739E-10	1.003E-09	0.	2.665E-11
	195.	5.038E-10	5.780E-10	0.	1.698E-11
	205.	2.386E-10	2.738E-10	0.	1.345E-11
	215.	1.946E-10	2.233E-10	0.	1.093E-12
	225.	1.494E-10	1.714E-10	0.	1.479E-12
	235.	7.517E-11	8.624E-11	0.	0.
	245.	4.092E-11	4.694E-11	0.	0.
	255.	1.386E-11	1.591E-11	0.	0.
	265.	1.045E-11	1.199E-11	0.	0.
	275.	6.344E-12	7.278E-12	0.	0.
	285.	1.548E-12	1.776E-12	0	0.
20 MR	75.	1.242E-09	2.230E-09	5.786E-10	8.003E-10
	85.	2.488E-09	3.611E-09	3.236E-10	5.274E-10
	95.	2.545E-09	3.242E-09	1.155E-10	3.212E-10
	105.	1.767E-09	2.156E-09	5.802E-11	1.948E-10
	115.	1.067E-09	1.226E-09	2.551E-11	1.093E-10
	125.	5.840E-10	6.420E-10	4.431E-12	4.691E-11
	135.	3.033E-10	3.276E-10	8.242E-12	2.011E-11
	145.	1.423E-10	1.508E-10	5.021E-12	6.682E-12
	155.	7.802E-11	8.131E-11	0	2.931E-12
	165.	3.434E-11	3.551E-11	0.	6.094E-13
	175.	2.517E-11	2.602E-11	0.	2.359E-12
	185.	1.111E-11	1.149E-11	0.	0.
	195.	8.805E-12	9.105E-12	0	0.

TABLE C.1 cont.

$$\text{Yield} = \frac{N}{I} \cdot d$$

	p	$\Theta_p > 0$ Λ	$\Theta_p < 0$	$\bar{\Lambda}$	K_s^o
LEAD 7 MR	75.	2.642E-08	3.801E-08	5.643E-09	7.597E-09
	85.	7.774E-08	9.035E-08	5.108E-09	9.795E-09
	95.	1.226E-07	1.231E-07	3.810E-09	1.000E-08
	105.	1.325E-07	1.295E-07	2.749E-09	9.358E-09
	115.	1.309E-07	1.204E-07	1.832E-09	7.699E-09
	125.	1.154E-07	1.016E-07	1.337E-09	5.713E-09
	135.	9.354E-08	8.094E-08	8.161E-10	4.643E-09
	145.	7.692E-08	6.530E-08	5.943E-10	3.061E-09
	155.	5.879E-08	4.908E-08	2.093E-10	1.869E-09
	165.	4.732E-08	3.920E-08	2.002E-10	1.275E-09
	175.	3.647E-08	3.021E-08	3.344E-11	8.632E-10
	185.	2.736E-08	2.266E-08	2.323E-11	5.790E-10
	195.	2.068E-08	1.713E-08	3.479E-11	3.432E-10
	205.	1.415E-08	1.172E-08	2.322E-11	2.234E-10
	215.	1.037E-08	8.592E-09	0.	1.336E-10
	225.	7.401E-09	6.131E-09	0.	7.215E-11
	235.	5.602E-09	4.641E-09	0.	0.
	245.	3.373E-09	2.794E-09	0.	0.
	255.	2.372E-09	1.964E-09	0.	0.
	265.	1.510E-09	1.250E-09	0.	0.
	275.	1.141E-09	9.451E-10	0.	0.
	285.	6.913E-10	5.727E-10	0.	0.
	295.	4.396E-10	3.641E-10	0.	0.
	305.	3.070E-10	2.543E-10	0.	0.
	315.	1.239E-10	1.026E-10	0.	0.
	325.	1.071E-10	8.875E-11	0.	0.
	335.	6.134E-11	5.097E-11	0.	0.
	345.	2.595E-11	2.149E-11	0.	0.
	355.	1.707E-11	1.414E-11	0.	0.
10 MR	75.	1.908E-08	3.035E-08	4.082E-09	4.874E-09
	85.	4.755E-08	6.112E-08	3.122E-09	5.893E-09
	95.	6.086E-08	6.869E-08	2.231E-09	5.334E-09
	105.	5.611E-08	6.065E-08	1.381E-09	4.432E-09
	115.	4.735E-08	4.817E-08	8.684E-10	3.225E-09
	125.	3.874E-08	3.773E-08	5.009E-10	2.245E-09
	135.	2.930E-08	2.804E-08	2.805E-10	1.444E-09
	145.	2.134E-08	2.003E-08	1.460E-10	9.624E-10
	155.	1.582E-08	1.461E-08	8.829E-11	6.226E-10
	165.	1.076E-08	9.854E-09	6.110E-11	4.046E-10
	175.	7.172E-09	6.569E-09	2.141E-11	2.101E-10
	185.	4.872E-09	4.463E-09	1.803E-11	1.340E-10
	195.	3.278E-09	3.003E-09	0.	6.086E-11
	205	2.141E-09	1.961E-09	0.	3.715E-11
	215.	1.358E-09	1.244E-09	0.	2.758E-11
	225.	7.938E-10	7.271E-10	0.	1.351E-11
	235.	5.397E-10	4.944E-10	0.	0.
	245.	2.749E-10	2.518E-10	0.	0.
	255.	1.716E-10	1.572E-10	0.	0.
	265.	9.952E-11	9.116E-11	0.	0.
	275.	6.194E-11	5.674E-11	0.	0.
	285.	4.717E-11	4.321E-11	0.	0.
	295.	2.196E-11	2.011E-11	0.	0.
	305.	1.105E-11	1.012E-11	0.	0.
	315.	7.221E-12	6.615E-12	0.	0
	325	3.557E-12	3.258E-12	0	0

TABLE C.1 cont.

$$\text{Yield} = \frac{N}{I} \cdot d$$

LEAD	p	$\Theta_p > 0$ Λ	$\Theta_p < 0$	$\bar{\Lambda}$	K_s^o
12 MR	75.	9.414E-09	1.313E-08	2.727E-09	3.234E-09
	85.	2.377E-08	3.091E-08	2.068E-09	3.274E-09
	95.	2.998E-08	3.422E-08	1.247E-09	2.753E-09
	105.	2.706E-08	2.959E-08	6.743E-10	2.212E-09
	115.	2.149E-08	2.211E-08	3.746E-10	1.384E-09
	125.	1.341E-08	1.318E-08	2.237E-10	9.296E-10
	135.	1.049E-08	1.016E-08	1.317E-10	5.344E-10
	145.	7.233E-09	6.887E-09	5.083E-11	3.031E-10
	155.	4.761E-09	4.446E-09	1.713E-11	1.374E-10
	165.	3.097E-09	2.869E-09	1.906E-11	8.377E-11
	175.	1.895E-09	1.736E-09	1.223E-12	4.729E-11
	185.	1.161E-09	1.076E-09	2.828E-12	3.835E-11
	195.	8.231E-10	7.627E-10	0.	2.035E-11
	205.	4.274E-10	3.961E-10	0.	1.369E-11
	215.	3.164E-10	2.932E-10	0.	9.783E-13
	225.	1.331E-10	1.233E-10	0.	0.
	235.	1.204E-10	1.116E-10	0.	0.
	245.	5.176E-11	4.796E-11	0.	0.
	255.	2.873E-11	2.662E-11	0.	0.
	265.	1.723E-11	1.596E-11	0.	0.
	275.	4.862E-12	4.503E-12	0.	0.
	285.	7.929E-12	7.347E-12	0.	0.
	295.	4.399E-12	4.076E-12	0.	0.
20 MR	75.	1.337E-09	2.346E-09	8.280E-10	1.018E-09
	85.	2.736E-09	4.178E-09	4.328E-10	7.034E-10
	95.	2.807E-09	3.735E-09	2.072E-10	4.289E-10
	105.	1.945E-09	2.479E-09	1.008E-10	2.620E-10
	115.	1.232E-09	1.478E-09	4.320E-11	1.326E-10
	125.	6.371E-10	7.346E-10	1.640E-11	6.680E-11
	135.	3.683E-10	4.136E-10	8.340E-12	3.205E-11
	145.	1.961E-10	2.171E-10	2.392E-12	1.266E-11
	155.	9.658E-11	1.031E-10	1.138E-12	6.317E-12
	165.	5.342E-11	5.770E-11	5.836E-13	1.724E-12
	175.	2.426E-11	2.620E-11	0.	1.945E-12
	185.	1.296E-11	1.399E-11	0.	5.601E-13
	195.	6.432E-12	6.948E-12	0.	4.394E-13
	205.	2.329E-12	2.515E-12	0.	0.
	215.	9.503E-13	1.026E-12	0.	0.
	225.	9.346E-13	1.031E-12	0.	0.
	235.	9.781E-13	1.036E-12	0.	0.

TABLE C.1 cont.

p	Λ		$\bar{\Lambda}$	K^0_S
	$\theta_p > 0$	$\theta_p < 0$		
75.	.019±.001	.033±.001	.096±.003	.031±.001
85.	.062±.002	.087±.003	.126±.004	.048±.001
95.	.112±.003	.138±.004	.152±.005	.066±.002
105.	.150±.005	.177±.005	.176±.005	.083±.002
115.	.181±.005	.201±.006	.197±.006	.096±.003
125.	.206±.006	.219±.007	.215±.006	.104±.003
135.	.224±.007	.234±.007	.228±.007	.110±.003
145.	.242±.007	.248±.007	.235±.007	.114±.003
155.	.255±.008	.257±.008	.240±.007	.116±.003
165.	.263±.008	.263±.008	.242±.007	.118±.004
175.	.267±.008	.267±.008	.241±.007	.119±.004
185.	.273±.008	.273±.008	.237±.007	.118±.004
195.	.275±.008	.275±.008	.230±.007	.117±.004
205.	.275±.008	.275±.008	.223±.007	.115±.003
215.	.274±.008	.274±.008	.212±.006	.111±.003
225.	.272±.008	.272±.008	.202±.006	.107±.003
235.	.270±.008	.270±.008	.191±.006	.103±.003
245.	.268±.008	.268±.008	.180±.005	.099±.003
255.	.265±.008	.265±.008	.168±.005	.096±.003
265.	.261±.008	.261±.008	.155±.005	.091±.003
275.	.257±.008	.257±.008	.143±.004	.087±.003
285.	.252±.008	.252±.008	.000±.000	.082±.002
295.	.247±.007	.247±.007	.000±.000	.078±.002
305.	.242±.007	.242±.007	.000±.000	.073±.002
315.	.236±.007	.236±.007	.000±.000	.069±.002
325.	.230±.007	.230±.007	.000±.000	.064±.002
335.	.223±.007	.223±.007	.000±.000	.060±.002
345.	.217±.007	.217±.007	.000±.000	.000±.000
355.	.210±.006	.210±.006	.000±.000	.000±.000
365.	.202±.006	.202±.006	.000±.000	.000±.000
375.	.195±.006	.195±.006	.000±.000	.000±.000
385.	.187±.006	.187±.006	.000±.000	.000±.000

TABLE C.2 Acceptance, $\mathcal{A}(p)$

p	6,7 mr	10, 12 mr	20 mr
75.	1.120±.105	1.140±.107	1.210±.114
85.	1.090±.058	1.120±.059	1.180±.063
95.	1.080±.055	1.100±.056	1.150±.059
105.	1.070±.050	1.100±.052	1.140±.054
115.	1.080±.050	1.100±.051	1.140±.052
125.	1.080±.048	1.110±.049	1.150±.051
135.	1.080±.045	1.110±.047	1.150±.048
145.	1.090±.044	1.120±.045	1.160±.046
155.	1.090±.044	1.120±.045	1.170±.047
165.	1.100±.044	1.130±.045	1.170±.047
175.	1.100±.044	1.130±.045	1.180±.047
185.	1.110±.044	1.140±.046	1.190±.048
195.	1.110±.046	1.140±.047	1.200±.049
205.	1.120±.047	1.150±.048	1.210±.051
215.	1.130±.050	1.160±.051	1.220±.054
225.	1.130±.051	1.170±.053	1.220±.055
235.	1.140±.054	1.170±.055	1.230±.058
245.	1.150±.055	1.180±.057	1.240±.060
255.	1.160±.059	1.190±.061	1.250±.064
265.	1.160±.061	1.200±.064	1.260±.067
275.	1.170±.063	1.200±.065	1.270±.069
285.	1.180±.065	1.210±.067	1.270±.070
295.	1.180±.067	1.220±.070	1.280±.073
305.	1.190±.069	1.220±.071	1.290±.075
315.	1.200±.070	1.230±.071	0.000±.000
325.	1.210±.070	1.240±.072	0.000±.000
335.	1.220±.071	1.250±.073	0.000±.000
345.	1.230±.071	1.260±.073	0.000±.000
355.	1.240±.072	1.270±.074	0.000±.000
365.	1.250±.073	1.280±.074	0.000±.000
375.	1.260±.073	0.000±.000	0.000±.000
385.	1.260±.073	0.000±.000	0.000±.000

TABLE C.3 Momentum Dependent Corrections, $K(p,\theta_p)$

TABLE C.4

Be	Λ	$\bar{\Lambda}$	K_s^0
6mr	2315187	47170	166965
7mr	982220	22024	63232
10mr	1504634	49973	123410
12mr	2348143	92351	208089
20mr	2115252	217552	367560
Cu			
7mr	129941	2833	8347
10mr	190650	5327	14891
12mr	178652	5765	15729
20mr	74189	15440	14713
Pb			
7mr	134293	3047	8975
10mr	194723	5903	15079
12mr	182330	5862	16045
20mr	91143	18970	18075

Appendix D

The following table contains the values of the fitted parameters c , used in the following function to fit the cross section data,

$$E\frac{d^3\sigma}{dp^3} = \exp\{f(x_F, p_T)\}\ (1-x_F)^{g(p_T)} \qquad (D.1)$$

The fuctions f and g are given by,

$$f = c1+c2x_F^2+c3x_F+c4x_F p_T+c5p_T^2+c6p_T^3+c7p_T^4 \qquad (D.2)$$

$$g = c8 + c9p_T^2 \qquad (D.3)$$

Beryllium

	Lambda	Lambda-bar	K-short
χ^2/d.f.	2.2	1.1	2.1
c1	1.106±0.027	1.66±0.13	2.39±0.04
c2	1.303±0.064	4.50±1.1	2.56±0.51
c3	4.50±0.09	-11.7±0.9	-5.17±0.20
c4	-3.96±0.04	-6.00±0.41	-4.49±0.12
c5	-2.111±0.009	-1.79±0.06	-2.281±0.018
c6	0.659±0.004	0.698±0.019	0.858±0.005
c7	-0.0654±0.0007	-0.077±0.004	-0.0951±0.0010
c8	2.37±0.05		
c9	-0.163±0.008		

Copper

	Lambda	Lambda-bar	K-short
χ^2/d.f.	0.9	1.0	0.8
c1	3.626±0.014	4.35±0.04	4.12±0.12
c2	17.71±0.12	27.7±0.3	7.74±0.5
c3	3.28±0.13	-25.2±0.3	-7.83±0.89
c4	-5.98±0.05	-5.52±0.19	-5.60±0.40
c5	-1.783±0.018	-0.336±0.026	-2.14±0.03
c6	0.648±0.007	-0.421±0.009	1.08±0.05
c7	-0.0720±0.0004	0.157±0.004	-0.170±0.12
c8	7.98±0.08		
c9	-0.240±0.024		

Lead

	Lambda	Lambda-bar	K-short
χ^2/d.f.	0.6	0.8	1.3
c1	4.549±0.012	5.08±0.05	5.09±0.03
c2	10.60±0.043	16.9±0.7	9.89±0.21
c3	0.572±0.022	-18.3±0.2	-9.65±0.2
c4	-3.97±0.04	-7.64±0.32	-9.65±0.04
c5	-1.922±0.009	-0.695±0.019	-1.441±0.005
c6	0.668±0.002	0.23±0.02	0.628±0.010
c7	-0.0736±0.0006	-0.004±0.002	-0.081±0.004
c8	5.28±0.04		
c9	-0.139±0.004		

Appendix E

The following pages contain tabulations of the the cross sections grouped according to the target material, the particle and the incident proton angle. The columns are respectively, the mean momentum, the mean production angle, Feynman x, transverse momentum, the cross section in the momentum bin in $cm^2 GeV^{-2}$, and the last column is the error computed in the cross section also in $cm^2 \cdot GeV^{-2}$. The error does not include the systematic uncertainty estimated to be 14% (Section 4.4).

MOM	ANGLE	X	PT	CROSS SEC	ERROR
BE LAMBDA					
75.71	6.19	.18	.47	2.395E-27	2.347E-28
85.49	6.17	.21	.53	2.109E-27	1.276E-28
95.29	6.14	.23	.58	1.790E-27	1.063E-28
105.17	6.10	.26	.64	1.502E-27	8.335E-29
115.07	6.06	.28	.70	1.258E-27	6.955E-29
124.98	5.99	.31	.75	1.016E-27	5.621E-29
134.94	5.91	.33	.80	8.137E-28	4.064E-29
144.90	5.85	.36	.85	6.343E-28	3.155E-29
154.87	5.79	.38	.90	4.873E-28	2.384E-29
164.85	5.75	.41	.95	3.808E-28	1.882E-29
174.82	5.71	.43	1.00	2.937E-28	1.440E-29
184.79	5.67	.46	1.05	2.283E-28	1.122E-29
194.79	5.63	.48	1.10	1.740E-28	8.593E-30
204.78	5.59	.51	1.14	1.319E-28	6.509E-30
214.75	5.54	.53	1.19	1.002E-28	4.959E-30
224.77	5.52	.56	1.24	7.281E-29	3.613E-30
234.71	5.48	.58	1.29	5.305E-29	2.629E-30
244.73	5.44	.61	1.33	3.806E-29	1.906E-30
254.70	5.42	.63	1.38	2.632E-29	1.322E-30
264.75	5.39	.66	1.43	1.830E-29	9.332E-31
274.70	5.38	.68	1.48	1.252E-29	6.521E-31
284.62	5.33	.71	1.52	8.719E-30	4.642E-31
294.67	5.32	.73	1.57	5.859E-30.	3.219E-31
304.80	5.29	.76	1.61	3.796E-30	2.232E-31
314.44	5.28	.78	1.66	2.274E-30	1.451E-31
324.55	5.24	.81	1.70	1.705E-30	1.205E-31
334.42	5.23	.83	1.75	1.001E-30	8.207E-32
344.31	5.21	.86	1.79	5.992E-31	5.768E-32
354.35	5.18	.88	1.84	3.207E-31	3.903E-32
364.50	5.13	.91	1.87	2.073E-31	2.820E-32
375.10	4.82	.94	1.81	1.272E-31	2.180E-32
384.00	4.91	.96	1.89	6.771E-32	1.610E-32
BE LAMBDA BAR					
75.01	6.18	.18	.46	5.787E-28	3.943E-29
84.91	6.12	.20	.52	3.666E-28	1.870E-29
94.83	6.13	.23	.58	2.124E-28	1.124E-29
104.73	6.10	.26	.64	1.344E-28	7.165E-30
114.60	6.06	.28	.69	7.957E-29	4.401E-30
124.65	6.07	.31	.76	4.664E-29	2.733E-30
134.64	6.02	.33	.81	2.875E-29	1.812E-30
144.77	5.96	.36	.86	1.548E-29	1.123E-30
154.58	5.98	.38	.92	9.747E-30	8.083E-31
164.67	5.95	.41	.98	4.604E-30	4.816E-31
174.39	5.92	.43	1.03	2.538E-30	3.284E-31
184.57	5.93	.46	1.09	1.234E-30	2.134E-31
194.04	5.91	.48	1.15	6.683E-31	1.537E-31
206.21	5.84	.51	1.21	2.772E-31	1.058E-31
BE K-SHORT					
75.50	6.15	.18	.46	2.425E-27	2.956E-28
85.22	6.10	.21	.52	1.754E-27	1.090E-28
95.05	6.06	.23	.58	1.246E-27	6.471E-29
104.94	6.04	.26	.63	9.129E-28	4.594E-29
114.85	5.99	.28	.69	6.471E-28	3.252E-29
124.75	5.99	.31	.75	4.437E-28	2.235E-29
134.75	5.96	.33	.80	2.976E-28	1.513E-29
144.82	5.93	.36	.86	2.011E-28	1.029E-29
154.69	5.94	.38	.92	1.325E-28	6.935E-30
164.71	5.87	.41	.97	8.776E-29	4.742E-30
174.71	5.86	.43	1.02	5.353E-29	3.007E-30
184.49	5.89	.46	1.09	3.266E-29	1.973E-30
194.75	5.81	.48	1.13	2.410E-29	1.533E-30
204.52	5.85	.51	1.20	1.211E-29	8.926E-31
214.30	5.77	.53	1.24	8.356E-30	6.864E-31
225.03	5.82	.56	1.31	3.941E-30	4.118E-31

MOM	ANGLE	X	PT	CROSS SEC	ERROR
BE LAMBDA					
75.69	7.62	.18	.58	1.607E-27	1.423E-28
85.50	7.59	.21	.65	1.388E-27	7.601E-29
95.27	7.55	.23	.72	1.129E-27	6.123E-29
105.15	7.52	.26	.79	8.870E-28	4.642E-29
115.04	7.50	.28	.86	7.087E-28	3.693E-29
124.93	7.47	.31	.93	5.387E-28	2.868E-29
134.87	7.40	.33	1.00	3.923E-28	1.967E-29
144.84	7.36	.36	1.07	2.852E-28	1.425E-29
154.79	7.32	.38	1.13	2.040E-28	1.004E-29
164.76	7.30	.41	1.20	1.480E-28	7.370E-30
174.79	7.27	.43	1.27	1.060E-28	5.254E-30
184.75	7.22	.46	1.33	7.610E-29	3.793E-30
194.70	7.18	.48	1.40	5.403E-29	2.721E-30
204.76	7.14	.51	1.46	3.884E-29	1.968E-30
214.67	7.11	.53	1.53	2.722E-29	1.400E-30
224.67	7.07	.56	1.59	1.784E-29	9.353E-31
234.65	7.04	.58	1.65	1.212E-29	6.508E-31
244.58	6.99	.61	1.71	7.940E-30	4.460E-31
254.61	6.94	.63	1.77	5.131E-30	3.046E-31
264.61	6.91	.66	1.83	3.630E-30	2.290E-31
274.63	6.86	.68	1.89	2.029E-30	1.467E-31
284.62	6.82	.71	1.94	1.309E-30	1.076E-31
294.30	6.79	.73	2.00	7.295E-31	7.385E-32
304.61	6.76	.76	2.06	5.303E-31	6.117E-32
314.19	6.77	.78	2.13	2.698E-31	4.130E-32
324.05	6.91	.81	2.24	1.526E-31	3.054E-32
334.53	6.74	.83	2.25	9.569E-32	2.385E-32
344.34	6.49	.86	2.23	8.950E-32	2.303E-32
353.70	6.74	.88	2.38	3.347E-32	1.383E-32
BE LAMBDA BAR					
74.95	7.50	.18	.56	4.354E-28	3.083E-29
84.83	7.48	.20	.63	2.516E-28	1.392E-29
94.63	7.45	.23	.70	1.447E-28	8.406E-30
104.72	7.42	.26	.78	7.933E-29	4.836E-30
114.62	7.40	.28	.85	4.547E-29	2.991E-30
124.10	7.38	.30	.92	1.977E-29	1.569E-30
134.40	7.36	.33	.99	1.230E-29	1.108E-30
144.18	7.32	.36	1.06	8.130E-30	8.470E-31
154.65	7.31	.38	1.13	3.396E-30	5.048E-31
164.69	7.29	.41	1.20	1.917E-30	3.596E-31
175.67	7.27	.44	1.28	8.761E-31	2.310E-31
185.67	7.24	.46	1.34	1.669E-31	9.678E-32
194.81	7.22	.48	1.41	5.480E-32	5.488E-32
203.92	7.14	.51	1.46	5.415E-32	5.423E-32
BE K-SHORT					
75.34	7.47	.18	.56	1.621E-27	1.991E-28
85.15	7.44	.21	.63	1.056E-27	6.716E-29
94.96	7.42	.23	.70	7.501E-28	4.012E-29
104.85	7.39	.26	.77	4.902E-28	2.364E-29
114.76	7.36	.28	.84	3.289E-28	1.732E-29
124.69	7.34	.31	.92	2.154E-28	1.153E-29
134.70	7.30	.33	.98	1.295E-28	7.184E-30
144.66	7.28	.36	1.05	8.431E-29	4.844E-30
154.63	7.25	.38	1.12	4.967E-29	3.079E-30
164.97	7.22	.41	1.19	2.979E-29	2.030E-30
174.83	7.20	.43	1.26	1.858E-29	1.409E-30
184.50	7.17	.46	1.32	1.058E-29	9.501E-31
194.24	7.14	.48	1.39	6.381E-30	6.804E-31
204.39	7.11	.51	1.45	4.401E-30	5.384E-31
214.17	7.05	.53	1.51	2.033E-30	3.442E-31
224.78	7.09	.56	1.59	8.636E-31	2.151E-31

MOM	ANGLE	X	PT	CROSS SEC	ERROR
BE LAMBDA					
75.67	10.07	.18	.76	1.057E-27	9.716E-29
85.40	10.01	.21	.85	7.744E-28	4.220E-29
95.19	9.96	.23	.95	5.324E-28	2.798E-29
105.05	9.92	.26	1.04	3.597E-28	1.788E-29
114.94	9.86	.28	1.13	2.491E-28	1.211E-29
124.84	9.81	.31	1.22	1.746E-28	8.527E-30
134.76	9.76	.33	1.32	1.152E-28	5.653E-30
144.73	9.72	.36	1.41	7.407E-29	3.677E-30
154.68	9.68	.38	1.50	4.733E-29	2.362E-30
164.70	9.65	.41	1.59	2.979E-29	1.478E-30
174.63	9.61	.43	1.68	1.846E-29	9.111E-31
184.67	9.59	.46	1.77	1.150E-29	5.734E-31
194.64	9.57	.48	1.86	7.151E-30	3.603E-31
204.70	9.55	.51	1.96	4.207E-30	2.149E-31
214.55	9.53	.53	2.04	2.665E-30	1.393E-31
224.57	9.50	.56	2.13	1.557E-30	8.383E-32
234.66	9.50	.58	2.23	8.966E-31	5.101E-32
244.55	9.48	.61	2.32	5.300E-31	3.272E-32
254.85	9.45	.63	2.41	2.902E-31	2.027E-32
264.18	9.43	.66	2.49	1.799E-31	1.432E-32
274.73	9.42	.68	2.59	9.629E-32	9.444E-33
284.68	9.41	.71	2.68	5.344E-32	6.602E-33
294.44	9.40	.73	2.77	3.089E-32	4.853E-33
305.70	9.38	.76	2.87	1.501E-32	3.288E-33
314.63	9.41	.78	2.96	7.335E-33	2.243E-33
324.07	9.46	.81	3.07	7.998E-33	2.350E-33
BE LAMBDA BAR					
74.91	9.96	.18	.75	2.877E-28	2.016E-29
84.76	9.92	.20	.84	1.495E-28	7.472E-30
94.71	9.90	.23	.94	7.370E-29	3.808E-30
104.51	9.91	.25	1.04	3.678E-29	1.952E-30
114.47	9.87	.28	1.13	1.662E-29	9.328E-31
124.22	9.77	.31	1.21	7.949E-30	4.932E-31
134.51	9.84	.33	1.32	3.594E-30	2.624E-31
144.61	9.84	.36	1.42	1.926E-30	1.686E-31
154.13	9.75	.38	1.50	9.573E-31	1.084E-31
164.13	9.72	.41	1.60	4.028E-31	6.386E-32
173.59	9.82	.43	1.70	1.190E-31	3.244E-32
183.72	9.67	.46	1.78	6.468E-32	2.313E-32
BE K-SHORT					
75.29	9.89	.18	.74	9.611E-28	5.870E-29
85.03	9.87	.20	.84	6.137E-28	3.169E-29
94.85	9.85	.23	.93	3.470E-28	1.745E-29
104.73	9.82	.26	1.03	2.035E-28	1.020E-29
114.67	9.80	.28	1.12	1.151E-28	5.843E-30
124.64	9.77	.31	1.22	6.427E-29	3.293E-30
134.64	9.73	.33	1.31	3.610E-29	1.888E-30
144.53	9.74	.36	1.41	1.958E-29	1.072E-30
154.59	9.72	.38	1.50	1.135E-29	6.552E-31
164.42	9.71	.41	1.60	6.153E-30	3.894E-31
174.35	9.68	.43	1.69	3.254E-30	2.344E-31
184.41	9.69	.46	1.79	1.720E-30	1.479E-31
195.07	9.65	.48	1.88	8.928E-31	9.596E-32
204.41	9.64	.51	1.97	4.788E-31	6.584E-32
214.35	9.65	.53	2.07	3.074E-31	5.090E-32
224.39	9.60	.56	2.15	1.170E-31	2.999E-32

MOM	ANGLE	X	PT	CROSS SEC	ERROR
BE LAMBDA					
75.90	12.13	.18	.92	5.800E-28	3.820E-29
85.26	12.09	.21	1.03	4.009E-28	1.905E-29
95.06	12.05	.23	1.15	2.570E-28	1.254E-29
104.92	12.01	.26	1.26	1.583E-28	7.755E-30
114.81	11.97	.28	1.37	9.659E-29	4.688E-30
124.73	11.92	.31	1.49	5.689E-29	2.784E-30
134.68	11.88	.33	1.60	3.276E-29	1.605E-30
144.65	11.85	.36	1.71	1.873E-29	9.200E-31
154.59	11.83	.38	1.83	1.071E-29	5.293E-31
164.60	11.79	.41	1.94	6.161E-30	3.063E-31
174.57	11.76	.43	2.05	3.489E-30	1.722E-31
184.56	11.75	.46	2.17	2.003E-30	1.006E-31
194.57	11.70	.48	2.28	1.098E-30	5.612E-32
204.55	11.70	.51	2.39	6.380E-31	3.324E-32
214.59	11.68	.53	2.51	3.659E-31	1.991E-32
224.57	11.67	.56	2.62	2.075E-31	1.197E-32
234.54	11.65	.58	2.73	1.119E-31	7.144E-33
244.74	11.62	.61	2.84	5.820E-32	4.338E-33
254.74	11.61	.63	2.96	3.567E-32	3.095E-33
264.90	11.60	.66	3.07	1.581E-32	1.865E-33
274.27	11.58	.68	3.18	5.833E-33	1.084E-33
285.58	11.55	.71	3.30	4.487E-33	9.615E-34
294.77	11.64	.73	3.43	3.129E-33	7.745E-34
BE LAMBDA BAR					
74.81	12.04	.18	.90	1.706E-28	1.134E-29
84.71	12.03	.20	1.02	8.100E-29	3.941E-30
94.61	12.01	.23	1.14	3.575E-29	1.795E-30
104.51	12.01	.25	1.25	1.591E-29	8.112E-31
114.48	11.98	.28	1.37	6.840E-30	3.599E-31
124.52	11.95	.31	1.49	3.071E-30	1.725E-31
134.66	11.92	.33	1.61	1.326E-30	8.316E-32
144.36	11.90	.36	1.72	5.964E-31	4.410E-32
154.46	11.90	.38	1.84	2.748E-31	2.566E-32
164.08	11.88	.41	1.95	1.393E-31	1.730E-32
174.40	11.89	.43	2.07	5.083E-32	9.321E-33
183.41	11.85	.45	2.17	1.592E-32	4.862E-33
195.35	11.88	.48	2.32	9.595E-33	3.946E-33
206.24	11.80	.51	2.43	5.742E-33	4.070E-33
BE K-SHORT					
75.23	12.03	.18	.90	5.422E-28	3.244E-29
84.96	12.01	.20	1.02	3.249E-28	1.666E-29
94.79	11.99	.23	1.14	1.647E-28	8.182E-30
104.74	11.97	.26	1.25	8.979E-29	4.460E-30
114.66	11.95	.28	1.37	4.730E-29	2.347E-30
124.63	11.95	.31	1.49	2.446E-29	1.216E-30
134.57	11.92	.33	1.60	1.184E-29	5.836E-31
144.57	11.94	.36	1.73	5.810E-30	2.902E-31
154.48	11.91	.38	1.84	2.837E-30	1.456E-31
164.42	11.88	.41	1.95	1.449E-30	8.007E-32
174.45	11.85	.43	2.07	7.358E-31	4.672E-32
184.58	11.81	.46	2.18	3.959E-31	2.921E-32
194.78	11.82	.48	2.30	1.919E-31	1.848E-32
204.53	11.78	.51	2.41	1.119E-31	1.386E-32
214.47	11.76	.53	2.52	5.712E-32	9.376E-33
223.87	11.79	.56	2.64	2.740E-32	6.619E-33
237.90	11.83	.59	2.81	5.114E-33	2.967E-33

MOM	ANGLE	X	PT	CROSS SEC	ERROR
BE LAMBDA					
75.28	20.40	.18	1.54	7.224E-29	1.229E-29
84.98	20.35	.20	1.73	3.951E-29	2.903E-30
94.81	20.32	.23	1.93	2.008E-29	1.260E-30
104.67	20.28	.26	2.12	9.456E-30	5.183E-31
114.57	20.23	.28	2.32	4.428E-30	2.300E-31
124.48	20.19	.31	2.51	2.006E-30	1.015E-31
134.43	20.16	.33	2.71	8.798E-31	4.497E-32
144.37	20.12	.36	2.90	3.772E-31	1.918E-32
154.38	20.11	.38	3.10	1.591E-31	8.143E-33
164.36	20.06	.41	3.30	7.029E-32	3.727E-33
174.38	20.05	.43	3.50	3.205E-32	1.783E-33
184.36	20.02	.46	3.69	1.383E-32	8.753E-34
194.27	20.00	.48	3.89	5.924E-33	4.587E-34
204.84	19.97	.51	4.09	3.213E-33	3.016E-34
214.20	19.95	.53	4.27	1.278E-33	1.740E-34
224.78	19.94	.56	4.48	4.597E-34	9.847E-35
235.29	19.92	.59	4.69	2.176E-34	6.962E-35
245.09	19.92	.61	4.88	9.770E-35	4.395E-35
255.11	19.89	.64	5.07	3.861E-35	2.737E-35
BE LAMBDA BAR					
74.51	20.32	.18	1.51	3.580E-29	2.458E-30
84.39	20.30	.20	1.71	1.196E-29	5.798E-31
94.36	20.28	.23	1.91	3.778E-30	1.891E-31
104.29	20.25	.25	2.11	1.244E-30	6.357E-32
114.22	20.23	.28	2.31	3.937E-31	2.140E-32
124.19	20.21	.31	2.51	1.347E-31	8.341E-33
134.28	20.20	.33	2.71	4.528E-32	3.542E-33
144.41	20.18	.36	2.91	1.477E-32	1.625E-33
154.21	20.15	.38	3.11	6.099E-33	9.871E-34
162.89	20.13	.40	3.28	1.523E-33	4.289E-34
177.56	20.10	.44	3.57	1.296E-34	1.298E-34
186.48	20.04	.46	3.74	2.479E-34	2.482E-34
BE K-SHORT					
74.99	20.29	.18	1.52	1.189E-28	7.468E-30
84.76	20.27	.20	1.72	4.276E-29	2.207E-30
94.58	20.24	.23	1.91	1.593E-29	7.923E-31
104.49	20.22	.25	2.11	6.221E-30	3.105E-31
114.45	20.20	.28	2.31	2.422E-30	1.193E-31
124.34	20.19	.31	2.51	9.234E-31	4.565E-32
134.45	20.17	.33	2.71	3.820E-31	1.950E-32
144.32	20.15	.36	2.91	1.372E-31	7.592E-33
154.36	20.13	.38	3.11	5.176E-32	3.492E-33
164.36	20.11	.41	3.31	2.322E-32	1.938E-33
174.38	20.09	.43	3.50	8.379E-33	1.003E-33
183.30	20.07	.45	3.68	2.551E-33	4.874E-34
194.65	20.05	.48	3.90	1.157E-33	3.137E-34
202.64	20.04	.50	4.06	1.196E-33	4.028E-34
213.99	20.00	.53	4.28	2.640E-34	1.871E-34
226.98	19.95	.56	4.53	2.663E-34	2.667E-34

	MOM	ANGLE	X	PT	CROSS SEC	ERROR
COPPER	LAMBDA					
	75.63	7.63	18	.58	7.942E-27	8.410E-28
	85.45	7.61	21	.65	6.400E-27	4.470E-28
	95.22	7.56	23	.72	4.850E-27	3.456E-28
	105.10	7.56	26	.79	3.585E-27	2.570E-28
	115.02	7.51	28	.86	2.796E-27	2.030E-28
	124.90	7.49	31	.94	1.988E-27	1.539E-28
	134.89	7.43	33	1.00	1.458E-27	1.059E-28
	144.83	7.37	36	1.07	1.033E-27	7.606E-29
	154.86	7.35	38	1.14	7.580E-28	5.499E-29
	164.81	7.32	41	1.21	5.368E-28	4.002E-29
	174.91	7.31	43	1.28	3.738E-28	2.851E-29
	184.78	7.24	46	1.34	2.822E-28	2.087E-29
	194.76	7.20	48	1.40	1.908E-28	1.494E-29
	204.83	7.15	51	1.46	1.369E-28	1.102E-29
	214.66	7.12	53	1.53	1.050E-28	8.220E-30
	224.80	7.09	56	1.59	6.541E-29	5.507E-30
	234.62	7.05	58	1.65	4.450E-29	4.046E-30
	244.56	7.03	61	1.72	2.636E-29	2.679E-30
	254.68	6.96	63	1.77	2.066E-29	2.139E-30
	264.67	6.93	66	1.83	1.259E-29	1.484E-30
	274.81	6.88	68	1.89	9.591E-30	1.284E-30
	284.85	6.83	71	1.95	4.223E-30	7.616E-31
	294.68	6.80	73	2.00	3.357E-30	7.161E-31
	304.61	6.79	76	2.07	1.986E-30	4.812E-31
	314.65	6.68	78	2.10	2.609E-30	4.743E-31
	324.26	7.11	81	2.31	4.777E-31	2.283E-31
	334.53	6.78	83	2.27	4.808E-31	2.553E-31
	343.32	6.52	86	2.24	1.892E-31	1.375E-31
COPPER	LAMBDA BAR					
	74.94	7.51	18	.56	1.588E-27	1.700E-28
	84.75	7.50	20	.64	9.370E-28	8.369E-29
	95.05	7.47	23	.71	5.441E-28	5.092E-29
	104.84	7.43	26	.78	2.916E-28	3.077E-29
	114.93	7.41	28	.85	1.419E-28	1.815E-29
	125.19	7.40	31	.93	8.865E-29	1.215E-29
	134.81	7.36	33	.99	6.532E-29	8.918E-30
	145.41	7.32	36	1.06	2.872E-29	6.550E-30
	155.93	7.51	39	1.17	8.322E-30	3.322E-30
	163.02	7.31	40	1.19	8.775E-30	2.805E-30
	173.33	7.59	43	1.32	2.956E-30	1.586E-30
	206.01	7.17	51	1.48	1.294E-32	1.296E-32
COPPER	K-SHORT					
	75.43	7.50	18	.57	6.357E-27	1.000E-27
	85.07	7.47	20	.64	4.490E-27	3.776E-28
	94.89	7.44	23	.71	3.051E-27	2.226E-28
	104.74	7.43	26	.78	2.137E-27	1.505E-28
	114.62	7.38	28	.85	1.265E-27	9.355E-29
	124.84	7.35	31	.92	8.296E-28	6.381E-29
	134.92	7.33	33	.99	5.327E-28	4.345E-29
	144.97	7.30	36	1.06	3.038E-28	2.764E-29
	154.72	7.29	38	1.13	2.200E-28	2.196E-29
	164.54	7.24	41	1.19	1.506E-28	1.589E-29
	174.55	7.22	43	1.26	7.785E-29	1.021E-29
	184.23	7.20	46	1.33	3.462E-29	7.307E-30
	193.84	7.09	48	1.37	4.041E-29	6.099E-30
	204.21	7.29	51	1.49	1.125E-29	3.293E-30
	215.15	7.09	53	1.53	8.997E-30	3.195E-30
	223.36	6.92	56	1.55	1.389E-29	2.646E-30
	239.26	7.76	60	1.86	1.488E-32	1.490E-32

	MOM	ANGLE	X	PT	CROSS SEC	ERROR
COPPER	LAMBDA					
	75.61	10.08	18	.76	5.922E-27	7.173E-28
	85.34	10.02	.21	.85	3.924E-27	2.831E-28
	95.14	9.95	.23	.95	2.493E-27	1.686E-28
	105.02	9.91	.26	1.04	1.564E-27	1.020E-28
	114.92	9.85	28	1.13	1.024E-27	6.514E-29
	124.83	9.82	.31	1.23	6.907E-28	4.451E-29
	134.79	9.79	33	1.32	4.507E-28	2.945E-29
	144.72	9.72	36	1.41	2.963E-28	1.916E-29
	154.69	9.67	.38	1.50	1.851E-28	1.238E-29
	164.71	9.65	.41	1.59	1.171E-28	7.972E-30
	174.74	9.62	43	1.68	7.511E-29	5.044E-30
	184.66	9.59	46	1.77	4.603E-29	3.233E-30
	194.72	9.59	.48	1.87	2.980E-29	2.134E-30
	204.65	9.57	.51	1.96	1.887E-29	1.350E-30
	214.57	9.52	.53	2.04	1.184E-29	9.253E-31
	224.71	9.51	.56	2.14	7.022E-30	5.841E-31
	234.74	9.50	.58	2.23	4.065E-30	4.107E-31
	244.62	9.48	.61	2.32	2.079E-30	2.499E-31
	254.63	9.47	.63	2.41	1.417E-30	2.013E-31
	264.93	9.42	.66	2.50	9.663E-31	1.466E-31
	275.24	9.43	.69	2.59	4.202E-31	9.169E-32
	284.68	9.51	.71	2.71	1.872E-31	5.880E-32
	293.85	9.30	.73	2.73	2.439E-31	5.871E-32
	305.31	9.38	.76	2.86	9.029E-32	4.398E-32
	313.30	9.66	.78	3.03	1.323E-32	2.139E-32
	327.26	9.47	.82	3.10	2.404E-32	2.133E-32
COPPER	LAMBDA BAR					
	74.88	9.97	.18	.75	1.148E-27	1.132E-28
	84.66	9.93	.20	.84	6.325E-28	4.498E-29
	94.62	9.92	.23	.94	3.078E-28	2.293E-29
	104.51	9.93	.25	1.04	1.407E-28	1.225E-29
	114.16	9.90	.28	1.13	6.992E-29	6.605E-30
	124.67	9.81	.31	1.22	3.809E-29	4.111E-30
	134.14	9.88	.33	1.33	1.895E-29	2.696E-30
	145.06	9.85	.36	1.43	1.072E-29	1.759E-30
	154.67	9.77	.38	1.51	5.711E-30	1.112E-30
	165.46	9.94	.41	1.64	1.488E-30	7.228E-31
	171.46	10.16	.42	1.74	4.128E-31	3.688E-31
COPPER	K-SHORT					
	75.36	9.89	18	.75	3.821E-27	3.306E-28
	85.01	9.85	.20	.84	2.518E-27	1.797E-28
	94.90	9.85	23	.94	1.443E-27	1.054E-28
	104.74	9.80	26	1.03	8.305E-28	6.189E-29
	114.60	9.81	28	1.12	4.900E-28	3.558E-29
	124.69	9.75	31	1.22	2.707E-28	2.097E-29
	134.57	9.73	33	1.31	1.687E-28	1.329E-29
	144.72	9.72	.36	1.41	9.486E-29	8.565E-30
	154.24	9.72	38	1.50	5.484E-29	5.333E-30
	164.15	9.71	41	1.59	2.785E-29	3.406E-30
	174.43	9.67	43	1.69	1.927E-29	2.500E-30
	184.14	9.66	46	1.78	7.164E-30	1.568E-30
	194.66	9.66	48	1.88	3.776E-30	1.113E-30
	204.59	9.65	51	1.97	1.834E-30	7.998E-31
	214.97	9.62	53	2.07	1.009E-30	6.449E-31
	225.32	9.76	56	2.20	2.957E-31	2.863E-31

	MOM	ANGLE	X	PT	CROSS SEC	ERROR
COPPER	LAMBDA					
	75.48	12.12	.18	.91	3.233E-27	2.418E-28
	85.24	12.10	.21	1.03	2.129E-27	1.204E-28
	95.07	12.09	.23	1.15	1.250E-27	7.571E-29
	104.87	12.02	.26	1.26	7.389E-28	4.661E-29
	114.79	11.98	.28	1.37	4.277E-28	2.737E-29
	124.69	11.96	.31	1.49	2.499E-28	1.656E-29
	134.65	11.87	.33	1.60	1.404E-28	9.494E-30
	144.65	11.85	.36	1.71	8.234E-29	5.543E-30
	154.51	11.86	.38	1.83	5.091E-29	3.493E-30
	164.70	11.79	.41	1.94	2.778E-29	2.030E-30
	174.53	11.78	.43	2.06	1.552E-29	1.223E-30
	184.66	11.75	.46	2.17	9.578E-30	8.202E-31
	194.55	11.72	.48	2.28	5.203E-30	4.769E-31
	204.52	11.73	.51	2.40	2.365E-30	3.148E-31
	214.40	11.69	.53	2.51	1.862E-30	2.492E-31
	224.32	11.68	.56	2.62	1.388E-30	2.105E-31
	234.24	11.67	.58	2.73	6.740E-31	1.273E-31
	244.98	11.63	.61	2.85	3.564E-31	9.019E-32
	252.66	11.63	.63	2.94	1.194E-31	6.532E-32
	265.76	11.60	.66	3.08	8.763E-32	4.062E-32
	276.12	11.59	.69	3.20	5.199E-32	3.615E-32
	288.95	11.55	.72	3.34	1.246E-32	1.785E-32
COPPER	LAMBDA BAR					
	74.61	12.04	.18	.90	7.340E-28	6.837E-29
	84.74	12.03	.20	1.02	3.733E-28	2.813E-29
	94.44	12.03	.23	1.14	1.822E-28	1.513E-29
	104.64	12.01	.26	1.26	7.215E-29	7.319E-30
	114.45	11.98	.28	1.37	3.196E-29	3.873E-30
	124.39	11.95	.31	1.49	1.270E-29	2.048E-30
	134.49	11.91	.33	1.60	8.370E-30	1.460E-30
	144.29	11.80	.36	1.70	4.749E-30	9.125E-31
	153.89	11.89	.38	1.83	1.722E-30	6.045E-31
	167.87	11.75	.42	1.97	1.081E-30	3.731E-31
	172.71	12.11	.43	2.09	2.033E-31	2.566E-31
COPPER	K-SHORT					
	75.20	12.00	.18	.90	2.568E-27	1.996E-28
	84.99	12.00	.20	1.02	1.490E-27	1.035E-28
	94.80	11.98	.23	1.14	8.243E-28	5.633E-29
	104.75	11.96	.26	1.25	4.359E-28	3.036E-29
	114.70	11.94	.28	1.37	2.410E-28	1.786E-29
	124.47	11.91	.31	1.48	1.365E-28	1.096E-29
	134.39	11.89	.33	1.60	6.024E-29	5.528E-30
	144.22	11.90	.36	1.72	3.172E-29	3.334E-30
	155.09	11.90	.38	1.85	1.677E-29	2.019E-30
	164.77	11.84	.41	1.95	9.183E-30	1.361E-30
	174.19	11.82	.43	2.06	3.587E-30	8.988E-31
	184.46	11.79	.46	2.17	2.252E-30	5.884E-31
	193.62	11.64	.48	2.25	1.378E-30	4.768E-31
	204.73	11.59	.51	2.37	1.060E-30	3.722E-31
	210.87	11.90	.52	2.51	8.734E-32	1.415E-31
	222.01	11.75	.55	2.61	1.175E-31	2.059E-31

	MOM	ANGLE	X	PT	CROSS SEC	ERROR
COPPER	LAMBDA					
	75.19	20.39	.18	1.53	4.839E-28	8.594E-29
	84.89	20.33	.20	1.73	2.567E-28	1.983E-29
	94.73	20.31	.23	1.92	1.269E-28	8.103E-30
	104.60	20.26	.26	2.12	5.908E-29	3.232E-30
	114.38	20.19	.28	2.31	2.700E-29	1.440E-30
	124.57	20.16	.31	2.51	1.204E-29	6.621E-31
	134.39	20.13	.33	2.71	5.332E-30	3.213E-31
	144.29	20.08	.36	2.90	2.175E-30	1.522E-31
	154.96	20.08	.38	3.11	1.063E-30	9.094E-32
	164.73	20.03	.41	3.30	4.267E-31	5.073E-32
	173.53	20.03	.43	3.48	2.949E-31	3.449E-32
	184.22	20.00	.46	3.68	1.210E-31	2.573E-32
	195.74	19.86	.49	3.89	9.032E-32	1.549E-32
COPPER	LAMBDA BAR					
	74.57	20.31	.18	1.51	1.845E-28	1.350E-29
	84.52	20.29	.20	1.72	6.765E-29	4.212E-30
	94.01	20.28	.23	1.91	1.753E-29	1.635E-30
	104.39	20.23	.25	2.11	6.793E-30	7.865E-31
	114.96	20.21	.28	2.32	2.423E-30	3.376E-31
	124.22	20.33	.31	2.53	3.600E-31	1.468E-31
	133.16	19.91	.33	2.65	5.891E-31	1.361E-31
	144.49	19.89	.36	2.87	3.237E-31	5.582E-32
COPPER	K-SHORT					
	75.09	20.32	.18	1.53	6.710E-28	4.368E-29
	84.81	20.29	.20	1.72	2.466E-28	1.368E-29
	94.65	20.24	.23	1.92	9.538E-29	5.515E-30
	104.62	20.23	.26	2.12	4.126E-29	2.682E-30
	114.68	20.23	.28	2.32	1.825E-29	1.426E-30
	124.28	20.22	.31	2.51	6.732E-30	7.007E-31
	133.80	20.20	.33	2.70	2.534E-30	3.772E-31
	144.04	20.15	.36	2.90	7.613E-31	1.747E-31
	154.99	20.14	.38	3.12	3.077E-31	1.081E-31
	164.24	20.12	.41	3.30	9.934E-32	4.480E-32
	173.71	19.76	.44	3.47	2.147E-31	5.732E-32

	MOM	ANGLE	X	PT	CROSS SEC	ERROR
LEAD	LAMBDA					
	75.60	7.64	.18	.58	2.021E-26	2.151E-27
	85.45	7.60	.21	.65	1.569E-26	1.036E-27
	95.23	7.55	.23	.72	1.218E-26	7.947E-28
	105.09	7.53	.26	.79	8.818E-27	5.553E-28
	114.97	7.48	.28	.86	6.663E-27	4.178E-28
	124.93	7.47	.31	.93	4.750E-27	3.045E-28
	134.84	7.40	.33	1.00	3.280E-27	1.985E-28
	144.84	7.37	.36	1.07	2.346E-27	1.418E-28
	154.84	7.32	.38	1.13	1.592E-27	9.524E-29
	164.76	7.29	.41	1.20	1.178E-27	7.160E-29
	174.68	7.29	.43	1.27	8.435E-28	5.136E-29
	184.80	7.23	.46	1.34	5.903E-28	3.652E-29
	194.66	7.17	.48	1.40	4.205E-28	2.660E-29
	204.75	7.14	.51	1.46	2.761E-28	1.800E-29
	214.66	7.12	.53	1.53	1.954E-28	1.323E-29
	224.66	7.06	.56	1.59	1.342E-28	9.534E-30
	234.60	7.06	.58	1.66	9.889E-29	7.385E-30
	244.90	7.01	.61	1.72	5.797E-29	4.871E-30
	254.60	6.95	.63	1.77	3.999E-29	3.709E-30
	264.31	6.93	.66	1.83	2.490E-29	2.682E-30
	274.97	6.85	.69	1.88	1.853E-29	2.222E-30
	284.56	6.81	.71	1.94	1.116E-29	1.638E-30
	294.61	6.81	.73	2.01	6.991E-30	1.262E-30
	305.17	6.78	.76	2.07	4.851E-30	1.036E-30
	313.08	6.93	.78	2.17	1.973E-30	6.412E-31
	325.35	6.90	.81	2.24	1.699E-30	5.965E-31
	334.92	6.74	.84	2.26	9.859E-31	4.503E-31
	343.28	6.51	.86	2.23	4.202E-31	2.915E-31
	354.17	6.76	.88	2.40	2.792E-31	2.368E-31
LEAD	LAMBDA BAR					
	74.94	7.49	.18	.56	3.953E-27	3.686E-28
	84.93	7.49	.20	.64	2.341E-27	1.822E-28
	94.76	7.45	.23	.71	1.285E-27	1.083E-28
	104.76	7.41	.26	.78	7.178E-28	6.582E-29
	114.82	7.38	.28	.85	3.937E-28	4.111E-29
	124.23	7.38	.31	.92	2.433E-28	2.880E-29
	134.33	7.36	.33	.99	1.295E-28	1.898E-29
	144.18	7.31	.36	1.05	8.603E-29	1.486E-29
	153.59	7.36	.38	1.13	2.784E-29	8.039E-30
	164.19	7.29	.41	1.20	2.494E-29	7.406E-30
	174.77	7.41	.43	1.30	4.165E-30	2.885E-30
	187.44	7.36	.47	1.38	2.611E-30	2.213E-30
	193.88	7.21	.48	1.40	3.897E-30	2.700E-30
	204.94	7.13	.51	1.46	2.560E-30	2.169E-30
LEAD	K-SHORT					
	75.49	7.46	.18	.56	1.498E-26	2.243E-27
	84.92	7.43	.20	.63	1.079E-26	8.619E-28
	94.90	7.40	.23	.70	7.105E-27	4.867E-28
	104.84	7.37	.26	.77	4.740E-27	3.209E-28
	114.75	7.36	.28	.84	3.109E-27	2.154E-28
	124.75	7.31	.31	.91	1.939E-27	1.418E-28
	134.44	7.30	.33	.98	1.397E-27	1.050E-28
	144.72	7.25	.36	1.05	8.330E-28	6.816E-29
	154.52	7.25	.38	1.12	4.681E-28	4.390E-29
	164.86	7.21	.41	1.19	2.971E-28	3.158E-29
	174.74	7.20	.43	1.26	1.885E-28	2.313E-29
	185.16	7.15	.46	1.32	1.212E-28	1.743E-29
	194.79	7.11	.48	1.39	6.927E-29	1.246E-29
	203.57	7.09	.51	1.44	4.443E-29	9.654E-30
	215.66	7.03	.54	1.52	2.598E-29	7.148E-30
	224.17	7.21	.56	1.62	1.400E-29	5.133E-30

	MOM	ANGLE	X	PT	CROSS SEC	ERROR
LEAD	LAMBDA					
	75.36	10.07	18	.76	1.562E-26	1.721E-27
	85.31	10.00	21	.85	1.038E-26	6.801E-28
	95.14	9.95	.23	95	6.480E-27	4.031E-28
	105.00	9.89	.26	1.04	4.042E-27	2.413E-28
	114.90	9.84	.28	1.13	2.583E-27	1.510E-28
	124.81	9.78	.31	1.22	1.725E-27	1.014E-28
	134.71	9.76	.33	1.31	1.112E-27	6.584E-29
	144.74	9.71	.36	1.41	7.037E-28	4.229E-29
	154.68	9.68	.38	1.50	4.633E-28	2.813E-29
	164.72	9.64	41	1.59	2.894E-28	1.761E-29
	174.71	9.58	43	1.67	1.792E-28	1.099E-29
	184.63	9.56	.46	1.77	1.137E-28	7.166E-30
	194.62	9.58	.48	1.86	7.201E-29	4.699E-30
	204.67	9.54	.51	1.95	4.512E-29	3.080E-30
	214.72	9.51	53	2.04	2.762E-29	2.032E-30
	224.67	9.49	.56	2.13	1.567E-29	1.284E-30
	234.70	9.50	.58	2.23	1.028E-29	9.374E-31
	244.98	9.45	61	2.32	5.095E-30	5.815E-31
	255.01	9.44	.63	2.41	3.117E-30	4.268E-31
	264.92	9.44	.66	2.50	1.781E-30	3.055E-31
	273.83	9.41	.68	2.58	1.089E-30	2.322E-31
	283.47	9.38	.71	2.66	8.241E-31	1.991E-31
	293.90	9.40	.73	2.76	3.806E-31	1.332E-31
	303.13	9.50	76	2.88	1.894E-31	9.310E-32
	315.84	9.39	79	2.97	1.229E-31	7.379E-32
	321.23	9.45	.80	3.03	6.157E-32	5.217E-32
LEAD	LAMBDA BAR					
	74.96	9.95	.18	.75	2.909E-27	2.564E-28
	84.84	9.92	20	.84	1.472E-27	9.921E-29
	94.67	9.87	.23	.93	7.672E-28	5.484E-29
	104.88	9.90	.26	1.04	3.704E-28	2.883E-29
	114.65	9.86	.28	1.13	1.903E-28	1.657E-29
	124.42	9.77	.31	1.22	9.352E-29	9.737E-30
	134.36	9.83	.33	1.32	4.573E-29	6.006E-30
	144.44	9.82	.36	1.42	2.168E-29	3.836E-30
	154.37	9.74	.38	1.50	1.201E-29	2.779E-30
	164.18	9.59	.41	1.57	7.819E-30	2.149E-30
	174.43	9.80	.43	1.71	2.589E-30	1.181E-30
	187.42	9.49	.47	1.78	2.083E-30	1.025E-30
LEAD	K-SHORT					
	75.26	9.93	.18	75	9.811E-27	7.483E-28
	85.08	9.88	20	84	6.658E-27	4.306E-28
	94.96	9.88	.23	.94	3.856E-27	2.438E-28
	104.78	9.86	26	1.03	2.309E-27	1.470E-28
	114.75	9.84	.28	1.13	1.327E-27	8.706E-29
	124.63	9.80	.31	1.22	7.921E-28	5.383E-29
	134.55	9.75	.33	1.31	4.462E-28	3.227E-29
	144.46	9.75	36	1.41	2.696E-28	2.118E-29
	154.74	9.73	38	1.50	1.600E-28	1.397E-29
	164.36	9.73	41	1.60	9.711E-29	9.660E-30
	174.65	9.72	43	1.70	4.705E-29	5.924E-30
	184.36	9.70	46	1.79	2.894E-29	4.357E-30
	195.15	9.66	.49	1.89	1.252E-29	2.677E-30
	203.80	9.62	51	1.96	7.509E-30	2.014E-30
	213.86	9.51	53	2.03	5.551E-30	1.698E-30
	226.16	9.46	56	2.14	2.691E-30	1.151E-30

	MOM	ANGLE	X	PT	CROSS SEC	ERROR
LEAD	LAMBDA					
	75.59	12.14	18	.92	7.751E-27	6.374E-28
	85.24	12.09	21	1.03	5.226E-27	3.247E-28
	95.08	12.06	23	1.15	3.212E-27	2.137E-28
	104.92	12.02	.26	1.26	1.962E-27	1.358E-28
	114.86	11.99	.28	1.38	1.179E-27	8.273E-29
	124.76	11.92	.31	1.49	6.902E-28	5.009E-29
	134.69	11.90	.33	1.60	4.005E-28	2.958E-29
	144.68	11.87	.36	1.72	2.407E-28	1.761E-29
	154.65	11.82	38	1.83	1.402E-28	1.044E-29
	164.55	11.78	41	1.94	8.388E-29	6.547E-30
	174.62	11.78	.43	2.06	4.765E-29	3.941E-30
	184.57	11.77	46	2.17	2.725E-29	2.444E-30
	194.62	11.72	.48	2.28	1.819E-29	1.625E-30
	204.38	11.70	.51	2.39	9.072E-30	1.110E-30
	214.35	11.68	.53	2.50	6.482E-30	7.940E-31
	224.32	11.69	.56	2.62	2.648E-30	4.693E-31
	234.96	11.67	.58	2.74	2.304E-30	3.941E-31
	244.96	11.64	.61	2.85	9.650E-31	2.441E-31
	254.34	11.62	.63	2.96	5.261E-31	2.271E-31
	265.38	11.60	.66	3.08	3.096E-31	1.253E-31
	273.44	11.73	.68	3.21	8.611E-32	7.602E-32
	286.93	11.49	.72	3.30	1.376E-31	9.751E-32
	292.74	11.55	.73	3.38	7.698E-32	4.370E-32
LEAD	LAMBDA BAR					
	74.79	12.04	.18	.90	1.948E-27	1.961E-28
	84.72	12.02	.20	1.02	9.762E-28	7.892E-29
	94.51	12.00	.23	1.13	4.296E-28	3.866E-29
	104.36	12.01	.25	1.25	1.817E-28	1.955E-29
	114.71	11.96	.28	1.37	8.205E-29	1.034E-29
	124.66	11.93	.31	1.49	4.206E-29	6.297E-30
	134.73	11.92	33	1.61	2.141E-29	3.844E-30
	143.82	11.87	35	1.71	7.579E-30	1.875E-30
	154.20	11.73	.38	1.81	2.332E-30	1.142E-30
	165.91	11.69	41	1.94	2.413E-30	9.169E-31
	171.49	11.97	.42	2.05	1.509E-31	3.613E-31
	186.85	11.85	.46	2.21	3.276E-31	3.343E-31
LEAD	K-SHORT					
	75.21	12.00	18	.90	6.554E-27	5.371E-28
	84.92	11.96	20	1.02	3.706E-27	2.716E-28
	94.75	11.95	.23	1.13	1.995E-27	1.442E-28
	104.79	11.96	.26	1.25	1.153E-27	8.374E-29
	114.67	11.93	.28	1.37	6.519E-28	4.994E-29
	124.60	11.93	31	1.49	3.280E-28	2.771E-29
	134.63	11.91	.33	1.60	1.650E-28	1.526E-29
	145.02	11.93	.36	1.73	8.516E-29	8.955E-30
	154.80	11.89	38	1.84	4.045E-29	5.082E-30
	164.98	11.86	41	1.96	2.003E-29	3.221E-30
	174.09	11.82	43	2.06	1.062E-29	2.514E-30
	184.12	11.68	46	2.15	8.290E-30	1.836E-30
	194.71	11.60	48	2.26	4.195E-30	1.343E-30
	204.28	11.59	51	2.37	2.760E-30	9.661E-31
	211.20	11.73	.52	2.48	1.995E-31	3.440E-31

	MOM	ANGLE	X	PT	CROSS SEC	ERROR
LEAD	LAMBDA					
	75. 21	20. 39	. 18	1. 53	1 287E-27	2. 020E-28
	85. 00	20. 33	. 20	1. 73	6. 912E-28	4. 725E-29
	94. 78	20. 31	. 23	1. 92	3. 405E-28	1. 992E-29
	104. 65	20. 25	. 26	2. 12	1. 382E-28	8. 138E-30
	114. 58	20. 23	. 28	2. 32	7. 584E-29	3. 743E-30
	124. 47	20. 16	31	2. 51	3. 301E-29	1. 743E-30
	134 57	20. 14	. 33	2. 71	1 574E-29	8. 149E-31
	144. 38	20. 09	. 36	2. 90	7. 292E-30	4 036E-31
	154 40	20. 09	38	3. 10	3. 214E-30	2 035E-31
	164. 38	20. 03	. 41	3. 29	1. 619E-30	1 211E-31
	174. 70	20. 02	. 43	3. 50	6. 873E-31	6 758E-32
	184. 84	20. 01	. 46	3. 70	3. 422E-31	4 438E-32
	193. 99	19. 97	. 48	3. 87	1. 620E-31	2. 905E-32
	206. 26	19. 97	. 51	4. 12	5. 563E-32	1. 635E-32
	214. 60	19. 91	. 53	4. 27	2. 208E-32	1. 019E-32
	223. 51	19. 82	. 56	4. 43	2. 145E-32	9. 897E-33
	233. 16	19. 66	. 58	4. 58	2. 140E-32	9. 874E-33
LEAD	LAMBDA BAR					
	74. 59	20. 30	. 18	1. 51	6. 296E-28	4. 134E-29
	84. 54	20. 28	. 20	1. 71	2. 257E-28	1. 148E-29
	94. 27	20. 27	. 23	1. 91	7. 483E-29	4. 338E-30
	104. 08	20. 21	. 25	2. 10	2. 823E-29	1 933E-30
	114. 19	20. 19	. 28	2. 31	9. 851E-30	8. 792E-31
	124. 41	20. 17	. 31	2. 51	3. 173E-30	4. 177E-31
	134. 08	20. 17	. 33	2. 70	1. 445E-30	2. 549E-31
	144. 78	20. 15	. 36	2. 92	3. 976E-31	1. 230E-31
	155. 24	20. 14	. 38	3. 13	1. 637E-31	7. 552E-32
	163. 67	20. 05	. 41	3. 28	7. 756E-32	5. 048E-32
LEAD	K-SHORT					
	74. 99	20. 27	. 18	1. 52	2. 183E-27	1. 310E-28
	84. 85	20. 27	. 20	1. 72	8. 419E-28	4. 254E-29
	94. 73	20. 24	. 23	1. 92	3. 250E-28	1. 632E-29
	104. 51	20. 22	. 25	2. 11	1. 419E-28	7. 486E-30
	114. 44	20. 21	. 28	2. 31	5. 667E-29	3. 255E-30
	124. 49	20. 17	. 31	2. 51	2. 444E-29	1. 603E-30
	134. 47	20. 18	. 33	2. 71	1. 027E-29	8. 319E-31
	144. 08	20. 14	. 36	2. 90	3. 684E-30	4. 051E-31
	153. 99	20. 11	. 38	3. 10	1. 705E-30	2. 516E-31
	163. 59	20. 20	. 40	3. 30	4. 305E-31	1. 155E-31
	173. 80	19. 80	. 43	3. 44	4. 571E-31	1. 137E-31
	188. 12	19. 82	. 47	3. 73	1. 237E-31	5. 702E-32
	195. 73	19. 79	49	3. 87	9. 485E-32	5. 044E-32

Appendix F

This section gives the values for $\alpha(x_F, p_T)$ derived from fitting data from all three targets at each momentum (x_F) bin to:

$$E \left.\frac{d^3\sigma}{dp^3}\right|_{A=1} = E \frac{d^3\sigma}{dp^3} A^{\alpha}$$

The left hand side is the measured cross section for the target of atomic weight A, and both $\alpha(x_F, p_T)$ and the nucleon cross section are determined.

The columns give, respectively, Feynman x, transverse momentum, α, the error in α, the nucleon cross section (extrapolated) and its error.

LAMBDA

	X	PT	ALPHA	D ALPHA	NUCLEON CS	D LOGCS
7 MR						
	.18	.58	.809	.043	2.722E-28	7.296E-02
	.21	.65	.775	.027	2.535E-28	4.515E-02
	.23	.72	.757	.026	2.130E-28	4.470E-02
	.26	.79	.730	.026	1.771E-28	4.313E-02
	.28	.86	.713	.025	1.472E-28	4.295E-02
	.31	.93	.691	.026	1.170E-28	4.389E-02
	.33	1.00	.677	.025	8.845E-29	4.135E-02
	.36	1.07	.671	.024	6.507E-29	4.123E-02
	.38	1.13	.657	.024	4.829E-29	4.065E-02
	.41	1.20	.662	.025	3.454E-29	4.116E-02
	.43	1.27	.660	.025	2.477E-29	4.102E-02
	.46	1.34	.656	.025	1.808E-29	4.133E-02
	.48	1.40	.654	.025	1.281E-29	4.187E-02
	.51	1.47	.628	.026	9.804E-30	4.234E-02
	.53	1.54	.638	.026	6.801E-30	4.317E-02
	.56	1.60	.647	.027	4.322E-30	4.430E-02
	.58	1.66	.669	.028	2.781E-30	4.564E-02
	.61	1.72	.631	.031	1.976E-30	4.857E-02
	.63	1.77	.665	.033	1.201E-30	5.185E-02
	.66	1.83	.618	.038	9.353E-31	5.641E-02
	.68	1.89	.722	.042	4.211E-31	6.416E-02
	.71	1.94	.670	.051	2.973E-31	7.459E-02
	.73	2.00	.731	.062	1.472E-31	9.177E-02
	.76	2.06	.701	.073	1.132E-31	1.057E-01
	.78	2.13	.877	.094	4.417E-32	1.421E-01
	.81	2.24	.744	.123	2.919E-32	1.809E-01
	.83	2.25	.759	.156	1.823E-32	2.278E-01
	.86	2.23	.467	.212	3.180E-32	2.708E-01
10 MR						
	.18	.76	.862	.045	1.599E-28	7.569E-02
	.21	.85	.829	.027	1.254E-28	4.490E-02
	.23	.95	.796	.025	9.227E-29	4.268E-02
	.26	1.04	.769	.024	6.591E-29	4.095E-02
	.28	1.13	.743	.024	4.830E-29	4.006E-02
	.31	1.22	.727	.024	3.501E-29	4.026E-02
	.33	1.32	.720	.024	2.348E-29	4.048E-02
	.36	1.41	.717	.024	1.527E-29	4.096E-02
	.38	1.50	.724	.024	9.556E-30	4.122E-02
	.41	1.59	.722	.024	6.050E-30	4.104E-02
	.43	1.68	.724	.024	3.751E-30	4.094E-02
	.46	1.77	.728	.025	2.310E-30	4.150E-02
	.48	1.86	.736	.025	1.416E-30	4.216E-02
	.51	1.96	.759	.026	7.959E-31	4.296E-02
	.53	2.04	.749	.028	5.158E-31	4.453E-02
	.56	2.13	.743	.030	3.059E-31	4.670E-02
	.58	2.23	.777	.033	1.622E-31	5.002E-02
	.61	2.32	.717	.039	1.091E-31	5.644E-02
	.63	2.41	.769	.045	5.388E-32	6.500E-02
	.66	2.49	.768	.054	3.383E-32	7.594E-02
	.68	2.59	.769	.068	1.771E-32	9.447E-02
	.71	2.68	.837	.082	8.310E-33	1.156E-01
	.73	2.77	.898	.104	4.472E-33	1.495E-01
	.76	2.87	.835	.135	2.420E-33	2.131E-01
	.78	2.96	.874	.212	1.059E-33	2.893E-01
	.81	3.07	.630	.256	1.992E-33	3.192E-01

12MR

.18	.92	.837	.032	9.395E-29	5.469E-02
.21	1.03	826	.024	6.599E-29	3.983E-02
23	1.15	.806	.025	4.371E-29	4.125E-02
.26	1.26	.800	026	2.715E-29	4.176E-02
28	1.37	790	026	1.683E-29	4.157E-02
31	1.49	788	026	9.968E-30	4.215E-02
.33	1.60	787	027	5.731E-30	4.237E-02
.36	1.71	802	.027	3.166E-30	4.235E-02
.38	1.83	.816	027	1.772E-30	4.274E-02
41	1.94	819	.028	1.003E-30	4.341E-02
43	2.05	.818	.029	5.697E-31	4.383E-02
46	2.17	.825	.030	3.247E-31	4.535E-02
.48	2.28	.875	.031	1.581E-31	4.594E-02
.51	2.39	809	039	1.063E-31	5.182E-02
53	2.51	.899	.039	5.034E-32	5.321E-02
.56	2.62	864	.051	3.141E-32	6.336E-02
.58	2.73	.955	053	1.367E-32	6.726E-02
.61	2.84	.904	.074	7.987E-33	8.777E-02
.63	2.96	.813	.127	5.951E-33	1.356E-01
.66	3.07	933	.121	2.026E-33	1.419E-01
.68	3.18	.956	.232	7.193E-34	2.588E-01
.71	3.30	1.046	.227	4.467E-34	2.618E-01

20 MR

.18	1.54	.922	.073	9.760E-30	1.334E-01
.20	1.73	.916	.032	5.386E-30	5.773E-02
.23	1.93	.906	.027	2.795E-30	4.929E-02
.26	2.12	.902	.024	1.328E-30	4.311E-02
.28	2.32	.908	.023	6.073E-31	4.096E-02
.31	2.51	896	.023	2.827E-31	4.057E-02
.33	2.71	.920	.023	1.164E-31	4.079E-02
.36	2.90	941	.024	4.702E-32	4.112E-02
.38	3.10	.960	.025	1.932E-32	4.242E-02
.41	3.30	.994	.029	7.832E-33	4.524E-02
.43	3.50	1.005	.034	3.592E-33	5.036E-02
.46	3.69	1.033	.044	1.435E-33	6.049E-02
.48	3.89	1.143	.056	4.968E-34	7.607E-02

LAMBDA BAR

	X	PT	ALPHA	D ALPHA	NUCLEON CS	D LOGCS
7 MR						
	18	56	717	.036	5 280E-29	5. 945E-02
	.20	.63	.725	.029	3. 002E-29	4. 714E-02
	.23	.70	713	.031	1. 779E-29	4. 985E-02
	.26	78	.716	.034	9. 660E-30	5 276E-02
	.28	85	.692	.038	5 786E-30	5. 775E-02
	.30	92	815	044	1. 938E-30	6. 856E-02
	.33	99	795	.051	1. 298E-30	7 936E-02
	36	1 06	757	062	8 989E-31	9. 261E-02
	38	1 13	.661	.099	4 617E-31	1. 389E-01
	41	1. 20	831	106	1. 813E-31	1. 644E-01
	.44	1. 28	.563	.200	1. 524E-31	2. 678E-01
	.51	1. 46	1. 188	.418	8. 539E-34	7. 740E-01
10 MR						
	.18	.75	.753	035	3. 228E-29	5. 828E-02
	.20	.84	.751	.026	1. 705E-29	4. 219E-02
	.23	94	.764	027	8. 104E-30	4. 384E-02
	.25	1. 04	.748	.029	4. 163E-30	4. 566E-02
	.28	1. 13	.790	.031	1. 719E-30	4. 894E-02
	31	1. 21	810	.036	7. 960E-31	5. 517E-02
	.33	1. 32	.839	.045	3. 380E-31	6. 625E-02
	.36	1. 42	.820	.057	1. 907E-31	8. 194E-02
	.38	1. 50	.859	.073	8. 714E-32	1. 059E-01
	.41	1. 60	.941	.098	2. 954E-32	1. 432E-01
	43	1. 70	.976	.166	8. 055E-33	2. 437E-01
12 MR						
	.18	.90	.790	.036	1. 766E-29	5. 755E-02
	.20	1. 02	.812	028	8. 036E-30	4. 304E-02
	.23	1. 14	.824	.030	3. 488E-30	4. 537E-02
	.25	1 25	.797	034	1. 633E-30	4. 844E-02
	.28	1 37	.812	.039	6. 782E-31	5. 238E-02
	.31	1. 49	.831	.046	2. 905E-31	5. 892E-02
	.33	1. 61	.923	.054	1. 035E-31	6. 747E-02
	36	1. 72	.925	.068	4. 698E-32	8. 362E-02
	38	1. 84	.812	.124	2. 745E-32	1. 358E-01
	41	1. 95	972	110	9. 813E-33	1. 370E-01
	.43	2. 07	.582	.500	8. 385E-33	4 960E-01
20 MR						
	18	1 51	.928	.030	2. 674E-30	5. 420E-02
	20	1. 71	.952	.022	8. 612E-31	3 893E-02
	23	1. 91	960	.024	2. 634E-31	4 095E-02
	25	2. 11	1 005	.027	7. 959E-32	4 309E-02
	.28	2. 31	1. 037	032	2. 364E-32	4. 827E-02
	31	2. 51	1 009	046	8. 588E-33	6. 058E-02
	33	2. 71	1. 158	058	2. 131E-33	7. 713E-02
	36	2. 91	1. 338	080	4 938E-34	1 108E-01

K SHORT

	X	PT	ALPHA	D ALPHA	NUCLEON.CS	D LOGCS
7 MR						
	.18	.56	.708	.060	3.408E-28	1.015E-01
	.21	.63	.742	.032	2.067E-28	5.289E-02
	.23	.70	.717	.027	1.550E-28	4.465E-02
	.26	.77	.729	.026	9.961E-29	4.376E-02
	.28	.84	.712	.027	6.820E-29	4.421E-02
	.31	.92	.702	.028	4.588E-29	4.520E-02
	.33	.98	.753	.029	2.451E-29	4.687E-02
	.36	1.05	.719	.031	1.709E-29	4.908E-02
	.38	1.12	.724	.034	1.021E-29	5.371E-02
	.41	1.19	.753	.038	5.802E-30	5.946E-02
	.43	1.26	.738	.043	3.664E-30	6.679E-02
	.46	1.32	.758	.052	1.961E-30	7.912E-02
	.48	1.39	.810	.061	1.121E-30	9.464E-02
	.51	1.45	.702	.076	9.162E-31	1.110E-01
	.53	1.51	.805	.099	3.437E-31	1.496E-01
	.56	1.59	1.095	.127	9.987E-32	2.135E-01
10 MR						
	.18	.74	.736	.030	1.886E-28	5.072E-02
	.20	.84	.755	.026	1.154E-28	4.291E-02
	.23	.93	.763	.029	6.417E-29	4.182E-02
	.26	1.03	.768	.029	3.713E-29	4.177E-02
	.28	1.12	.774	.026	2.079E-29	4.244E-02
	.31	1.22	.792	.026	1.110E-29	4.309E-02
	.33	1.31	.800	.027	6.199E-30	4.438E-02
	.36	1.41	.832	.029	3.124E-30	4.687E-02
	.38	1.50	.838	.032	1.785E-30	5.004E-02
	.41	1.60	.864	.036	9.039E-31	5.541E-02
	.43	1.69	.864	.043	4.911E-31	6.477E-02
	.46	1.79	.880	.053	2.446E-31	7.777E-02
	.48	1.88	.828	.073	1.439E-31	1.013E-01
	.51	1.97	.858	.093	7.177E-32	1.290E-01
	.53	2.07	.902	.108	4.172E-32	1.527E-01
	.56	2.15	.972	.156	1.348E-32	2.292E-01
12 MR						
	.18	.90	.795	.031	9.440E-29	5.066E-02
	.20	1.02	.777	.027	5.891E-29	4.381E-02
	.23	1.14	.802	.027	2.847E-29	4.263E-02
	.26	1.25	.813	.027	1.501E-29	4.266E-02
	.28	1.37	.836	.027	7.520E-30	4.317E-02
	.31	1.49	.840	.029	3.896E-30	4.431E-02
	.33	1.60	.839	.031	1.871E-30	4.520E-02
	.36	1.73	.859	.034	8.795E-31	4.753E-02
	.38	1.84	.864	039	4.270E-31	5.153E-02
	.41	1.95	.869	.047	2.163E-31	5.961E-02
	.43	2.07	.842	.069	1.155E-31	7.952E-02
	.46	2.18	.954	.068	4.842E-32	8.261E-02
	.48	2.30	.990	.095	2.181E-32	1.131E-01
	.51	2.41	1.055	.105	1.110E-32	1.328E-01
	.53	2.52	.344	.462	2.680E-32	4.564E-01
20 MR						
	.18	1.52	.925	.028	1.525E-29	4.955E-02
	.20	1.72	.946	.023	5.214E-30	4.092E-02
	.23	1.91	.958	022	1.904E-30	3.966E-02
	.25	2.11	.995	.023	6.913E-31	4.015E-02
	.28	2.31	1.008	.024	2.656E-31	4.034E-02
	.31	2.51	1.043	.026	9.292E-32	4.159E-02
	.33	2.71	1.044	030	3.828E-32	4.493E-02
	.36	2.91	1.038	.038	1.391E-32	5.249E-02
	.38	3.11	1.104	.051	4.552E-33	6.662E-02
	.41	3.31	912	088	3.116E-33	1.012E-01
	.43	3.50	1.357	081	4.418E-34	1.137E-01

Appendix G

This appendix contains the polarization results for Λ's and $\bar{\Lambda}$'s arranged by the target material and incident proton angle. The columns are, respectively, the mean momentum, mean production angle, transverse momentum, Feynman x, the value of the polarization and its error, and the χ^2 per degree of freedom from Eqn. 5.17.

	MOM	ANGLE	PT	X	P	χ^2/DF
Be Λ	101.3	6.13	.621	.247	-.063±.004	55/39
	134.3	6.00	.806	.331	-.090±.004	
	163.5	5.84	.955	.405	-.124±.005	
	193.0	5.73	1.106	.479	-.179±.007	
	222.5	5.63	1.253	.553	-.222±.011	
	252.1	5.54	1.397	.628	-.250±.019	
	281.9	5.42	1.528	.702	-.248±.034	
	311.8	5.43	1.693	.777	-.326±.068	
	99.6	7.51	.748	.242	-.049±.006	40/29
	133.7	7.35	.983	.329	-.080±.007	
	162.9	7.15	1.165	.403	-.127±.009	
	192.5	7.05	1.357	.478	-.193±.014	
	221.8	6.98	1.548	.552	-.155±.024	
	251.4	6.92	1.740	.626	-.210±.049	
	72.9	10.12	.738	.173	-.033±.018	51/44
	91.0	9.99	.909	.220	-.062±.007	
	109.7	9.79	1.074	.268	-.072±.006	
	129.1	9.70	1.252	.318	-.091±.006	
	148.7	9.63	1.432	.367	-.113±.009	
	168.6	9.59	1.617	.418	-.159±.013	
	188.5	9.54	1.798	.468	-.146±.020	
	208.5	9.50	1.981	.518	-.131±.033	
	217.1	9.48	2.058	.540	-.166±.025	
	95.2	11.93	1.136	.231	-.071±.006	53/39
	109.5	11.87	1.300	.268	-.078±.004	
	128.7	11.77	1.515	.317	-.092±.005	
	148.4	11.72	1.739	.367	-.121±.007	
	168.3	11.65	1.961	.417	-.128±.017	
	188.2	11.60	2.183	.467	-.163±.020	
	208.1	11.58	2.410	.517	-.159±.034	
	94.9	20.30	1.926	.230	-.054±.006	52/44
	104.6	20.26	2.119	.255	-.057±.007	
	114.5	20.20	2.313	.280	-.063±.009	
	124.5	20.19	2.514	.306	-.092±.011	
	134.4	20.13	2.705	.331	-.111±.015	
	144.4	20.12	2.905	.356	-.090±.021	
	154.3	20.05	3.094	.381	-.129±.031	
	164.4	20.14	3.311	.407	-.158±.046	
	182.0	20.02	3.644	.451	-.273±.052	

	MOM	ANGLE	PT	X	P	χ^2/DF
Cu Λ	116.0	7.42	.861	.284	-.078±.022	7.7/9
	176.1	7.13	1.256	.437	-.090±.040	
	90.9	9.96	.905	.220	.021±.042	14/19
	109.5	9.76	1.069	.268	-.050±.029	
	128.7	9.67	1.245	.317	-.074±.031	
	148.8	9.60	1.428	.368	-.061±.040	
	90.8	11.92	1.082	.220	-.063±.022	31/24
	108.6	11.85	1.287	.265	-.037±.022	
	128.5	11.70	1.503	.316	-.096±.026	
	148.6	11.66	1.733	.367	-.172±.042	
	168.4	11.59	1.952	.417	-.089±.064	
	90.4	20.32	1.837	.219	-.039±.016	13/14
	108.3	20.25	2.193	.265	-.076±.013	
	128.2	20.18	2.587	.315	-.038±.022	
Pb Λ	115.8	7.44	.862	.284	-.052±.022	10/9
	176.0	7.16	1.260	.436	-.088±.088	
	90.7	9.97	.904	.219	-.040±.033	9.9/19
	109.3	9.75	1.066	.267	-.073±.029	
	128.5	9.65	1.240	.316	-.093±.033	
	148.8	9.59	1.427	.368	-.067±.040	
	90.7	11.91	1.080	.219	-.051±.022	16/24
	108.5	11.83	1.284	.265	-.054±.022	
	128.9	11.69	1.507	.317	-.059±.024	
	148.7	11.65	1.732	.367	-.061±.035	
	168.5	11.61	1.956	.417	-.125±.058	
	90.4	20.33	1.838	.219	-.043±.033	8.2/14
	108.6	20.23	2.197	.265	-.051±.041	
	128.3	20.20	2.592	.316	-.123±.059	

	MOM	ANGLE	PT	X	P	χ^2/DF
Be $\bar{\Lambda}$	65.0	10.11	.657	.152	.033±.016	9.8/15
	89.0	9.96	.886	.215	-.049±.032	
	108.0	9.93	1.072	.264	-.023±.018	
	65.0	12.11	.787	.152	.035±.023	20/30
	75.0	12.07	.905	.179	0.000±.019	
	85.0	12.04	1.023	.205	-.001±.021	
	95.0	12.02	1.142	.231	.003±.025	
	105.0	12.00	1.260	.256	.055±.030	
	115.0	11.97	1.377	.282	.019±.037	
	65.0	20.24	1.316	.152	.001±.009	21/30
	75.0	20.21	1.516	.179	-.005±.013	
	84.0	20.19	1.696	.202	.009±.016	
	94.0	20.17	1.896	.228	.035±.023	
	104.0	20.15	2.096	.254	.003±.029	
	114.0	20.15	2.297	.279	.015±.044	

REFERENCES

1 J. Lach, L. Pondrom, Annual Review of Nuclear and Particle Science 29, p203 (1979)

2 G. Bunce et. al., Phys. Rev. Lett. 36, 1113 (1976)

3 For a review of magnetic moment results see L. Pondrom, Proc. High Energy Spin Physics-1982, Ed. G. Bunce (1983) p. 45

4 R. Grobel, Ph.D. Thesis, University of Wisconsin (1980) (unpublished)

5 K. Heller, Proc. of 20th International Conference on High Energy Physics, Eds. L. Durand and L. Pondrom (1980) p. 61

6 P. Skubic et. al., Phys. Rev. D18, 3115 (1978)

7 L. Schachinger et. al., Phys. Rev. Lett. 41, 1348 (1978)

8 H. Hagerty et. al., Nucl. Instr. Meth. 115, 157 (1974)

9 L. Jones et. al., University of Michigan preprint UM-HE-79-01 (unpublished)

10 G. Bunce, Nucl. Instr. Meth. 172, 553 (1980)

12 R.P. Feynman, Phys. Rev. Lett. 23, 1415 (1969)

13 F. Taylor et. al., Phys. Rev. D14, 1217 (1976)

14 A. Beretvas, private communication

15 S. Berman, J.D. Bjorken, J. Kogut, Phys. Rev. D4, 3338 (1971)

17 R. Blankenbecler, S. Brodsky, J. Gunion, Phys. Rev. D12, 3469 (1975)

18 S. Brodsky, G. Farrar, Phys. Rev. Lett. 31, 1153 (1973)

19 D.S. Barton et. al., Phys. Rev. D27, 2580 (1983)

20 J. Cronin et. al., Phys. Rev. D11, 3105 (1975)

21 S. Denisov et. al., Nucl. Phys. B61, 62 (1973)

22 K. Heller et. al., Phys. Rev. D16, 2737 (1977)

23 S. Denisov et. al., op. cit.

24 A.N. Aleev et. al., Akademie der Wissenschaften DDR, preprint PHE 82-7

25 G.J. Bobbink et. al., Nucl. Phys. B166, 308 (1981)

26 B. Anderson et. al., Physics Reports 96C, 133 (1983)

27 Yu. Fisjak, E. Kistenev, Zeit. fur Phys. C10, 307 (1981)

28 K. Heller et. al., Phys. Rev. Lett. 51, 2025 (1983)

29 K. Heller et. al., Phys. Rev. Lett. 41, 607 (1978)

30 ibid.

31 C. Wilkinson et. al., Phys. Rev. Lett. 46, 803 (1981)

32 L. Deck et. al., Phys. Rev. D28, 1 (1983)

33 M. Corcoran et. al., Phys. Rev. D22, 2625 (1980)

34 T. De Grand, H. Miettenen, Phys. Rev. D24, 2419 (1981)

35 K. Heller, University of Michigan preprint UM-HE-77-38 (unpublished)

36 B. Andersson, G. Gustafson, G. Ingelman, Phys. Lett. 85B, 417 (1979)

37 J. Szwed, Phys. Lett. 105B, 403 (1981)

38 G. Preparata, Proc. of The 1980 Symposium on High Energy Physics with Polarized Beams and Targets, Eds. C. Joseph and C. Soffer, p. 121

39 F. Paige, D. Sidhu, Phys. Rev. D14, 2307 (1976)

40 K. Moriarty et. al., Lett. Nuovo Cimento 17, 366 (1976)

41 N.S. Craigie et. al., Physics Reports 99, 70 (1983)

42 G. Kane, J. Pumplin, W. Repko, Phys. Rev. Lett. 41, 1689 (1978)

43 N.S. Craigie et. al., op. cit.

44 S. Yokosawa et. al., Fermilab Proposal P-704